# Quantum Chemical Investigation of a Surface Science Model for the Inner Surfaces of Zeolites and Silicates

Dissertation

zur Erlangung des akademischen Grades

"doctor rerum naturalium"

(Dr. rer. nat.)

im Fach Chemie

eingereicht an der

Mathematisch-Naturwissenschaftlichen Fakultät

der Humboldt-Universität zu Berlin

von

**Dipl.-Chem. Frank Daniel Fischer**

Präsident der Humboldt-Universität zu Berlin:

Prof. Dr. Jan-Hendrik Olbertz

Dekan der Mathematisch-Naturwissenschaftlichen Fakultät:

Prof. Dr. Elmar Kulke

Gutachter: 1. Prof. Dr. Joachim Sauer

2. Prof. Dr. Hans-Joachim Freund

Tag der mündlichen Prüfung: 25. April 2016

# Quantum Chemical Investigation of a Surface Science Model for the Inner Surfaces of Zeolites and Silicates

**Frank Daniel Fischer**


## Abstract

We propose a surface science model system for the inner surfaces of both alumino- and other silicates. Such two-dimensional model systems offer three advantages. (1) They open up new avenues to study complex materials under very well-defined conditions. (2) Properties that could previously not be accessed directly in an experimental setup can now be measured using the tools of surface science. Thus, experimental reference numbers can be found and compared directly to computational results. (3) For zeolites, the two-dimensional aluminosilicate films present the limiting case of a zeolite with infinite pore size and are a established as valuable model in investigating the structure-reactivity relationships. Density functional theory (DFT) calculations are used to propose structural models for novel ultra-thin silica films. The periodic DFT calculations give insight into the relative stability of different substitution patterns, the solid acidity or possible reactivity and the vibrational properties. Generally, the DFT results agree very well with the experimental observations. The structure of a Ti-silicate film is found to be similar to known phyllosilicates, while interestingly and maybe counter-intuitively, it has no uniform distribution of Ti. For Al-silicate films, the assumption of homogeneous distribution of Al is substantiated even though the computational results are not conclusive. These films exhibit bridging hydroxyl groups that are highly acidic compared to known zeolites, relating to possible high reactivity. In concert with the experimental results, the Al-silicate films are established as two-dimensional model systems for the otherwise complex, three-dimensional frameworks of zeolites and substituted silicates.

# Quantenchemische Untersuchung eines oberflächenphysikalischen Modellsystems für die inneren Oberflächen von Zeolithen und Silikaten

**Frank Daniel Fischer**


## Kurzzusammenfassung

Wir stellen ein oberflächenphysikalisches Modellsystem für die inneren Oberflächen von Alumino- und sonstigen Silikaten vor. Derartige zweidimensionale Modellsysteme bieten drei Vorteile. (1) Sie eröffnen neue Ansätze zur Untersuchung komplexer Materialien unter sehr wohldefinierten Bedingungen. (2) Eigenschaften, die sonst nicht direkt experimentell zugänglich waren können nun mit den Instrumenten der Oberflächenphysik gemessen werden. So können experimentelle Referenzwerte gefunden und direkt mit quantenchemischen Resultaten verglichen werden. (3) In Bezug auf Zeolithe stellen die zweidimensionalen Aluminosilikatfilme den Grenzfall eines Zeoliths mit unendlichem Porenvolumen dar und sind als wertvolles Modell zur Untersuchung von Struktur-Reaktivitätsbeziehungen etabliert. Die Berechnungen mit periodischer DFT ermöglichen Einsichten in die relativen Stabilitäten unterschiedlicher Substitutionsmuster, die feste Säurestärke oder mögliche Reaktivität, sowie die Schwingungseigenschaften. Insgesamt stimmen die DFT-Ergebnisse sehr gut mit den experimentellen Beobachtungen überein. Die Struktur eines Ti-Silikatfilms wurde bestimmt. Sie ist ähnlich der von bekannten Phyllosilikaten, während sie interessanterweise und vielleicht entgegen der Intuition keine gleichmäßige Verteilung von Ti aufweist. Im Falle der Al-Silikatfilme wird die Annahme einer homogenen Al-Verteilung bekräftigt, obwohl die quantenchemischen Ergebnisse nicht endgültig sind. Diese Filme weisen verbrückende Hydroxylgruppen mit, im Vergleich zu bekannten Zeolithen, hoher Azidität auf, was auf eine mögliche hohe Reaktivität hinweist. Gemeinsam mit den experimentellen Resultaten werden die

Al-Silikatfilme als zweidimensionale Modellsysteme für die sonst komplexen, dreidimensionalen Netzwerke von Zeolithen und substituierten Silikaten etabliert.

# Contents

# 1 Publications

Most of the research presented in this thesis has been published in scientific journals. The following list identifies the contributions of the author of this thesis (F.D.F.) to the publications.

**FDF1** J. A. Boscoboinik, X. Yu, B. Yang, **F. D. Fischer**, R. Włodarczyk, M. Sierka, S. Shaikhutdinov, J. Sauer, H.-J. Freund, "Modeling Zeolites via Metal Supported, Two-Dimensional Aluminosilicate films," *Angew. Chem. Int. Ed.*, vol. 51, no. 24, pp. 6005-6008, 2012.

F.D.F. contributed the quantum chemical calculations for Chabazite and also performed calculations for unsupported Aluminosilicate films which, though not published directly in this paper, were used internally.

**FDF2** J. A. Boscoboinik, X. Yu, E. Emmez, B. Yang, S. Shaikhutdinov, **F. D. Fischer**, J. Sauer, H.-J. Freund, "The interaction of probe molecules with bridging hydroxyls of two-dimensional zeolites: a surface science approach," *J. Phys. Chem. C*, vol. 117, no. 26, pp. 13547-13556, 2013.

F.D.F. contributed all quantum chemical calculations. He wrote the section on computational methods and the first drafts of the computational results and their discussion.

**FDF3** **F. D. Fischer**, J. Sauer, X. Yu, J. A. Boscoboinik, S. Shaikhutdinov, H.-J. Freund, "Ultrathin Ti-Silicate Film on a Ru(0001) surface," *J. Phys. Chem. C*, vol. 119, no. 27, pp. 15433-15448, 2015.

F.D.F. contributed all quantum chemical calculations and prepared the first draft of the publication, except for the section on experimental details.

# 2 Introduction

## Zeolites as Porous Materials: Industrial Applications and Framework Structure

Catalysis in general, and particularly acid-base catalysis, is one of the fundamental principles of chemical reactivity. It is observed in many varieties, in enzymatic, homogeneous and heterogeneous catalysis. For industrial processes, zeolites are the most important class of solid acids [1]. The modular combination of the microporous framework structure on the one hand, i.e. the molecular sieving property, with on the other hand the tailoring of acid functionality of zeolites is a particularly powerful concept and appears as so-called "shape-selectivity". One of the well-known applications for acidic zeolite catalysts is the "cracking" in crude oil refining. Similarly, many other chemical products – from polymers to fine chemicals – "see" a zeolite catalyst sometime during the course of their manufacturing. Heteroatom-substituted zeolites can be designed for their reactive properties and specific applications [2, 3]. Recent international conferences on zeolites and related functional materials organized by the International Zeolite Association (for example) cover applications from oil refinery and petrochemistry, to environmental catalysis and biomass conversion, from adsorption and separation processes to novel applications in the field of health, electronics and sensors [4]. While this thesis is concerned with silicates and zeolites, also other materials like silico-alumino-phosphates (SAPOs) [5] or especially nowadays, an increasing variety in metal-organic frameworks (MOFs) are at the cutting edge of research [6, 7]. Similar to zeolites, their potential is in the combination of local (tailored) reactivity with a highly porous framework structure that allows a large

variety of complex three-dimensional arrangements together with designing the internal surface structure and chemistry and the so-called coordination space.

Zeolites are three-dimensional crystalline frameworks of corner-sharing $SiO_4$ and $AlO_4^-$ tetrahedra. The conformational flexibility of the Si-O-Si and Si-O-Al structural elements (bond angles) allows a huge variety of different topologies of the frameworks. This enables (typically) interconnected channels and cavities, which can be accessed from outside via diffusion by small molecules. The negative charge (one per $[AlO_4]$ tetrahedron) is compensated by cations like $Na^+$ or $NH_4^+$ . When this cation is a proton, the zeolite becomes a solid acid. The proton is connected to one of the four oxygen atoms of the $[AlO_4]$ tetrahedra, so that a bridging hydroxyl group Si-O(H)-Al is formed. These "bridging hydroxyls" exhibit high Brønsted acidity.

One of the ways to characterize these bridging hydroxyls is by adsorption of probe molecules. The O-H vibration is affected upon adsorption of weak bases such as carbon monoxide or ethene. The red-shift of the IR adsorption band is used as a measure for the solid acidity [8, 9]. Nicholas and Haw found experimentally that the proton transfer to form a carbenium ion depends on the proton affinity of the parent hydrocarbon [10]. A generalization of this was found by theoretical methods. Any molecule with a proton affinity close to that of ammonia (854 kJ/mol) or larger gets protonated upon interaction with the bridging hydroxyl, while molecules with lower proton affinity (weaker bases) form a H-bonded complex [11, 12].

In addition to the framework structure, cavity dimensions, pore sizes and other framework properties, concentration and distribution of the aluminum ions are parameters that characterize acid zeolites. These parameters are governed by certain boundaries. According to Löwenstein's rule, which states that Al-O-Al connections between $[AlO_4]$ tetrahedra are unlikely, the lowest possible Si:Al ratio is exactly one [13].

## Theoretical Modeling

Computational chemistry can and has contributed to the field of zeolite science over many years. The fundamental understanding of zeolite-synthesis, for example nucleation, solvent and template effects, crystal growth [14, 15], up to post-synthetic modifications like de/re-alumination [16] or dissolution, from catalytic activity [12, 17] to diffusion properties [18], requires sophisticated theoretical analysis combined with high quality experiments. Characteristic for the computational chemist's approach are the limitations of the models that are used. If a high degree of accuracy is the goal, the zeolite framework has to be approximated using cluster models. For this purpose, clusters represent a defined cut out of the framework structure and the dangling bonds are terminated with hydrogen atoms [19, 20]. While this approach allows highly accurate calculations (for benchmark data, see for example ref. [21]), it cannot adequately describe reality, since it neglects long-range contributions. In addition, more macroscopic properties, such as diffusion, framework flexibility or the effect of bulk defects, cannot adequately be treated this way. On the other end of the spectrum, molecular mechanics methods can treat huge numbers of atoms at once – at the cost of accuracy and flexibility. Hybrid methods like QM/MM try to combine the advantages of both approaches by approximating the long-range contributions to the total energy using a lower level of theory. The lower level of theory can be a molecular mechanics method [22], but can also be a lower level of ab initio theory [23–26]. Using modern computer power, density functional theory with periodic boundary conditions (PBC-DFT) can bridge the gap. Especially combined with dispersion correction (DFT+D), it offers reasonable accuracy [27, 28] and can be used to model chemical reactions (as opposed to most force fields) but can still be applied to systems of many atoms (up to hundreds, as opposed to high level wave-function based ab initio methods). Using periodic boundary conditions, the long-range contributions in the crystal can be modeled in a way that is satisfactory for many applications. Nevertheless, it has to be mentioned that this approach also has its limitations; inhomogeneous distributions of certain atoms or defect sites in the crystals cannot be treated in a way that is satisfying in all cases, since

the periodic boundary conditions mean that the defect is copied in each periodic image. One particularly dramatic example is the inability of PBC-DFT to calculate deprotonation energies of zeolites. In periodic boundaries, the negative charge appears in each periodic image, which leads to a diverging energy. This problem can be eliminated by adding a background charge. But then there is the remaining problem of the interaction of the charged defects. To deal with this problem by applying a supercell approach can be very computationally demanding [29]. Alternatively, an approximate scheme can be used for the aperiodic correction [30]. As it is, computational chemists have to keep in mind two kinds of approximations when comparing their results to experimental observations; on the one hand, there is the limited accuracy of the methods that are used. For high-level ab initio methods, this limit can approach chemical accuracy, which means deviations of less than 1 kcal/mol from accurate experimental reference values (which certainly are not always available!) [31, 32]. On the other hand, one has to keep in mind the approximations that were done to the chemical model: the simplification of the true, complex, three-dimensional system to a cluster model or to an array of periodic images.

## Surface Science Models for Zeolites

Recent developments in the fabrication of very well-defined, substrate-supported, two-dimensional silicate model systems allow for the use of novel approaches in silicate and zeolite research [33, 34]. The synthesis paradigm in surface science is completely different to the usual, wet-chemical approach for obtaining micro- or macro-crystalline powder (bulk) materials. Here, nano-scale ultrathin silicate films consisting of only a few atomic layers are prepared using ultra-high vacuum (UHV) methods, by depositing atoms from the gas phase on an extremely clean single-crystal metal surface. A unique tool box of characterization techniques that cannot be applied in the same way on the bulk materials can now be employed to investigate these thin film materials. For example, scanning tunneling microscopy (STM) allows for very high-resolution imaging of these surfaces that, with respect to the original bulk materials, correspond to the inner surfaces of the zeolite

and therefore would normally be inaccessible for direct microscopic imaging techniques (see Figure 2.1). The same is true to some extent for other powerful techniques such as low energy electron diffraction (LEED), x-ray photoelectron spectroscopy (XPS), temperature programmed desorption (TPD) experiments, and especially, infrared reflection-absorption spectroscopy (IRAS). They can be applied on exposed surfaces, bringing zeolite and silicate research into the field of surface science. Since the UHV-prepared films are extremely well-defined, experiments on these surfaces allow the rigorous probing of atomistic properties which are relevant for a fundamental understanding of zeolites.

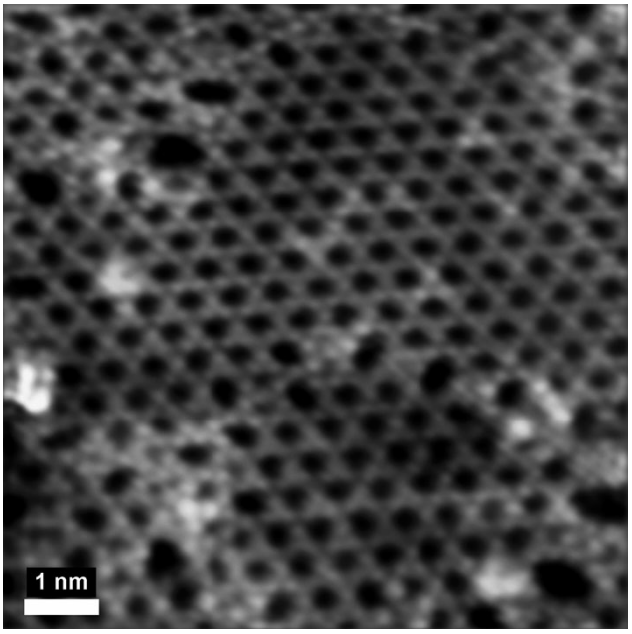


***Figure 2.1:*** *STM image of a $Al_{0.36}Si_{0.64}O_2$ film on a Ru(0001) surface. The ordered regions show a honeycomb-like structure. [The figure is taken from the first publication on this system [FDF1].]*

A main advantage of the thin films lies in the reduction in complexity, which is important for both theoretical and experimental investigations. The virtually defect-free films can be studied by employing the tools of surface science while the two-dimensional films are also structurally more simple and therefore much easier to model computationally compared to their three-dimensional analogues. Ideally, such films allow for a direct comparison of calculations with experiments, since some sources of errors (approximations when using cluster models, defect sites, diffusion properties, etc.) can be excluded. For zeolites, a two-dimensional aluminosilicate film is of special interest for understanding internal zeolite surfaces. It can be regarded as representing the case of a zeolite with

infinite pore size, which provides a very valuable reference point when trying to unravel the structure-reactivity relationships in zeolites. In conclusion, such kinds of novel thin film model systems for zeolites offer vast possibilities and new avenues for theory and experiment to work in concert towards a better understanding of zeolites and related materials on a fundamental, atomistic level.

## The Scope of this Thesis

This thesis is a product of work done in the group of Prof. J. Sauer at the Humboldt-Universität, in collaboration with the group of Prof. H.-J. Freund at the Fritz-Haber Institut (both in Berlin), following up on a history of colloborative research between the two groups that also takes place within the framework of the cluster of excellence UniCat [35] and within the new colloborative research center (CRC) 1109 [36].

The experimental partners at the Fritz-Haber Institut developed novel, ultra-thin silicate films prepared on metal single-crystal support in UHV that have to be characterized. A combined approach of experimental techniques and theoretical calculations has proven to be successful to unravel the structures of such systems [37]. Calculations using DFT with periodic boundary conditions have made it possible to precisely identify the structure of the ultra-thin silicate mono- and bilayer film structures, which previously had not been known in atomic detail [38].

For this thesis, calculations have been performed on two new thin film systems, namely Ti- and Al-substituted silica bilayers on Ru(0001) support. The task was to identify possible structures and to verify the structural prediction by a comparison of calculated and observed spectroscopic (IRAS) properties. In addition to the identification of the structures, first steps are done to investigate the properties of the novel systems. Doing so allowed for the aluminosilicate film to be established as a new zeolite model system [39] of especially high interest, for which it has already been mentioned in a recent review of the field [40].

The following paragraphs provide an overview by introducing the chemical systems

that were studied in the scope of this thesis.

**Ultrathin Ti-Silicate Film on a Ru(0001) Surface.** (Section 4.1)

Well-defined ultrathin silicate [34, 38, 39] and aluminosilicate [41, 42] films prepared on metal single-crystal support are of interest because they are suited to model (experimentally and computationally) otherwise three-dimensional, complex materials such as zeolites.[1] Corner-sharing [$SiO_4$] tetrahedra are the building blocks of these films. By now, it is well known how under different experimental conditions, either mono- or bilayers are formed [37]. Similar to the preparation of the Al-containing films, other metal cations can be incorporated into the films, as was most recently reported for the case of a Fe-containing silicate film [43].

In this thesis, heteroelement exchanged Ti-silicate films (Ti/Si substitution) that were prepared following this same approach [41] are investigated. Titanium silicates or Ti-containing zeolites often find applications as catalysts. For example, titanium silicate-1 (TS-1, first synthesized in 1983), is a structural analogue to the zeolite ZSM-5, where Ti is substituted for Al to a certain extent. It enabled new approaches for selective oxidation reactions. Previous work on zeolite-like Ti-containing silicate films by Goodman and coworkers employed a Mo(112) surface as substrate. The identification of the structure was based on a wrong structural model of the monolayer silica film that has since been replaced by the mono- and bilayer models of these films [38] that form the starting point of this work.

The following tasks are addressed:

- What kind of stable Ti-silicate, Ru(0001) supported thin film structures can be found in the calculations for varying Ti contents, based on the known structure of the pristine silica bilayer film?
- What are the relative energies, which structures are predicted to be most stable?
- Can a structural model be proposed that explains the experimental observations?

[1] This text is an only slightly changed excerpt from the paper published on the topic [FDF3].

In particular, do the calculated vibrational frequencies agree with the experimental IRAS results for varying Ti-contents?

The results are presented in detail in section 4.1.

### Ultrathin Al-Silicate Film on a Ru(0001) Surface (Sections 4.2 and 4.3)

The preparation of well-defined aluminosilicate thin films was first reported using a Mo(112) substrate [44].[1] It was shown that this film consists of a single layer network of corner-sharing [$SiO_4$] tetrahedra and [$AlO_3$] units, and the film is strongly bound to the Mo(112) surface by Si-O-Mo linkages (see Figure 2.2a). Certainly, for those monolayer films the metal support has to be explicitly included in the proper description of the system. Furthermore, this film lacks the negative framework charge present in zeolites, which is responsible for the presence of acidic OH groups. The preparation of aluminosilicate films that a) are constituted of tetrahedral [$SiO_4$] and [$AlO_4$] building blocks, b) are weakly bound to the underlying metal support and c) expose highly acidic OH species, provides more adequate model systems. Our results open up an avenue for experimental and theoretical modeling of zeolite surfaces that is aimed at a fundamental understanding of structure–reactivity relationships in those materials.

The following tasks are addressed:

- Derive the possible structures for the Al-silicate films containing varying amounts of Al. The starting point for the structural explorations was the well-known structure of the pristine silicate bilayer film. It was assumed that the overall charge of the film is zero.

- What are the relative energies, which structures are most stable?

- Can a structural model be proposed that explains the experimental observations? In particular, do the calculated vibrational frequencies agree with the experimental IRAS results?

[1] This text is based on an only slightly changed excerpt from the publication [FDF1].

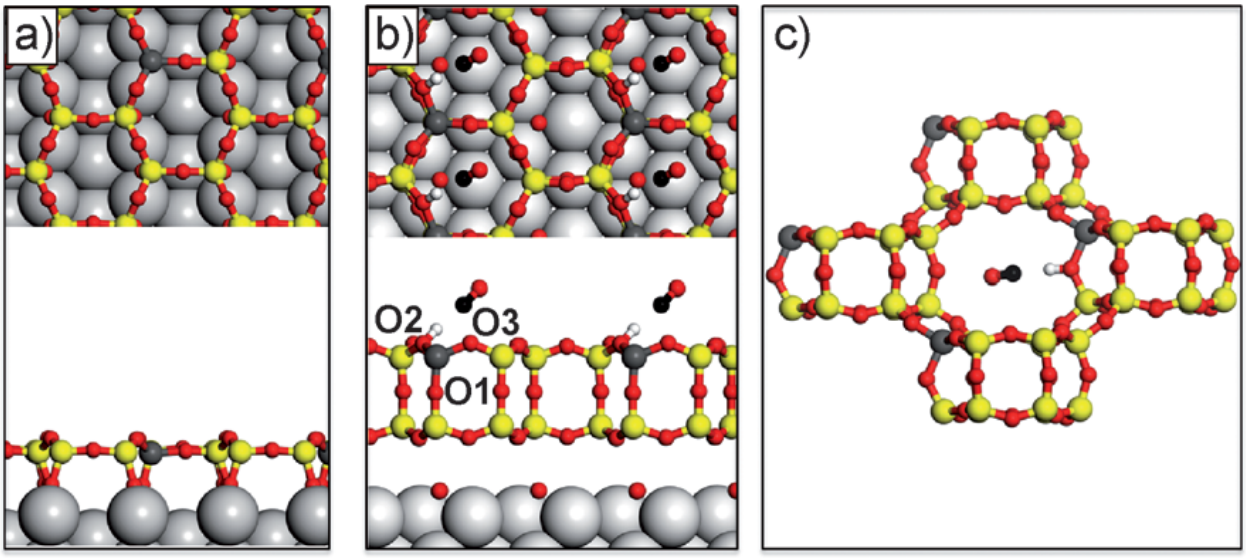


***Figure 2.2:*** *Structural models of a) an $AlSi_7O_{19}$ film on Mo(112); b) a $HAlSi_7O_{16}$ film on $O(2 \times 1)Ru(0001)$; and c) chabasite (H-CHA) with the proton on O1. Top and cross views are shown in (a) and (b), adsorbed CO are shown in (b) and (c). One of the surface O atoms on Ru(0001) underneath the film is not seen in the top view. Si yellow, O red, Al dark gray, C black, H white. The figure is taken from [FDF1].*

The scope of this project is largely identical to investigation of the Ti-silicate films. However, the results (section 4.2) made it necessary to add further tasks. Of particularly high interest are the properties of the bridging hydroxyls in zeolites. It had to be investigated, whether the experimentally prepared films exhibit any such groups. The following tasks are addressed:

- Can the experimental film be understood as a zeolite model system? For this to be true, there have to be bridging hydroxyl groups. In the experiment, they are identified using IRAS in combination with isotope exchange experiments. Do the properties (in particular, the acid strength) of the bridging hydroxyls in our computationally predicted structures match with the experimentally observed properties?

- What simplifications can be done to the computational model to reduce the cost and complexity, while still adequately representing the properties of the films, especially concerning the acidic sites?

- In investigating such models of reduced complexity, we can try to answer questions on the role of the metal support and the aluminum content. Can we understand

their influence on the acidity?

The results are presented in sections 4.2 and 4.3.

**Adsorption of Probe Molecules on Zeolites and a Two-Dimensional Zeolite Model System** (Section 4.4)

Al-silica bilayers on Ru(0001) support are genuine models of the internal surface of zeolites representing infinitely large pores.[1] This opens new possibilities for studying phenomena that depend on pore size such as surface curvature effects on adsorption energy [45]. The Al-silica bilayers do not have dangling bonds saturated by surface hydroxyls as external surfaces of zeolites or mesoporous materials have [8, 9]. The presence of bridging hydroxyls in these films, which are named H(D)-2dH in its protonated or deuterated forms (for 2-dimensional Hexagonal), was demonstrated by adsorption of carbon monoxide as a probe molecule [FDF1]. It forms an adduct with the proton and induces a red shift of the O-H stretching vibration, with the magnitude of the shift being proportional to the acidity [8, 9]. The results were found to be comparable to zeolite H-CHA, which is also composed of hexagonal prisms but in a three-dimensional arrangement. Other probes are also used for zeolites to determine the presence of acidic sites within the pores of the framework [8].

This thesis, in addition to CO, reports infrared spectra of this film after reaction with probe molecules $C_2H_4$, $NH_3$, and pyridine (Py). Similar to CO, ethene is a weak base. It has been shown that the shifts induced by CO and ethene are directly proportional to each other for OH groups in different materials [46]. More importantly, ethene, the simplest olefin, is the reactant in the ethene oligomerization reaction which is also catalyzed by bridging hydroxyls. The use of this probe molecule provides information about the precursor state for this reaction [47]. Until now, much of the details about the adsorption geometry of such probe molecules (and reactants) came from theoretical models based on educated assumptions [48]. By using a well-defined model system and the analytical tools of surface science [41, 49], experimental data can provide a more detailed understanding

[1] This text is an only slightly changed excerpt from the paper [FDF2].

of the interaction of different molecules with the active sites on zeolites and allows the validation of the use of this model system for mechanistic studies.

For this thesis the following tasks are addressed:

- Identify the adsorption structures of CO, $C_2H_4$, $NH_3$ and pyridine ($NC_5H_5$) on the two-dimensional zeolite model system H-2dH.
- What are the adsorption energies and the shifts in the vibrational frequencies?
- To give meaning to the calculated values, it is best to look at relative trends. So also calculate the adsorption structures for the molecules adsorbed on acidic chabazite H-CHA.
- Do the computationally derived properties agree with what is observed experimentally using IRAS?
- How can H-2dH be characterized in relation to known zeolites regarding its acidity and thus, its possible catalytic activity?

The results are presented in detail in section 4.4.

# 3 Methods

## 3.1 Density Functional Theory (DFT)

Modern theoretical chemistry offers a large variety of methods that can be used to model chemical systems.[1] Theoretical approaches that are ideally based only on physical concepts and universal constants are called *ab initio* methods. Compared to empirical methods which offer very efficient, cheap (fast) calculations by using a large number of preset parameters, *ab initio* methods have the advantage of generality, the ability to treat many chemically different systems. The starting point for *ab initio* methods (also for semi-empirical methods) is the time-independent Schrödinger equation

$$H\Psi = E\Psi. \tag{3.1}$$

The central quantity for such methods is therefore the wavefunction $\Psi$. In itself, such a wavefunction is no intuitive object for a chemist. Even when applying the Born-Oppenheimer approximation (treating the nuclei classically), it depends on the spin and spatial coordinates of all $N$ electrons. Hartree-Fock theory introduces an approximation for $\Psi$, express-

[1] This chapter summarizes concepts that can be found in many quantum chemistry textbooks. In particular, the books by C. J. Cramer [50] and by W. Koch and M. C. Holthausen [51] were useful.

ing it as a Slater determinant

$$\Psi(\mathbf{x}_1, \mathbf{x}_2, \ldots, \mathbf{x}_N) = \frac{1}{\sqrt{N!}} \begin{vmatrix} \chi_1(\mathbf{x}_1) & \chi_2(\mathbf{x}_1) & \ldots & \chi_N(\mathbf{x}_1) \\ \chi_1(\mathbf{x}_2) & \chi_2(\mathbf{x}_2) & \ldots & \chi_N(\mathbf{x}_2) \\ \vdots & \vdots & \ddots & \vdots \\ \chi_1(\mathbf{x}_N) & \chi_2(\mathbf{x}_N) & \ldots & \chi_N(\mathbf{x}_N) \end{vmatrix}. \tag{3.2}$$

Expressing the wave function as a determinant of one-electron spin orbitals $\chi_i$ allows for some more clarity as each electron is somewhat independent, interacting only with the static electric field created by all other electrons. While it is helpful for the chemist to be able to think of separated electrons in their orbitals, this approximation limits the accuracy of Hartree-Fock theory. The error compared to the correct solution of the Schrödinger equation is called *electron correlation energy*. Within the world of wave-function based methods, this problem is approached by going beyond the approximation of treating the wave function as a single determinant of one-electron functions. One possibility is the construction of the wave function as a linear combination of determinants

$$\Psi = c_1\Psi_1 + c_2\Psi_2 + \ldots, \tag{3.3}$$

ultimately leading to *(full) configuration interaction* (FCI), making the exact solution of the Schrödinger equation possible. Unfortunately, FCI calculations can be carried out only for very small molecules due to the extreme computational costs. Other wavefunction-based methods that treat electron correlation more approximately are very costly. Available methods are, for example, *multiconfiguration self-consistent field theory* (MCSCF), *complete active space self-consistent field theory* (CASSCF) or *coupled cluster theory*. *Møller-Plesset perturbation theory* can comfortably be applied on even medium-sized clusters but is still problematic for extended, periodic systems.

A theorem by P. Hohenberg and W. Kohn states that the ground-state electron density $\rho(\mathbf{r})$ uniquely determines the Hamilton operator $H$ and hence is sufficient to calculate all ground state properties, for instance the total energy of a system. $\rho$ is a much simpler

quantity than $\Psi$, being a function of only three variables $(r_x, r_y, r_z)$, independent of the size of the system. While the first Hohenberg-Kohn theorem sets the foundation for density functional theory, proving its existence, the question remains how to obtain $\rho$. The second Hohenberg-Kohn theorem shows, that just as $\Psi$ in molecular orbital theory, the electron density obeys a variational principle, so the ground state energy can be written as

$$E_0 = \min_{\rho \to N} \left( E[\rho(\mathbf{r})] \right). \tag{3.4}$$

Thus, a density that provides a lower energy $E[\rho(\mathbf{r})]$ is closer to the correct one. Theoretically, this means that a computational routine should modify candidate densities as long as it is possible to obtain lower energies (up to a pre-defined convergence limit), to find the correct ground-state energy. While the density can theoretically be mapped onto the Hamiltonian and the wave function, the functional $E[\rho(\mathbf{r})]$ is not known.

Since, in practice, approximate functionals are used, the variational principle only shows how to get the correct density from this functional. The calculated energy may then be even lower than the exact energy.

The functional can be separated into several components

$$E[\rho(\mathbf{r})] = T[\rho(\mathbf{r})] + V_{\mathrm{ne}}[\rho(\mathbf{r})] + V_{\mathrm{ee}}[\rho(\mathbf{r})], \tag{3.5}$$

namely the kinetic energy of the electrons, the nucleus-electron interaction and the electron-electron interaction. The attraction of electrons to the nuclei can be calculated using the Coulomp potential

$$V_{\mathrm{ne}}[\rho(\mathbf{r})] = \sum_{k}^{\text{nuclei}} \int \frac{Z_k}{|\mathbf{r} - \mathbf{r}_k|} \rho(\mathbf{r}) \mathrm{d}\mathbf{r}. \tag{3.6}$$

The classical electron-electron interaction energy $V_{\mathrm{ee}}[\rho(\mathbf{r})]$ is

$$V_{\mathrm{ee}}[\rho(\mathbf{r})] = \frac{1}{2} \iint \frac{\rho(\mathbf{r}_1)\rho(\mathbf{r}_2)}{|\mathbf{r}_1 - \mathbf{r}_2|} \mathrm{d}\mathbf{r}_1 \mathrm{d}\mathbf{r}_2. \tag{3.7}$$

Attempts to calculate the kinetic energy $T[\rho(\mathbf{r})]$ by using the model of a homogeneous

electron gas lead to acceptable results for metals but this approach is not applicable for molecules. The basic, orbital-free form of density functional theory (DFT) has the hypothetical advantage of depending on only the three spatial coordinates. It is unfortunately not usable for quantum chemical purposes since there is no intuitive way to calculate the missing quantities (kinetic energy and non-classical electron-electron interactions) directly from the electron density. In 1965, W. Kohn and L. J. Sham suggested a solution for parts of this problem. Instead of trying to calculate the whole exact kinetic energy, they found a way approximate it by reintroducing a reference system of non-interacting electrons as a Slater determinant of orbitals $\chi_i$. The result is known as Kohn-Sham (KS)-DFT. The missing contributions to $E[\rho(\mathbf{r})]$, the correction to the kinetic energy related to the approximation of considering non-interacting electrons in $T_{\text{ni}}$ and all non-classical corrections to the electron-electron repulsion energy $V_{\text{ee}}$, are collected and expressed as $E_{\text{XC}}[\rho(\mathbf{r})]$. The exchange-correlation functional $E_{\text{XC}}$ is not known. Approximations to it, using a variety of approaches, give birth to the many different DFT functionals that are known today. Kohn-Sham orbitals are defined as a non-interacting reference system which corresponds to the same electron density as the real system. The kinetic energy for this system can be calculated as

$$T_{\text{ni}} = \sum_{i}^{N} \langle \chi_i | -\frac{1}{2}\nabla^2 | \chi_i \rangle \,. \tag{3.8}$$

The Hamiltonian for the non-interacting reference system has to include an effective potential $V_{\text{n.i.}}$

$$H_{\text{n.i.}} = -\frac{1}{2}\sum_{i}^{N}\nabla_i^2 + \sum_{i}^{N} V_{\text{n.i.}}(\mathbf{r}_i), \tag{3.9}$$

that must be chosen in such a way that the density of the reference system $\rho_{\text{n.i.}}$ is equal to the density of the real, interacting density $\rho_0$

$$\rho_{\text{n.i.}}(\mathbf{r}) = \sum_{i}^{N} \langle \chi_i | \chi_i \rangle \,. \tag{3.10}$$

The Kohn-Sham orbitals are determined analogously to the methodology of the Hartree-

Fock approach, using

$$h_i^{\mathrm{KS}}\chi_i = \epsilon_i\chi_i, \tag{3.11}$$

where the one-electron Kohn-Sham (KS) operator is defined as

$$h_i^{\mathrm{KS}} = -\frac{1}{2}\nabla_i^2 + V_{\mathrm{n.i.}}(\mathbf{r}). \tag{3.12}$$

It can be shown that $V_{\mathrm{n.i.}}(\mathbf{r})$ can be formulated as

$$V_{\mathrm{n.i.}}(\mathbf{r}) = \int \frac{\rho(\mathbf{r}')}{|\mathbf{r}_i - \mathbf{r}'|}\mathrm{d}\mathbf{r}' - \sum_k^{\text{nuclei}} \frac{Z_k}{|\mathbf{r}_i - \mathbf{r}_k|} + V_{\mathrm{XC}}(\mathbf{r}), \tag{3.13}$$

where $V_{\mathrm{XC}}(\mathbf{r})$ is still unknown so it needs to be approximated. Formally, it is defined as a functional derivative of $E_{\mathrm{XC}}$ with respect to $\rho$:

$$V_{\mathrm{XC}} = \frac{\delta E_{\mathrm{XC}}}{\delta\rho}. \tag{3.14}$$

$V_{\mathrm{XC}}$ has to be a (one-electron) operator for which the expectation value of the Slater determinant of the KS orbitals is $E_{\mathrm{XC}}$. Since $V_{\mathrm{n.i.}}$ in equation 3.13 itself depends in the Coulomb term on the density, the KS one-electron equations 3.11 have to be solved iteratively, just like what is known from the Hartree-Fock Self-Consistent-Field (SCF) method.

## 3.2 DFT with Periodic Boundary Conditions

**Periodic Boundary Conditions** From an atomistic point of view, crystals are large, nearly infinite systems. Typically, it is useful to describe them using the concept of a *unit cell (u.c.)* as the fundamental building block. The crystal consists of an infinite number of unit cells. For computational purposes, the crystal is constructed as a unit cell and its copies or *images* that are created by translations of the original u.c. along the crystal lattice vectors. The application of periodic boundary conditions (pbc) means, that if an object passes through one side of the u.c., it re-appears at the opposite side.

**Plane Wave Expansion** The Kohn-Sham orbitals $\chi_j$ are expressed in terms of basis functions $\Phi_i$:[1]

$$\chi_j = \sum_{i=1}^{N} c_{ij}\Phi_i, \tag{3.15}$$

where $N$ is the number of basis functions. During the computational procedure to determine the Kohn-Sham orbitals (see eq. 3.11), the various coefficients $c_{ij}$ have to be found. Atom-centered Gaussian-type orbitals are typically used for $\Phi_i$ when treating finite systems like molecules or clusters. When periodic boundary conditions are applied, it can be useful to use periodic basis functions

$$\Phi_{\mathbf{k}} = \exp(\mathrm{i}\mathbf{k}\mathbf{r}). \tag{3.16}$$

Crystal orbitals can then be expressed as Bloch functions:

$$\chi_{i,\mathbf{k}}(\mathbf{r}) = \sum_{m=1}^{N} \frac{1}{\sqrt{\Omega}} \exp\left\{\mathrm{i}\left(\mathbf{k}+\mathbf{G}_m\right)\mathbf{r}\right\}, \tag{3.17}$$

where $\Omega$ is the cell volume and $\mathbf{G}_m$ are reciprocal lattice vectors. In order to apply this approach practically, a finite basis set size has to be defined. This is done via choosing a *cut-off energy*. For each $\mathbf{k}$ in the Brillouin Zone, one includes only those plane waves with

$$|\mathbf{k}+\mathbf{G}| \leq \sqrt{2E_{\mathrm{cut}}}. \tag{3.18}$$

It is important to note that the number of plane waves depends on the volume of the Brillouin zone and therefore also on the volume of the unit cell. Accordingly, two calculations that were performed in two different unit cells employed a different number of plane wave basis functions and can not be directly compared - at least, as long as the calculations are not converged with respect to the basis set size (cut-off energy).

[1] This and the following paragraphs summarize knowledge that can be found in many quantum chemistry textbooks or publications. In particular, the text by R. Hoffmann [52], a collection by C. Pisani [53] and a lecture script by E. Pehlke [54] were useful.

**Brillouin Zone Integration** In a finite system, with $N$ unit cells and periodic boundary conditions, the sum over $N$ $\mathbf{k}$ points is an average over the electronic states. For example, the band contribution to the total energy is the average of the eigenvalues of the Kohn-Sham equations over the wave vectors. For $N \to \infty$, the sum over $N$ becomes an integral over the Brillouin Zone

$$\overline{f}_i = \frac{1}{N_k} \sum_{\mathbf{k}} f_i(\mathbf{k}) \Longrightarrow \overline{f}_i = \frac{\Omega}{(2\pi)^3} \int_{\mathrm{BZ}} f_i(\mathbf{k}) \mathrm{d}\mathbf{k}, \tag{3.19}$$

where $\Omega$ is the unit cell volume and $f_i(\mathbf{k})$ is a periodic function of $\mathbf{k}$. In practice, the integration is performed via sampling over a finite set of $N_k$ points. Following the Monkhorst-Pack approach [55], an equally spaced mesh of $\mathbf{k}$-points is created. The size can be determined by the user. The symmetry of the Bravais lattice is used to reduce the problem to a summation over $\mathbf{k}$ in the irreducible Brillouin Zone (IBZ) with relative weights $\omega_{\mathbf{k}}$. After choosing an irreducible zone of the reciprocal lattice, the weight $\omega_{\mathbf{k}}$ of a point is set to 1 if it is inside the IBZ. If on the other hand the point is outside, one needs to find the equivalent point inside the IBZ. If this point coincides with one of the points already found, the weight $\omega_{\mathbf{k}}$ of that point is increased by one. Otherwise, the point is considered as a new one and its weight is set to one [56]. The integration over the IBZ is then realized by

$$\overline{f}_i = \sum_{\mathbf{k}}^{\mathrm{IBZ}} \omega_{\mathbf{k}} f_i(\mathbf{k}). \tag{3.20}$$

**Pseudopotentials, the PAW method** Wavefunctions of valence electrons oscillate rapidly close to the nuclei, due to the requirement that they have to be orthogonal to core states. This behavior is difficult to describe with a finite basis set size (a given plane-wave cutoff energy). The *projector augmented-wave* method introduces valence pseudo wave functions that are smoothed out inside an augmentation sphere around each nucleus. In combination with the *frozen core* approximation, this allows for very efficient calculations without much loss of accuracy [57].

## 3.3 Jacob's Ladder and the PBE Functional

The exact exchange-correlation functional $E_{XC}[\rho(\mathbf{r})]$ is not known. Many different approaches to calculate the exchange-correlation contribution to the total energy are in use, but these approaches can not be improved systematically. Therefore, the development of new density functionals typically involves the fitting of at least some parameters in order to best reproduce some reference values from a test set. Even though, a qualitative ranking of different classes of functionals is in use [58]. It is based on the metaphor of "Jacob's ladder"; different classes of functionals are represented by rungs on a ladder that reaches from the "Hartree World" to the "heaven of chemical accuracy". The first four rungs that

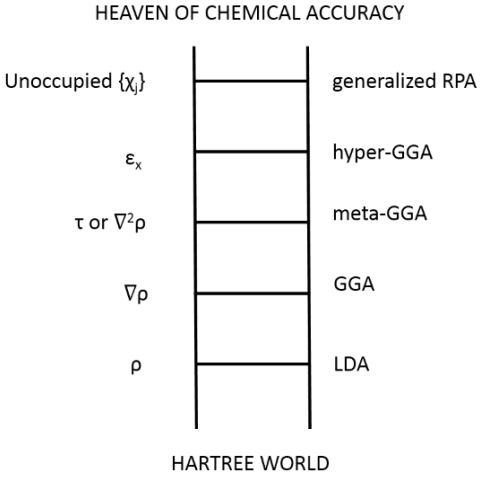


***Figure 3.1:*** *Jacob's ladder - a qualitative ranking of classes of DFT functionals. Reproduced from [59].*

are shown in Figure 3.1 are the *local density approximation* (LDA), the *generalized gradient approximation* (GGA), the *meta generalized gradient approximation* (metaGGA), the *hyper generalized gradient approximation* (hyper-GGA) [59]. The final, fifth rung is a generalized random phase approximation and is fully non-local.

In the work presented in this thesis, the Perdew-Burke-Ernzerhof (PBE) functional [60] was used. It belongs to the class of GGA functionals, where the exchange-correlation part $E_{XC}[\rho(\mathbf{r})]$ depends both on the local density $\rho(\mathbf{r})$ and its gradient $|\nabla\rho(\mathbf{r})|$. One key feature of the PBE functional is that it contains no empirically optimized parameters - which is not only an attractive feature from a puristic point of view, but also an advantage. By not being optimized to perform well for a specific set of chemical systems, the PBE functional

is very generally applicable.

One of the main problems of GGA functionals like PBE is the *self-interaction error*. It leads to over-delocalizaton of the electrons. In cases where this becomes a problem, one might use hybrid GGAs. Following the adiabatic connection [50], they introduce exact Fock exchange and thereby partially cancel out the self-interaction error. To do this, not only the local density and its gradient have to be evaluated, but the Fock exchange is calculated using the Kohn-Sham orbitals $\chi_i(\mathbf{r})$. Methods on the fifth rung on Jacob's ladder like ACFD-RPA (adiabatic connection fluctuation-dissipation [61, 62] - random phase approximation [63, 64]) also include unoccupied orbitals. The application of such methods at extended systems is yet prohibitively expensive.

How to choose the right functional for a project [65]? The philosophy that was followed for the work presented here was to use well-established functionals with few, or no empirical parameters, instead of choosing a different, highly parametrized functional for each new problem. Since the extremely wide-spread and well-known PBE functional (augmented by dispersion correction [27, 66]) performs quite well for the kind of problems that were dealt with, there was absolutely no reason to use more exotic functionals. Their possible advantage of producing data that might lie closer the experimentally derived values is outweighed by PBE's general advantage: it is very well known by the scientific community. Anyone with some experience in the field knows how to judge the results and how to compare them with other data.

Among many papers containing benchmarking information for density functionals, a very thorough study was done that investigates bond separation reactions of alkanes, employing a variety of different density functionals [67]. Reference values were obtained by CCSD(T) calculations with an estimation for the complete basis set limit. In this study, PBE, PBE-D2 and PBE-D3 exhibit MADs of 8.17, 1.24 and 4.78 $\mathrm{kJ\,mol^{-1}}$, respectively. In another very large benchmarking study, different density functionals with dispersion correction (DFT+D3) were investigated [68]. There, PBE's performance can be compared to other GGAs. Interestingly, for all of the test sets that were included in the study, PBE+D3 never gave either the best or the worst MAD. This certainly underlines the previous argu-

ment about the reliability of PBE. The weighted total mean absolute deviations (WTMAD) for PBE+D3 were found to be 21.7 kJ mol$^{-1}$, which is average for GGAs. For comparison, B3LYP+D3 has an WTMAD of 15.5 kJ mol$^{-1}$ in this study. These benchmarking studies employed test sets of molecular reactions etc. In this work, extended systems are of interest, not molecular ones. Especially important are the adsorption energies of small molecules in zeolites. A recent study compared calculated and experimental adsorption enthalpies for water, three alcohols and three nitriles in the zeolite H-ZSM 5 [69]. The study compares different DFT functionals, the effect of including dispersion correction and, in the case of PBE+D2, employing periodic boundary conditions. As can be seen in table 3.1, the inclusion of a dispersion correction is absolutely essential. The adsorption enthalpies calculated using PBE+D2 with periodic boundary conditions have a mean absolute deviation of 6 kJ mol$^{-1}$ from the experimental value which is only slightly worse than the value found for B3LYP+D2 (in cluster calculations) of 3 kJ mol$^{-1}$. These results

***Table 3.1:*** *Mean absolute deviations (MAD) in* kJ mol$^{-1}$ *between calculated and experimental adsorption enthalpies of selected molecules in H-ZSM 5. Summarized from [69].*

| Functional | D2 | D3 | pbc | MAD |
|---|---|---|---|---|
| B3LYP | - | - | - | 49 |
| | x | - | - | 3 |
| | - | x | - | 4 |
| M06-2X | - | - | - | 24 |
| | - | x | - | 12 |
| $\omega$B97X-D | | | - | 8 |
| PBE | - | - | - | 34 |
| | x | - | - | 7 |
| | - | x | - | 5 |
| | x | - | x | 6 |

certainly show a very nice performance of PBE+D2 for adsorption enthalpies in zeolites, which is exactly the kind of problem that is of relevance for this thesis.

Benchmark studies are one way to find out, whether a particular functional is suited to study a certain type of chemical problem. Fortunately for the work presented in this thesis, experimental findings were available at several points. The congruence of computational and experimental findings is certainly a most convincing observation that justi-

fies the selected approach - especially, if no highly parametrized functional was chosen in order to reproduce experimental values.

## 3.4 Exploration of the Potential Energy Surface

The Born-Oppenheimer approximation is the basis how we imagine chemical structures. In the Born-Oppenheimer approximation, the energy is expressed as a function of the nuclear coordinates $E(\mathbf{r}) = E[r_{x,1}, r_{y,1}, r_{z,1}, r_{x,2}, \ldots, r_{z,N}]$. $E(\mathbf{r})$ is called the potential energy surface (PES). Stable structure are minima on the PES, while transition states are first-order saddle points. In order to explore the PES, efficient tools have too be used, since its multi-dimensionality makes a rigorous exploration in all degrees of freedom impossible for all but the most simple cases. If nothing is known about the chemical structure that is to be found, global exploration techniques have to be applied (molecular dynamics, Monte Carlo approaches or, for example, genetic algorithms). For the work presented in this thesis, that methodology was not necessary, as chemical intuition or previous results could be used for educated guesses and gave reasonable starting structures for local optimizations. [1]

In order to find the optimized structure of a given chemical system, *chemical intuition* can often be very helpful in finding an initial guess for that structure. Starting from there, one can employ local optimization techniques such as *steepest decent*, *conjugate gradient*, or *quasi-Newton* algorithms. For the work presented in this thesis, the conjugate gradient was used for most cases. It begins with a steepest decent step:

$$\mathbf{r}_1 = \mathbf{r}_0 + \alpha \mathbf{h}_0 \tag{3.21}$$

where $\alpha$ is a scaling factor and $\mathbf{h}_n = \mathbf{g}_n = -\nabla E(\mathbf{r}_n)$, the gradient of the potential energy at the point $\mathbf{r}_n$, establishes a vector by which the coordinates $\mathbf{r}_n$ are changed in order to get to the next point on the PES, $\mathbf{r}_{n+1}$. In all following steps, this process is repeated, but

[1] Potential energy surfaces and their exploration are discussed in detail in the book by D. Wales [70]. For an overview over all these methods, see also the dissertation thesis of R. Włodarczyk [71].

each new vector is forced to be conjugate to previous change vectors [72]

$$\mathbf{h}_{n+1} = \mathbf{g}_{n+1} + \gamma_{n+1}\mathbf{h}_n, \tag{3.22}$$

where, in the Polak-Ribiere method:

$$\gamma_{n+1} = \frac{(\mathbf{g}_{n+1} - \mathbf{g}_n)\,\mathbf{g}_{n+1}}{|\mathbf{g}_n|^2}. \tag{3.23}$$

The conjugate gradient algorithm is both efficient and stable. It avoids the problem of oscillating behavior in narrow "valleys" of the PES that can be a problem with the steepest decent algorithm.

In case the conjugate gradient optimization does not lead to a local minimum (performing a vibrational analysis show remaining imaginary frequencies), it can become necessary to give the optimization a "nudge" in the direction that leads out of the transition structure - either manually, or automatically, by performing a step along the eigenvector that belongs to the vibrational mode with the imaginary frequency. This technique was employed a few times for the work that is presented in this thesis. It will not be explicitly mentioned in the following, since it is a well-known standard technique.

## 3.5 Vibrational Structure Analysis

Understanding the vibrational properties of molecules has many applications.[1] Calculated vibrational frequencies can be compared to experimental infrared spectra and give insights about the vibrational modes associated with the observed spectral properties. Also, a precise knowledge of the vibrational structure is necessary when trying to calculate the vibrational partition function in statistical thermodynamics, in order to get the entropy. As was the case for the exploration of the potential energy surface, it is typically within the framework of the Born-Oppenheimer approximation that we think about the

[1] This chapter summarizes concepts that can be found in many quantum chemistry textbooks. It is based in particular on sections of the book by P. Polavarapu [73].

vibrational structure of molecules.

**The Harmonic Oscillator Approximation** The potential energy $V$ can be expressed as a Taylor expansion about $\mathbf{r}_0$:

$$\begin{aligned} V(\mathbf{r}) = V(\mathbf{r}_0) &+ \sum_{i}^{3N} \left( \frac{\partial V(\mathbf{r})}{\partial r_i} \right)_{\mathbf{r}_0} (r_i - r_{i,0}) \\ &+ \frac{1}{2!} \sum_{i,j}^{3N} \left( \frac{\partial^2 V(\mathbf{r})}{\partial r_i \partial r_j} \right)_{\mathbf{r}_0} (r_i - r_{i,0})(r_j - r_{j,0}) \\ &+ \dots . \end{aligned} \tag{3.24}$$

Starting from a minimum energy structure, $\mathbf{r}_0$ is a minimum of $V$, so the first derivatives are zero. If the Taylor expression is terminated after the second order term, the result is known as the harmonic approximation. The vibrational energy can now be expressed as

$$E_{\text{vib}} = \frac{1}{2} \sum_{a}^{N} \mathrm{m}_a (v_x^2 + v_y^2 + v_z^2) + \frac{1}{2} \sum_{i,j}^{3N} \left( \frac{\partial^2 V(\mathbf{r})}{\partial r_i \partial r_j} \right)_{\mathbf{r}_0} (r_i - r_{i,0})(r_j - r_{j,0}), \tag{3.25}$$

where $\mathrm{m}_a$ are the atomic masses and

$$v_i = \frac{\mathrm{d}r_i}{\mathrm{d}t} = \dot{r}_i \tag{3.26}$$

are the velocities. Introducing root-mass-weighted coordinates

$$\xi_i = \sqrt{\mathrm{m}_i}(r_i - r_{i,0}) \tag{3.27}$$

allows for a rewriting of the expression for the vibrational energy:

$$E_{\text{vib}} = \frac{1}{2} \sum_{i}^{3N} \dot{\xi}^2 + \frac{1}{2} \sum_{i,j}^{3N} \left( \frac{\partial^2 V(\boldsymbol{\xi})}{\partial \xi_i \partial \xi_j} \right)_{\boldsymbol{\xi}_0} \xi_i \xi_j. \tag{3.28}$$

Expressed as a matrix equation with **H** as the mass-weighted Hessian or force constant matrix

$$E_{\text{vib}}(\boldsymbol{\xi}) = \frac{1}{2}\dot{\boldsymbol{\xi}}^{\dagger}\dot{\boldsymbol{\xi}} + \frac{1}{2}\boldsymbol{\xi}^{\dagger}\mathbf{H}\boldsymbol{\xi}, \tag{3.29}$$

the vibrational frequencies $\omega_i$ are obtained after diagonalization of **H** as

$$\mathbf{L} = \begin{vmatrix} \omega_1^2 & 0 & 0 & \dots & 0 \\ 0 & \omega_2^2 & 0 & \dots & 0 \\ \vdots & \vdots & \vdots & \ddots & \vdots \\ 0 & 0 & 0 & \dots & \omega_{3N}^2 \end{vmatrix}, \tag{3.30}$$

where **L** is obtained after finding the matrix **A** that diagonalizes the mass-weighted Hessian **H**:

$$\mathbf{L} = \mathbf{A}^{\dagger}\mathbf{H}\mathbf{A}. \tag{3.31}$$

The columns of $\mathbf{A}^{\dagger}$ are the eigenvectors of **H** and specify the normal mode coordinates

$$q_j = \sum_{i=1}^{3N} A_{ij}\xi_i \tag{3.32}$$

in which the vibrational movement of the atoms can be described in a natural way. In the harmonic approximation, the normal mode coordinates oscillate independently of each other:

$$q_j(t) = b_j \cos(\omega_j t + \phi_j). \tag{3.33}$$

For the prediction of IR spectra, the calculated $\omega_i$ can be inserted into the known solution for the quantum harmonic oscillator problem:

$$E_n = \hbar\omega\left(n + \frac{1}{2}\right). \tag{3.34}$$

The frequencies in $\mathrm{s}^{-1}$ are typically expressed as wavenumbers in $\mathrm{cm}^{-1}$ via

$$\omega_{\text{wavenumber}} = \frac{\omega_{\text{frequency}}}{2\pi \mathrm{c}}, \tag{3.35}$$

where c is the speed of light.

**IR Intensities; the Double Harmonic Approximation** For comparison with experimental IR spectra, it is of interest to calculate the electric dipole transition moments for a transition from vibrational state $\nu_n$ to $\nu_{n+1}$, to which the IR intensities are proportional:

$$\boldsymbol{\mu}_{\nu'\nu} = \langle \Psi^0_{\nu'} | \boldsymbol{\mu} | \Psi^0_{\nu} \rangle \,. \tag{3.36}$$

Formulating the electric dipole moment operator $\boldsymbol{\mu}$ as a Taylor expansion in normal mode coordinates about the reference geometry and truncating the series to the first power in the *electrical harmonic approximation* gives

$$\boldsymbol{\mu} = \boldsymbol{\mu}_0 + \left(\frac{\partial \boldsymbol{\mu}}{\partial \mathbf{q}}\right)_{\mathbf{q}_0} \mathbf{q}. \tag{3.37}$$

In combination with harmonic oscillator wavefunctions, eq. 3.37 is referred to as the *double harmonic approximation*. Inserting eq. 3.37 into eq. 3.36 gives

$$\boldsymbol{\mu}_{\nu'\nu} = \boldsymbol{\mu}_0 \delta_{\nu\nu'} + \left(\frac{\partial \boldsymbol{\mu}}{\partial \mathbf{q}}\right)_{\mathbf{q}_0} \left\{ \left(\frac{\nu+1}{2}\right)^{\frac{1}{2}} \delta_{\nu',\nu+1} + \left(\frac{\nu}{2}\right)^{\frac{1}{2}} \delta_{\nu',\nu+1} \right\}, \tag{3.38}$$

with

$$\delta_{\nu\nu'} = \begin{cases} 1, & \text{if } \nu = \nu', \\ 0, & \text{if } \nu \neq \nu'. \end{cases} \tag{3.39}$$

This is the reason for the selection rules, stating that within the double harmonic approximations, only the so-called "fundamentals", $\nu \rightarrow \nu \pm 1$, have non-zero transitions.

Many of the chemical systems of interest in this thesis are thin films on metal substrates. For such systems, *surface selection rules* have to be considered. The adsorbed film (or adsorbed molecule) induces opposite image charges in the substrate. The dipole moment of the molecule and the image charges perpendicular to the surface reinforce each other. In contrast, the dipole moments of the molecule and the image charges parallel to the surface cancel out. Therefore, only vibrational modes associated with a non-zero

transition dipole moment perpendicular to the surface will be observed in the vibrational spectrum [74].

**Numerical Derivatives** For computational purposes, both the components of the Hessian **H** and the dipole moment derivatives can be calculated numerically, for example with a central finite difference method with one displacement step in each direction for all $r_i$. This is the way how the force constants for the harmonic vibrational modes and the predicted relative IR intensities were obtained for most cases in this thesis.

**Sources of Errors, Anharmonicities** In the work presented in this thesis, the adsorption of CO and other probe molecules at acidic hydroxyl groups was investigated and the vibrational modes had to calculated. Here, one encounters two different sources of errors:

1. The potential energy surface along the O-H bond is described inaccurately with the GGA functional that is employed.

2. The vibrational mode of interest is not well described using the harmonic approximation.

Usually, harmonic force constants and frequencies are higher than the experimentally observed quantities and since the errors in the calculations are largely systematic, empirical scaling factors can be used to correct the computed values [75]. For the case of hydrogen-bonded systems, this treatment is not always sufficient. The Perdew-Burke-Ernzerhof (PBE functional [60, 76] that was employed tends to overestimate hydrogen-bonded interactions, leading to overbinding [77]. In addition, it may be necessary to go beyond the harmonic approximation. Solving the one-dimensional Schrödinger equation on a numerical grid for several values of $r_{\mathrm{OH}}$ around the equilibrium distance allows the calculation of anharmonic OH stretching frequencies by treating the O-H stretching vibration as decoupled from the rest. A $\omega / r_{\mathrm{OH}}$ correlation scheme can be applied for the case of CO adsorbed on bridging hydroxyls Si-O(H)-Al in zeolites. Together, this results in a simple

linear formula for the anharmonic frequency [78, 79]:

$$\nu_{\mathrm{OH}}^{\mathrm{Nachtigall}} = a \times r_{\mathrm{OH}} + b + \Delta_{\mathrm{CC}}, \tag{3.40}$$

where $\Delta_{\mathrm{CC}}$ is a correction for the remaining error of the CCSD(T) method that was used in the parametrization to get the single point energies for several values of $r_{\mathrm{OH}}$. $a, b$ and $\Delta_{\mathrm{CC}}$ are parameters that have to be obtained using a test set of zeolite clusters with adsorbed CO. In this work, the parameters obtained by Nachtigall [79] for the PBE functional were used: $a = -13\,165.306\,\mathrm{cm}^{-1}\,\mathrm{Å}^{-1}$, $b = 16\,522.1\,\mathrm{cm}^{-1}$ and $\Delta_{\mathrm{CC}} = -50\,\mathrm{cm}^{-1}$. An analogous formula can also be used for the calculation of the frequency of the C-O stretching mode:

$$\nu_{\mathrm{CO}}^{\mathrm{Nachtigall}} = a \times r_{\mathrm{OH}} + b + \Delta\nu, \tag{3.41}$$

with $a = -8582.336\,\mathrm{cm}^{-1}\,\mathrm{Å}^{-1}$, $b = 11\,975.4\,\mathrm{cm}^{-1}$ and $\Delta\nu = -29\,\mathrm{cm}^{-1}$.

# 4 Results

## 4.1 Ultrathin Ti-Silicate Film on a Ru(0001) Surface

DFT calculations give insight into possible structures of ultrathin Ti-doped silicate films prepared on a Ru(0001) surface. The computational results are then compared to the experimentalists' findings obtained by the analytical tools of surface science. Theory and experiment in concert allow the characterization of experimentally prepared Ti-silicate films. A homogeneous substitution of Si by Ti in the silicate bilayer frame is energetically unfavorable: the film laterally segregates into two phases (domains), a pure silica doublelayer and a Ti-silicate doublelayer. The DFT calculations reveal that the Ti-silicate film with an Ti/Si = 1:1 ratio consists of a monolayer of [$SiO_4$] tetrahedra on top, connected via shared oxygen atoms to the bottom layer of [$TiO_6$] octahedra. Similar structures are known for naturally occuring phyllosilicates and a recently prepared Fe-silicate film [43]. The modeling of the Ti-silicate film followed a methodology similar to the approach that was used and recently reported for the investigation of these Fe-silicate films [43]. The DFT calculations predict formation of bridging Ti-O-Ru bonds between the Ti-silicate film and the Ru substrate. These findings give insight into the chemistry of substituted silica bilayers, which are interesting model systems in surface chemistry.[1]

### 4.1.1 Computational Details

All calculations were based on density functional theory with periodic boundary conditions and carried out using the Vienna ab initio simulation package (VASP) [80, 81], along

[1] This chapter is based on the joint publication [FDF3] and contains direct excerpts.

with the projector augmented wave (PAW) method [57, 82]. We applied the PBE functional [60, 76]. A 400 eV cutoff for the plane wave basis set and an $8 \times 4 \times 1$ Monkhorst-Pack grid [55] for the integrations of the first Brillouin zone were used. The surface slabs were modeled using the cell parameters of the silica double layer on Ru(0001) ($539.6 \times 934.6$ pm) [83, 84] containing five Ru layers, with the three top layers allowed to relax and two bottom layers fixed to their bulk positions. The positions of the nuclei were relaxed until the forces were smaller than $0.005\,\mathrm{eV\,\AA^{-1}}$. A central finite difference method with 2.0 pm displacements in each Cartesian direction was used to obtain the harmonic force constants, after re-optimization of the structures with the PBE functional augmented with a semi-empirical $^1/_{r^6}$ dispersion term (PBE+D) [27, 66]. The intensities were obtained from the derivatives of the dipole moment component perpendicular to the surface. To compensate for systematic errors of DFT, the vibrational frequencies are scaled by a factor of 1.0341 derived from a comparison between experimental and calculated frequencies for $\alpha$-quartz [83].

### 4.1.2 Exploration of Possible Structures

The bilayer silica film [83, 84] with a $Si_8O_{16} \cdot 2\,O/Ru$ composition in the $(2 \times 2)$ unit cell was the starting point for the DFT calculations. To investigate possible substitution patterns systematically, one to four Si atoms of the bilayer unit cell were replaced by Ti atoms. This was done in four steps. In the first step, all eight possible structures of $TiSi_7O_{16} \cdot 2\,O/Ru$ that can be formed by substituting Ti for one of the eight Si atoms in the unit cell were optimized and examined. The energetically most favored structure was taken as a starting point to investigate possible substitution locations for the next Ti atom to create $Ti_2Si_6O_{16} \cdot 2\,O/Ru$ and so on. By iterative replacement of more Si atoms, other $Ti_nSi_{8-n}O_{16} \cdot 2\,O/Ru$ structures were created and then optimized. In the end, eight structures (substitution patterns) were compared for one Ti atom per unit cell. Eight structures were examined for two Ti atoms per unit cell, seven for three Ti atoms and finally 16 different substitution patterns were created for the case where half of the Si atoms were

replaced by Ti atoms. Here, some extra structures were considered in addition to those obtained by the procedure that was explained above. This approach of subsequent substitutions to find the most stable structures for varying numbers of heteroatoms that are substituted for Si atoms in the silica bilayer has also been successfully applied by Włodarczyk et al. to find the correct structure for Fe-substituted silica bilayers [43]. This methodology includes several assumptions. First of all, we assume that the cell constants of the Ti-substituted films do not differ from those of the pristine film. However, note that De Man et al. found that the cell volume of zeolites increases upon Ti-substitution [85]. In addition, we assumed that the orientation of the film does not change in respect to the Ru substrate. A unit cell that accommodates for a possible rotation would have to be significantly larger and therefore computationally much more demanding. The scheme of replacing Si with Ti atoms subsequently also includes one additional, major assumption. It is based on the idea of the general structure staying intact which means that coordination numbers do not change and bond angles etc. also do not change too much. As will be seen, this assumption does not hold true. The results are documented in table 4.1. It shows the relative energies for the structures that were investigated for four degrees of Ti-Substitution, going from one to four Ti-atoms per unit cell, which translates to 12.5 % to 50 % Ti-substitution. For morphological substitutions of one, two and three Ti atoms per unit cell (u.c.), the energies per unit cell for all structures found were within 1.3 , 23 and 7 $\mathrm{kJ\,mol^{-1}}$, respectively, as can be seen in table 4.1. Figure 4.1 shows the resulting, most stable structures for 12.5 %, 25 %, 37.5 % and 50 % substitution of the Si atoms by Ti. The substitutions of one or two Si atoms by Ti per unit cell (u.c.) preserve the bilayer structure; that is, it is isomorphous. The energies per unit cell for all structures found were within 1.3 and 23 kJ/mol, respectively for the different isomorphous substitution patterns. The lowest energy structures found for $Ti_3Si_5O_{16} \cdot 2\,O/Ru$ and $Ti_4Si_4O_{16} \cdot 2\,O/Ru$ are qualitatively different. The energies per unit cell of the structures shown in Figure 4.1c,d were 68 and 217 $\mathrm{kJ\,mol^{-1}}$ lower than structures with the same composition that did more closely resemble the original bilayer structure, similarly to those of lower Ti content.

Table 4.2 compares structural details of the pristine silica layer on top of the Ru(0001)

***Table 4.1:*** *Relative energies $\Delta E$ in* kJ mol$^{-1}$ *per unit cell for $Ti_nSi_{8-n}O_{16} \cdot 2O/Ru$ with with $n \in \{1,2,3,4\}$. Structures marked with an asterisk $*$ are not isomorphous substitutions in the bilayer structure.*

| $TiSi_7O_{16} \cdot 2O/Ru$ | | $Ti_2Si_6O_{16} \cdot 2O/Ru$ | | $Ti_3Si_5O_{16} \cdot 2O/Ru$ | | $Ti_4Si_4O_{16} \cdot 2O/Ru$ | | | |
|---|---|---|---|---|---|---|---|---|---|
| Structure | $\Delta E$ | Structure | $\Delta E$ | Structure | $\Delta E$ | Structure | $\Delta E$ | Structure | $\Delta E$ |
| 1 | 0.0 | 1 | 0.0 | 1* | 0.0 | 1* | 0.0 | 9 | 226.9 |
| 2 | 0.0 | 2 | 0.0 | 2 | 68.0 | 2 | 217.3 | 10 | 227.5 |
| 3 | 0.5 | 3 | 5.1 | 3 | 68.0 | 3 | 221.5 | 11 | 228.7 |
| 4 | 0.6 | 4 | 7.3 | 4 | 68.3 | 4 | 222.1 | 12 | 229.0 |
| 5 | 1.3 | 5 | 17.5 | 5 | 68.7 | 5 | 223.0 | 13 | 230.5 |
| 6 | 1.3 | 2 | 18.0 | 6 | 74.4 | 6 | 223.8 | 14 | 230.6 |
| 7 | 1.3 | 7 | 23.3 | 7 | 75.3 | 7 | 225.3 | 15 | 243.5 |
| 8 | 1.3 | 8* | 99.7 | | | 8 | 225.9 | 16 | 253.6 |

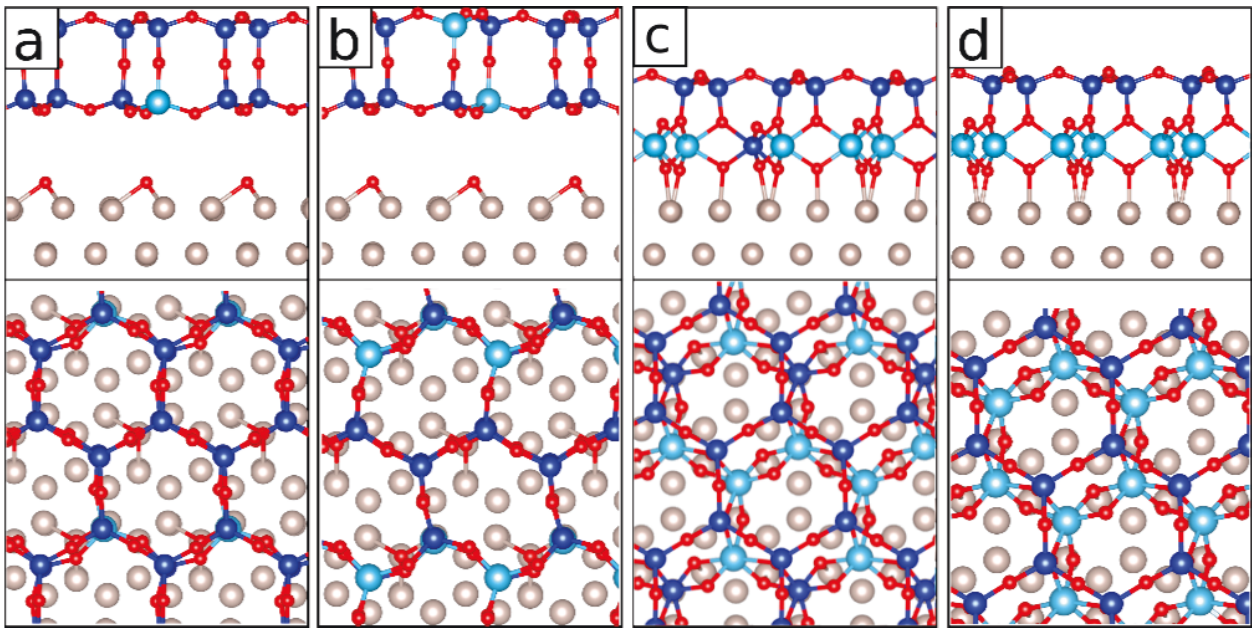


***Figure 4.1:*** *Top and side views of the most stable structures found by DFT at various Ti/Si ratios. (a) $TiSi_7O_{16} \cdot 2\,O/Ru$, (b) $Ti_2Si_6O_{16} \cdot 2\,O/Ru$, (c) $Ti_3Si_5O_{16} \cdot 2\,O/Ru$, (d) $Ti_4Si_4O_{16} \cdot 2\,O/Ru$. Si, blue; Ti, light blue; O, red; Ru, grey. The figure is taken from [FDF3].*

surface with the global minimum structure of $Ti_4Si_4O_{16} \cdot 2\,O/Ru$ (Figure 4.1d), which does no longer resemble the bilayer structure. The topmost layer rather resembles silica monolayers, as observed on Ru(0001), Mo(112), and SiC(0001) [37, 38] in which all Si atoms are fourfold coordinated to oxygen atoms. The bottom layer consists of edge-sharing $[TiO_6]$ octahedra, which share corners with the $[SiO_4]$ tetrahedra of the top layer. The three oxygen atoms of the $[TiO_6]$ octahedra that are closest to the Ru surface are within 202 - 205 pm of the next Ru atoms, while their distance to Ti is 197 to 203 pm. In the case of the structure of $Ti_4Si_4O_{16} \cdot 2\,O/Ru$, the surface oxygen atoms and the oxygen atoms that originally belonged to the bilayer cannot be differentiated. The Ti atoms of the bottom layer are now connected to the Ru surface via oxygen atoms. This situation is shown in Figure 4.2. Figure 4.2 demonstrates that there are three different types of O atoms connected to Ti atoms: firstly, twofold coordinated O atoms connected to two Ti atoms; secondly, threefold coordinated O atoms connecting to two Ti atoms and one Si atom; thirdly, threefold coordinated O atoms connecting to two Ti atoms and one Ru atom of the metal surface. This is still in agreement with the assumption of formal charges of for Ti and Si and for O. Formally, one might assign a charge of $+^2/_3$ per Ru atom that is

***Table 4.2:*** *Comparison of selected distances[a] (in pm) calculated for* $Si_8O_{16} \cdot 2\,O/Ru$ *and* $Ti_4Si_4O_{16} \cdot 2\,O/Ru$ *(Figure 4.1d).*

| distance | $Si_8O_{16} \cdot 2\,O/Ru$ | $Ti_4Si_4O_{16} \cdot 2\,O/Ru$ |
|---|---|---|
| $r(O_{surface} - Ru)$ | 202-203 | 202-205 |
| $r_z(O_{surface} - Ru)$ | 117 | 200 |
| $r_z(O_{surface} - O_{layer})$ | 322 | - |
| $r(O_{surface} - Ti_{layer})$ | - | 197-203 |

[a] $r(O_{surface} - Ru)$ is the distance of surface oxygen atoms to the Ru atoms they are bound to, $r_z(O_{surface} - Ru)$ is the distance between the plane parallel to the Ru-surface, going through the topmost layer of Ru atoms and the parallel plane containing the closest surface oxygen atoms, $r_z(O_{surface} - O_{layer})$ is the distance between the plane parallel to the Ru surface, containing the topmost surface oxygen atoms and the parallel plane containing the lowest oxygen atoms of the bilayer that are closest to the surface and $r(O_{surface} - Ti_{layer})$ is the bond distances for the Ti-O bonds connecting Ti atoms to the lowest layer of oxygen atoms.

directly connected to O. The positive charge of the Ru substrate will be delocalized in the bulk of the metallic substrate.

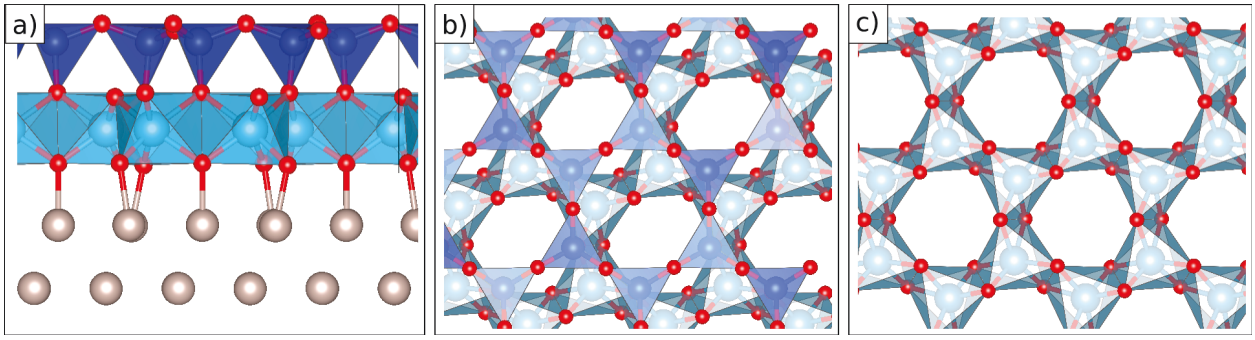


***Figure 4.2:*** *Views of the most stable structure found for the* $Ti_4Si_4O_{16} \cdot 2\,O/Ru$ *unit cell. (a) side view, polyhedral representation; Si, blue; Ti, light blue; O, red; Ru, grey. (b) top view. (c) top view of only the layer formed by* $[TiO_6]$ *units. The figure is taken from [FDF3].*

Layered silicates are known as phyllosilicates. Phyllosilicates have the basic unit $Si_2O_5^{2-}$ . A typical arrangement can be seen in talc $Mg_3Si_4O_{10}(OH)_2$. It is composed of silicate ($Si_2O_5^{2-}$) sheets with magnesium $Mg^{2+}$ ions sandwiched between sheets in octahedral sites. The silicate layer consists of interconnected six-membered rings of $[SiO_4]$ tetrahedra extending outward to form the tetrahedral (T) layer. Every tetrahedron is connected to others by three of its oxygen atoms. The unshared oxygen atoms of all tetrahedra are orientated towards the same side where the octahedral (O) layer is formed by the $Mg^{2+}$ ions with $OH^-$ occupying two out of six corners of each octahedron. Each $OH^-$ is shared by three of these octahedra. Apical oxygen atoms from the T layer above occupy

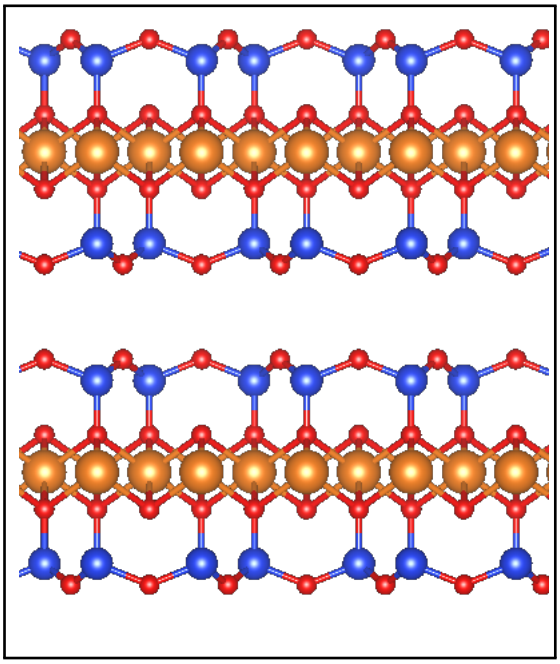

***Figure 4.3:*** *Crystal structure of talc, $H_2Mg_3O_{12}Si_4$ (taken from the literature [86]). The positions of the hydrogen atoms are not shown. Si, blue; Mg, bronze; O, red. The figure is taken from [FDF3].*

two other corners, the remaining two are occupied by two apical oxygen atoms from the T layer below. Thus, an overall T-O-T layer is formed. It can bind to other T-O-T layers via weak Van der Waals interactions. This gives the phyllosilicates their crystallographic cleavage plane parallel to the layers. Our structure has obvious similarities to these systems. As can be seen in Figure 4.2, the Ti atoms are coordinated octahedrally, forming the O layer. Apical oxygen atoms of [$SiO_4$] tetrahedra of the layer above occupy two of the corners of the octahedra. This silica layer has the same structure as the "T" layer in phyllosilicates, it shares the overall composition of $Si_2O_5^{2-}$. Oxygen atoms that connect to the Ru substrate fill up the three remaining corners of the [$TiO_6$] octahedra. Instead of $OH^-$ ions that are shared by three octahedra in the case of talc, there are now oxygen atoms shared by only two octahedra. Layered titanosilicates also appear in a class of minerals called heterophyllosilicates (e.g., Bafertisite or Nafertisite [87]). Like phyllosilicates, they have "T-O-T" layers. However, beyond this structural features and the general fact that titanium ions are included there are no other similarities to the titanosilicate film that is described in this work. In the heterophyllosilicates, the $Ti^{4+}$ ions do not form the centers of the octahedral layer. Rows of Ti-polyhedra are substituted periodically for rows of

Si-tetrahedra within the tetrahedral layer.

### 4.1.3 Stability and Vibrational Spectra

For understanding the effect on the bilayer structure at a given Ti content, segregation reactions have to be considered. At 0 % Ti content, a pristine silica film is formed. At 50 % Ti content, the structure for $Ti_4Si_4O_{16} \cdot 2\,O/Ru$ is preferred as has been described above. The obvious questions is what happens at a Ti content between 0 and 50 %? For Fe-substituted silica films, phase segregation into Fe-containing and pure silica domains takes place [43]. For the case of Ti-substituted silica films that is considered here, equations 4.1 to 4.4 show the segregation reactions and the associated energies[1] which are estimated from total slab energies.

$$2\,TiSi_7O_{16} \cdot 2\,O/Ru \longrightarrow Ti_2Si_6O_{16} \cdot 2\,O/Ru + Si_8O_{16} \cdot 2\,O/Ru, \quad \Delta E = -11\,kJ\,mol^{-1} \tag{4.1}$$

$$3\,TiSi_7O_{16} \cdot 2\,O/Ru \longrightarrow Ti_3Si_5O_{16} \cdot 2\,O/Ru + 2\,Si_8O_{16} \cdot 2\,O/Ru, \quad \Delta E = -73\,kJ\,mol^{-1} \tag{4.2}$$

$$4\,TiSi_7O_{16} \cdot 2\,O/Ru \longrightarrow Ti_4Si_4O_{16} \cdot 2\,O/Ru + 3\,Si_8O_{16} \cdot 2\,O/Ru, \quad \Delta E = -227\,kJ\,mol^{-1} \tag{4.3}$$

$$4\,Ti_3Si_5O_{16} \cdot 2\,O/Ru \longrightarrow 3\,Ti_4Si_4O_{16} \cdot 2\,O/Ru + 3\,Si_8O_{16} \cdot 2\,O/Ru, \quad \Delta E = -390\,kJ\,mol^{-1} \tag{4.4}$$

Whereas equation 4.1 shows a small energy gain for phase segregation into Ti-enriched ($Ti_2Si_6$) and pure silica domains, equations 4.2 and 4.3 show a much larger energy gain for the segregation of layers with isolated tetrahedrally coordinated Ti atoms ($TiSi_7$) in the unit cell into a pure silica film and a film containing three and four, respectively, octahedrally coordinated Ti atoms in the bottom layer and four tetrahedrally coordinated Si atoms in the top layer. This energy gain is particularly large for the formation of the

[1] The reactions energies refer to the stoichiometry as written in the equations.

$Ti_4Si_4$ film, which results in a large energy gain also for the segregation of the $Ti_3Si_5$ film into a $Ti_4Si_4$ and a pure silica film. Therefore, even at low Ti content, the structural and spectral characteristics of the $Ti_4Si_4$ film should be observed.

Figure 4.5 shows the harmonic IRA spectra simulated for the most stable $Ti_4Si_4O_{16} \cdot 2\,O/Ru$ structure (50 % Ti, Figure 4.1d and 4.2) and for the pristine silica bilayer containing 0 % Ti. Only modes above $600\,cm^{-1}$ will be discussed here since only those can be compared with the experimental observations. The peak at $1302\,cm^{-1}$ is very characteristic for the bilayer structure [37]. The corresponding vibrational mode is a symmetrical stretching of the interlayer Si-O-Si linkages. The vibrational mode at $654\,cm^{-1}$ is a bending mode of the intralayer Si-O-Si bonds. The spectrum for the $Ti_4Si_4O_{16} \cdot 2\,O/Ru$-system is qualitatively different. The most prominent vibrational mode at $1003\,cm^{-1}$ does not involve the Ti atoms that constitute the bottom layer. The mode solely describes a stretching of the Si-O bonds perpendicular to the surface (see Figure 4.1d).

### 4.1.4 Comparison with Experimental Observations

All experiments on the Ti-silicate films which are referred to in this thesis were carried out by X. Yu, J. A. Boscoboinik and S. Shaikhutdinov in the group of H.-J. Freund at the Fritz-Haber-Institut, Berlin. The thin film synthesis and the subsequent characterization were done in were carried out in an ultrahigh vacuum (UHV) chamber and followed in general the methodology that was developed for other ultrathin silica films [37]. The experimental details are described in the joint publication [FDF3]. Selected experimental results are cited from this work and are discussed in the following for better understanding and comparison with the theoretical results outlined above. Low energy electron diffraction (LEED) patterns clearly indicate formation of well-ordered films. In addition to pure silica surface that shows a $(2 \times 2)$ symmetry with respect to the Ru(0001) surface, a new structure with a $(\sqrt{3} \times \sqrt{3})R30^\circ$ unit cell develops as the Ti:Si ratio increases (see Figure 4.4a and 4.4b). A high-resolution scanning tunneling microscopy (STM) image (Figure 4.4c) reveals a honeycomb-like surface. This is so far in nice agreement with the computational

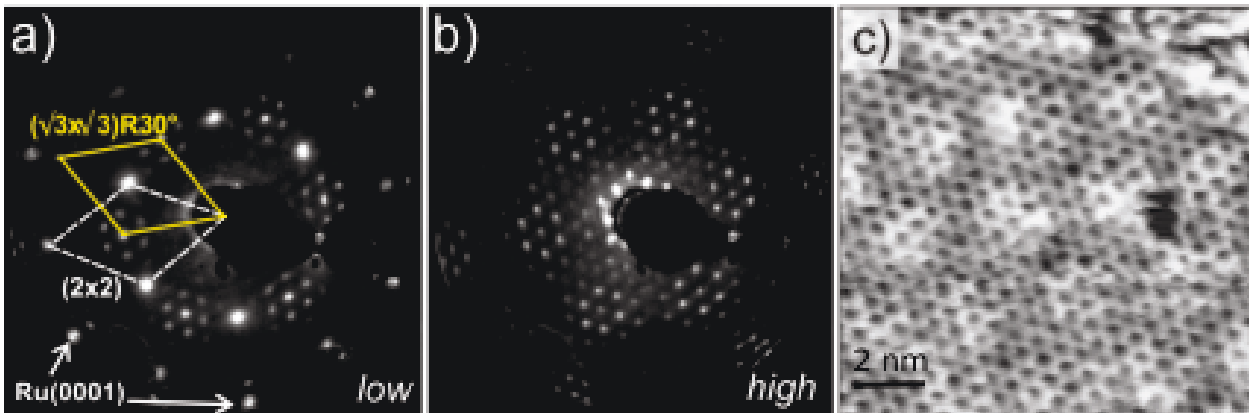


***Figure 4.4:*** *Microscopic and spectroscopic characterization of the Ti-Silicate films. (a,b) LEED patterns (60 eV) of the Ti-silicate films at low (a) and high (b) Ti content in the films. The* $(2 \times 2)$ *and* $(\sqrt{3} \times \sqrt{3})R30°$ *unit cells are indicated. The principal spots of the Ru(0001) surface are marked by arrows. (c) High-resolution STM image of a Ti-silicate film showing a honeycomb-like surface structure. The Moiré structure resulting in a long-range surface modulation is also seen. Tunneling conditions: sample bias 1.5 V, current 0.1 nA. These data were obtained by the experimental partners. The figure is taken from [FDF3].*

findings. There are now two different structures present at the surface, the pristine silica films and a new structure which is rotated with respect to the Ru(0001) surface compared to the pristine silica film. This rotation of the film with respect to the surface was expected, but not accommodated for in the calculations as was explained in subsection 4.1.2. Water adsorption experiments showed only Si-OH and no Ti-OH in experimental IRA spectra, a finding that agrees with the theoretical prediction that Ti atoms occupy exclusively the bottom layer and thus, are not available for hydroxylation. IRAS has also been shown to be very sensible towards the nature of silica films [37]. A good test to see whether the structure that was proposed based on calculations might be a good model for the experimentally observed structure is to compare experimental and computationally predicted vibrational spectra. This is done in Figure 4.5. The pure bilayer $SiO_2$ film is characterized by very strong and sharp phonon bands at $\sim$ 1300 $cm^{-1}$ and $\sim$ 693 $cm^{-1}$, which were observed here also for the films at relatively low Ti:Si ratios (see the top spectrum in Figure 4.5). However, an additional band centered at $\sim$ 1022 $cm^{-1}$ appeared upon Ti doping, which dominates the spectrum at high Ti:Si ratios, whereas the spectral features of bilayer silica attenuate accordingly and disappear with rising Ti content. Vibrational modes of similar frequencies were observed for silica monolayers grown on Mo(112) and Ru(0001) [88]. The Fe-silicate film that has recently been reported exhibited a similar vi-

brational mode as well [43]. Low intensity spectral features in the frequency region below $\sim 700\,\mathrm{cm}^{-1}$, which is near the absorption cut-edge of the KBr windows used in the experimentalists' spectrometer, were difficult to determine precisely in these experiments and resulted in baseline problems as can be seen in the experimental spectrum for the film with high Ti content. The clear agreement of calculated and observed IRA spectra supports the proposed structural model. An important, additional check had to be done to exclude the possibility that pristine titanium oxide domains are formed. The experimentalists have prepared $TiO_x$ films. The IRA spectra for these films (not shown here) showed none of the features that are observed for the Ti-silicate films. Thus, the formation of alone-standing $TiO_x$ structure can be excluded for the case of the Ti-silicate films.

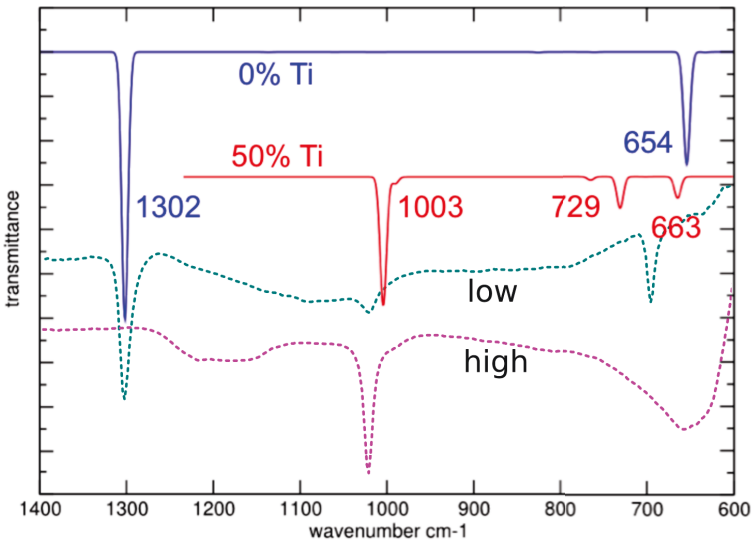


***Figure 4.5:*** *IRA spectra simulated for 0% Ti ($Si_8O_{16} \cdot 2\,O/Ru$) and 50% Ti ($Ti_4Si_4O_{16} \cdot 2\,O/Ru$). The spectra are scaled by a factor of 1.0341 [83] and compared to the experimentally observed spectra (dotted lines) obtained for both low and high Ti content. The figure is taken from [FDF3].*

### 4.1.5 Conclusions

Combining experimental techniques with DFT structure and stability predictions resulted in structural model for a well-ordered, ultrathin Ti-silicate film on a Ru(0001) surface. The film can best be described as a monolayer of corner-sharing $[SiO_4]$ tetrahedra on top of a monolayer formed by $[TiO_6]$ octahedra. The layers are connected by shared oxygen

atoms at the corners of the [$SiO_4$] tetrahedra and [$TiO_6$] octahedra in the top and bottom layers, respectively. The [$TiO_6$] octahedra are connected to the Ru substrate via oxygen atoms shared by two Ti atoms and one Ru atom. The agreement of the calculated infrared reflection absorption (IRA) spectra with the experimental ones provides compelling evidence for the proposed structural model and the segregation into pure silica and a 1:1 (Si:Ti) phase. For low Ti contents, segregation is predicted and observed. Next to pristine silica bilayer domains, domains of the proposed Ti-silicate structure are formed. Those results clearly differ from what was found for Al-substitution into pure silica film but are similar to what was recently found for a Fe-containing silicate film.

## 4.2 Ultrathin Al-Silicate Film on a Ru(0001) Surface

Thin, Al-substituted silica films are of high interest as possible model systems for zeolites. DFT calculations give insight into possible structures of ultrathin aluminosilicate films on a Ru(0001) surface. The computational findings are compared to the characterization of experimentally prepared films. The results obtained by DFT suggest that structures that violate Löwenstein's rule are energetically favorable. Löwenstein's rule [13] states that Al atoms do not occupy neighboring sites in zeolites. DFT and experiment agree that Al occupies positions in the bottom layer first. Computed vibrational modes both for structures that violate Löwenstein's rule and for some that follow this rule, agree reasonably well with experimental IRAS data. These findings weakly support the interpretation of the experimental data on the aluminosilicate films, regarding them as model systems for zeolites.

### 4.2.1 Computational Details

All calculations were based on density functional theory with periodic boundary conditions and carried out using the Vienna ab initio simulation package (VASP) [80, 81], along with the projector augmented wave (PAW) method [57, 82]. We apply the PBE functional [60, 76] augmented with a semi-empirical $^1/_{r^6}$ dispersion term (PBE+D) [27, 66]. A 400 eV cutoff for the plane wave basis set and a $8 \times 4 \times 1$ Monkhorst-Pack grid [55] for the integrations of the first Brillouin zone were used. The surface slabs were modeled using the cell parameters of the silica double layer on Ru(0001) [83, 84]. The cell contains five Ru layers, with the three top layers allowed to relax and two bottom layers fixed to their bulk positions. The positions of the nuclei were relaxed until the forces were smaller than 0.005 eV $\text{Å}^{-1}$. A central finite difference method with 2.0 pm displacements in each Cartesian direction was used to obtain the frequencies. The intensities were obtained from the derivatives of the dipole moment component perpendicular to the surface. To compensate for systematic errors of DFT, the vibrational frequencies are scaled by a factor of 1.0341, derived from a comparison between experimental and calculated frequencies

for $\alpha$-quartz [83].

### 4.2.2 Exploration of Possible Structures

The modeling of the Ti-silicate film followed a methodology similar to the approach recently reported for the investigation of Fe-silicate films [43], which is essentially the same as described for the exploration of possible structures for Ti-silicate Films reported in subsection 4.1.2 of this work. The bilayer silica film [83, 84] with a $Si_8O_{16}{\cdot}n$O/Ru composition (with $n \in \{0, 2, 4\}$), corresponding to 0%, 25% and 50% oxygen coverage of the Ru surface) in the $(2 \times 2)$ unit cell was used as a starting point for the DFT modeling of the substituted films. To investigate possible substitution patterns systematically, one to four Si atoms of the bilayer unit cell were replaced by Al atoms. For each value of $n$, that is, for 0%, 25% and 50% oxygen coverage of the Ru surface, this was done in four steps. In the first step, different possible structures for $AlSi_7O_{16}{\cdot}n$O/Ru that were formed by substituting Al for one of the eight Si atoms in the unit cell were optimized and examined. The most energetically favored of these structures was taken as a starting point to investigate possible substitution locations for the next Al atom to create $Al_2Si_6O_{16}{\cdot}n$O/Ru and so on. By iterative replacement of more Si atoms, other $Al_mSi_{8\text{-}m}O_{16}{\cdot}n$O/Ru structures were created and then optimized.[1]. All assumptions that are made in section 4.1.2 were made here, as well. The cell constants are not changed from those of the pristine silica layer and the orientation of the layer with respect to the metal substrate is unchanged, as well. It is also assumed that the aluminum atoms simply take the positions in the film that have previously been occupied by silicon atoms, so no major changes to the framework are expected. Most importantly, coordination numbers do not change. This assumption should be justified, since this behavior is similar to what one knows from zeolites, were both Al and Si exclusively occupy the so-called tetrahedral ("T") sites and can be exchanged via de-/realumination and de-/resilication. Figure 4.6 shows the resulting structures for the

[1] Preliminary calculations were initially carried out by R. Włodarczyk. For this work, the results of these calculations have been evaluated. Following up on this, some of the calculations have then been repeated and were refined and additional structures have been considered. Those additional results are reported in subsection 4.2.4.

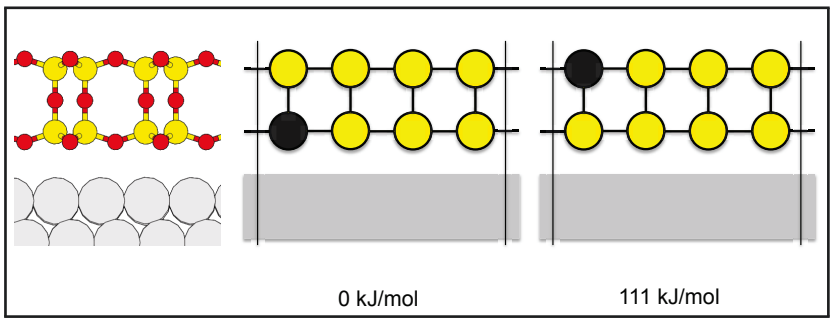


***Figure 4.6:*** *Schematic visualizations and relative energies of the most stable $AlSi_7O_{16}$/Ru structures found by DFT at various Al/Si ratios by substituting Al for Si atoms in the unit cell of the pristine silica double layer (left). In the schematic views (right), only the positions of the Si (yellow) and Al (dark grey) are shown explicitly.*

$AlSi_7O_{16}$/Ru composition. If no surface oxygen is present, only two significantly different structures have to be compared. The two structures differ in whether the Al atom is substituted for a Si atom in the top or in the bottom layer of the silica double layer. Many other structures were investigated as starting points for DFT structure optimizations, but no significantly different structures (concerning the relative position of the double layer with respect to the metal substrate) emerged. All of them converged in one of the two structures that are shown in Figure 4.6. The film can easily move with respect to the surface since it is only bound to it via week Van der Waals forces. Figure 4.6 also introduces a schematic view of the $Al_mSi_{8-m}O_{16}\cdot nO$/Ru unit cell that will be used further in this work.

If surface oxygen is included, other resulting $AlSi_7O_{16}\cdot nO$/Ru structures can be distinguished that differ in their relative positioning of the Al-silicate film with respect to the Ru(0001) surface. These structures are schematically compared in Figure 4.7

For unit cells of the $Al_2Si_6O_{16}\cdot nO$/Ru system, even more complex substitution patterns can be distinguished. They are shown in Figure 4.8 (without surface oxygen), Figure 4.9 (with 25% surface oxygen coverage) and Figure 4.10 (with 25% surface oxygen coverage).

The study of the different Al/Si substitution patterns leads to some general findings. Firstly, it can be observed that Al favors a position in the bottom layer by ca. 100 kJ mol$^{-1}$. Secondly, the substitution pattern and relative positioning with respect to surface oxygen is important. It also can make a difference of ca. 100 kJ mol$^{-1}$. Thirdly, placing Al atoms

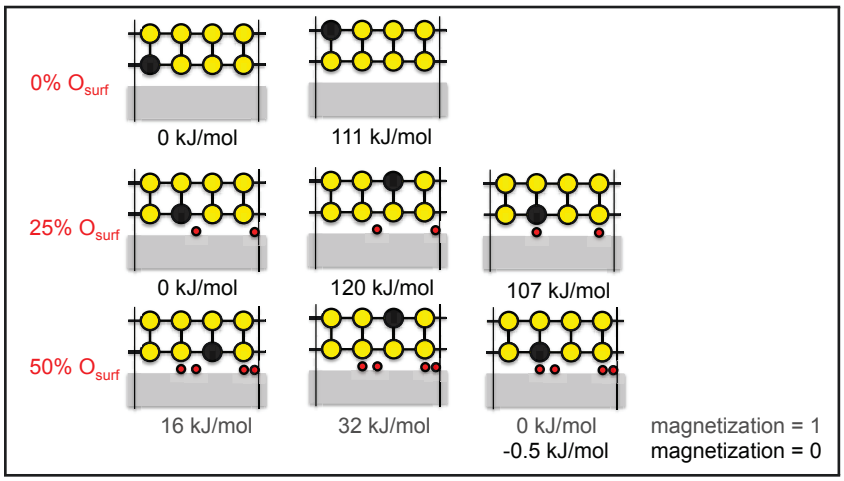


***Figure 4.7:*** *Schematic visualizations and relative energies of the most stable $AlSi_7O_{16}{\cdot}nO/Ru$ structures found by DFT with varying amounts of surface oxygen. Only the positions of the Si (yellow), Al (dark gray) and surface oxygen atoms (red) are shown explicitly.*

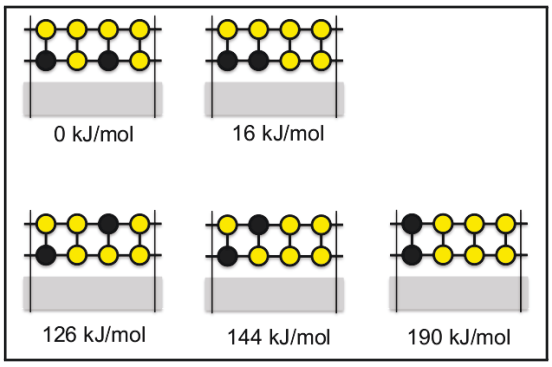


***Figure 4.8:*** *Schematic visualizations and relative energies of the most stable $Al_2Si_6O_{16}/Ru$ structures found by DFT. Only the positions of the Si (yellow) and Al (dark grey) are shown explicitly.*

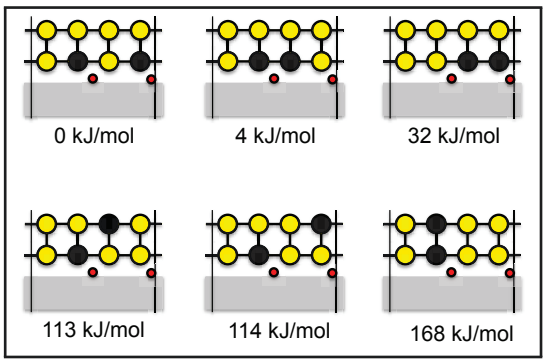


***Figure 4.9:*** *Schematic visualizations and relative energies of the most stable $Al_2Si_6O_{16} \cdot 2\,O/Ru$ structures found by DFT. Only the positions of the Si (yellow), Al (dark grey) and surface oxygen atoms (red) are shown explicitly.*

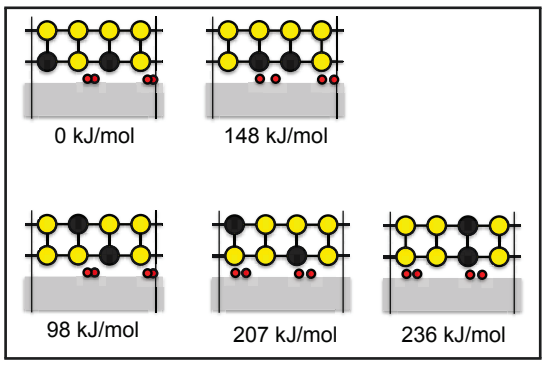


***Figure 4.10:*** *Schematic visualizations and relative energies of the most stable $Al_2Si_6O_{16} \cdot 4\,O/Ru$ structures found by DFT. Only the positions of the Si (yellow), Al (dark gray) and surface oxygen atoms (red) are shown explicitly.*

in neighboring positions is disfavored by up to ca. $45\,\mathrm{kJ\,mol^{-1}}$ (if one aluminum atom is placed in the top layer, on top of the other aluminum atom). When both Al atoms are placed in the bottom layer, the energy cost of placing them in neighboring positions is much smaller: $16\,\mathrm{kJ\,mol^{-1}}$, if no surface oxygen is included; only $4\,\mathrm{kJ\,mol^{-1}}$, if the oxygen coverage of the surface is at 25% and $148\,\mathrm{kJ\,mol^{-1}}$, if the oxygen coverage of the surface is at 50%. This last case can be connected with the second observation from above. Note, one aluminum atom is placed directly above a surface oxygen atom which is energetically very disadvantageous. These findings have to be discussed in greater detail in comparison with experimental results later. The computational data are not as conclusive one might expect, especially with regard to Löwenstein's rule [13]. One has to keep in mind that the aluminosilicate film has no bridging hydroxyl groups and there are no counter ions. One should assume that electrons are transferred from the ruthenium substrate to the film and this need to be investigated in more detail later. Figure 4.11 shows the resulting, most stable structures for 12.5 %, 25 %, 37.5 % and 50 % substitution of the Si atoms by Al. One can see clearly that for all aluminum contents that were considered, only positions in the bottom layer are preferably occupied by Al, leading up to the completely filled layer. In all cases, the principle structural features were not changed. Both Ti and Al are always tetrahedrally coordinated. This is quite different from what was observed in the case of the Ti-silicate film of the previous chapter of this thesis. Here, even when the bottom layer is completely filled with Al, the structure stays intact. What will happen

at low Al contents? Should one expect lateral segregation into Al-rich domains and domains of the pristine silica bilayer? Equations 4.5 to 4.7 show the corresponding reactions and their reaction energies which are estimated from total slab energies.

$$2\,AlSi_7O_{16}\cdot n\mathrm{O/Ru} \longrightarrow Al_2Si_6O_{16}\cdot n\mathrm{O/Ru} + Si_8O_{16}\cdot n\mathrm{O/Ru},$$
$$\Delta E = \begin{cases} 47\,\mathrm{kJ\,mol^{-1}} & \text{for } n = 0 \\ 13\,\mathrm{kJ\,mol^{-1}} & \text{for } n = 2 \end{cases} \tag{4.5}$$

$$3\,AlSi_7O_{16}\cdot n\mathrm{O/Ru} \longrightarrow Al_3Si_5O_{16}\cdot n\mathrm{O/Ru} + Si_8O_{16}\cdot n\mathrm{O/Ru},$$
$$\Delta E = \begin{cases} 216\,\mathrm{kJ\,mol^{-1}} & \text{for } n = 0 \\ 88\,\mathrm{kJ\,mol^{-1}} & \text{for } n = 2 \end{cases} \tag{4.6}$$

$$4\,AlSi_7O_{16}\cdot n\mathrm{O/Ru} \longrightarrow Al_4Si_4O_{16}\cdot n\mathrm{O/Ru} + Si_8O_{16}\cdot n\mathrm{O/Ru},$$
$$\Delta E = \begin{cases} 421\,\mathrm{kJ\,mol^{-1}} & \text{for } n = 0 \\ 195\,\mathrm{kJ\,mol^{-1}} & \text{for } n = 2 \end{cases} \tag{4.7}$$

However, according to the estimated reaction energies for the segregation reactions in equations 4.5 to 4.7 , no such phenomenon should be expected. An even distribution of aluminum seems to be preferred since all segregation reactions come with energy costs instead the energy gains that could be observed in other cases (see p. 40).

### 4.2.3 Comparison to Experimental Observations

Experiments were performed in an ultrahigh vacuum system equipped with XPS, LEED, IRAS, and STM. The Ru(0001) surface was cleaned with cycles of $Ar^+$ sputtering and annealing at 1400 K. The clean surface was pre-covered with a 3O($2 \times 2$)-layer overlayer by exposing to $3 \times 10^{-6}$ mbar $O_2$ at 1200 K. The films were prepared by sequential Si and Al physical vapor deposition in $2 \times 10^{-7}$ mbar $O_2$. The surface was then oxidized in $3 \times 10^{-6}$ mbar $O_2$ at 1200 K for 10 min and slowly cooled down to 450 K in an $O_2$ en-

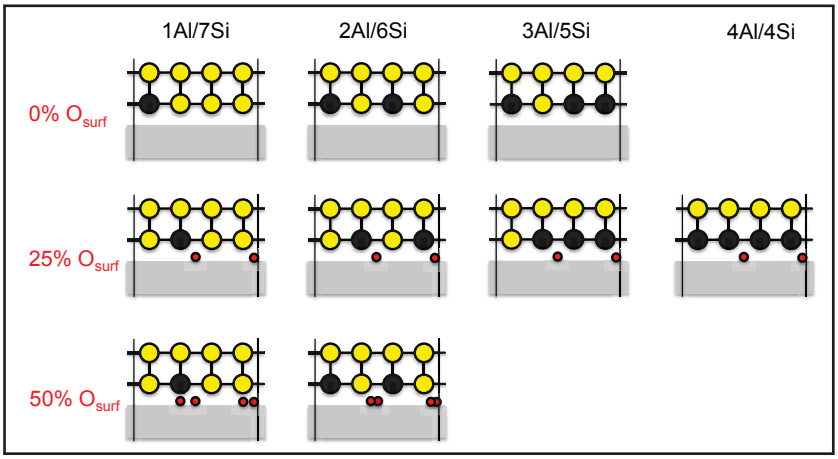


***Figure 4.11:*** *Schematic visualizations of the most stable $Al_mSi_{8-m}O_{16}{\cdot}nO/Ru$ structures found by DFT at various Al/Si ratios and with varying amounts of surface oxygen. Only the positions of the Si (yellow), Al (dark grey) and surface oxygen atoms (red) are shown explicitly.*

vironment.[1] The experiments show several key observations. Firstly, in IRAS experiments, bridging hydroxyl groups Si-O(H)-Al are only visible at Al:Si ratios above 25%. The nature of the bridging hydroxyl groups will be considered later. Here, it supports an assumption based on Löwenstein's rule [13] that was made about the structure. Following this rule, it has to be assumed that as aluminum atoms do not occupy neighboring tetrahedral sites in zeolite frameworks, they also should not be next neighbors in this aluminosilicate film. Thus, the observation about the hydroxyl groups suggests that Al atoms preferably occupy positions in the bottom layer, where possible bridging hydroxyl groups would be invisible since they could form hydrogen bonds with surface oxygen and the resulting broadening of the signals would make them very difficult to detect. Once the bottom layer is half-filled, Al begins to occupy positions in the top layer and the IRAS signal for the bridging hydroxyl groups can be observed. This interpretation of the spectroscopic observations, in accordance with Löwenstein's rule in general, are however in direct contrast with the computational results presented above. This discrepancy needs to be resolved. The DFT data suggest the violation of Löwenstein's rule and indicate that the aluminum atoms occupy solely positions in the bottom layer (as long as the Al:Si ratio is below 50%), up to a structure where all tetrahedral sites in the bottom layer are

[1] All Experiments and qualitative interpretation of the data were carried out by the group of H.-J. Freund at the Fritz-Haber-Institut, Berlin. This section of the thesis is based on the joint publication [FDF1].

occupied by aluminum. To investigate this disagreement between the computationally derived structural models and the more natural assumptions on the structure of the aluminosilicate films, based on Löwenstein's rule, harmonic IRA spectra can be calculated and compared to the experiment. Figure 4.12 shows the calculated harmonic IRA spectra for the most stable $Al_mSi_{8-m}O_{16}{\cdot}2O/Ru$ structures and for the pristine silica bilayer containing 0 % Al. Only modes above $600\,cm^{-1}$will be discussed here since only those can be compared to the experimental observations later. As can be seen in the figure, all of the calculated spectra show two vibrations that correspond to a significantly higher IRAS adsorption intensity than all other. The scaled [83] frequencies of these two vibrations are given for all of the selected structures in table 4.3. The experimentally observed IRAS frequencies are listed here, as well. The agreement between the computed and the observed frequencies is rather close for all but the last ($Al_4Si_4$) structure. This shows that at least at those Al contents that were used experimentally, the structure that was found computationally (see Figure 4.11) for the $Al_4Si_4O_{16}{\cdot}2O/Ru$ composition can be excluded - this structure is most probably not present under the experimental conditions. In fact, for films with an Al molar fraction approaching 0.5 (that is, Al/ Si = 1), the integrity of the film is not conserved in the experiment [41]. In contrast to equation 4.5, there is some experimental evidence that supports segregation. Figure 4.13 shows an STM image of the aluminosilicate film at low Al content. In the image, domains can be distinguished. The size of domain type A in Figure 4.13 increases with increasing Al content. Therefore, it is reasonable to assume that this domain contains the aluminosilicate film $Al_xSi_{1-x}O_2$, while domain B consists of the pristine silica film. If the distribution of Al atoms within the islands A, shown in Figure 4.13, follows Löwenstein's rule, then for this film ($x = 0.12$) the islands would cover $0.48 (= 0.12 \times 4)$ of the whole surface, which is in excellent agreement with the 45%coverage observed experimentally. This proposed segregation would violate Dempsey's statement [89] based on electrostatic considerations that Al atoms arrange in zeolitic structures as far as possible from each other. This statements obviously does not include possible influence of the metal substrate on the Al-silicate bilayer.

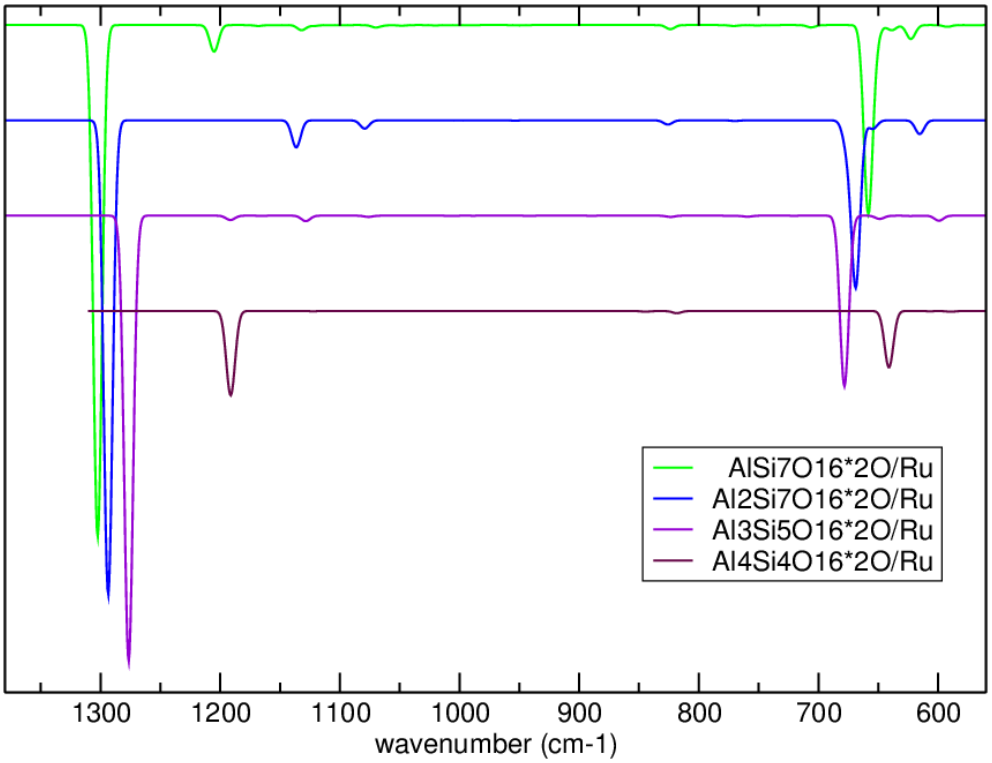


***Figure 4.12:*** *IRA spectra simulated for the most stable $Al_mSi_{8-m}O_{16}{\cdot}2O/Ru$ with $m \in \{1,2,3,4\}$. The spectra are scaled by a factor of 1.0341 [83].*

***Table 4.3:*** *Scaled [83] PBE+D frequencies (in $cm^{-1}$) for the two most IR-active (highest intensity) vibrational modes of Ru-supported aluminosilicate films $Al_mSi_{8-m}O_{16}{\cdot}2O/Ru$ with $m \in \{1,2,3,4\}$. An overlayer of surface oxygen (25%) was included in the calculations. The results are compared to the experimentally observed [41] IRAS frequencies. The structural details of the systems of interest were explained in Figure 4.11 and on page 49.*

| System | Vib. 1 | Vib. 2 |
|---|---|---|
| $AlSi_7O_{16}{\cdot}2O/Ru$ | 1302 | 658 |
| $Al_2Si_6O_{16}{\cdot}2O/Ru$ | 1294 | 669 |
| $Al_3Si_5O_{16}{\cdot}2O/Ru$ | 1277 | 678 |
| $Al_4Si_4O_{16}{\cdot}2O/Ru$ | 1191 | 641 |
| *exp. observed* | *1300-1270* | *690-702* |

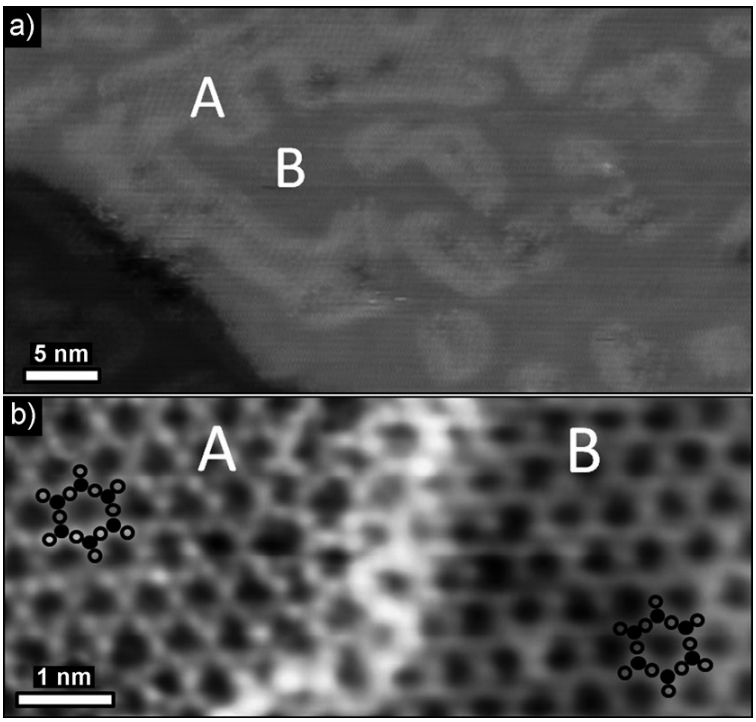


***Figure 4.13:*** *a) Large-scale STM image of an $Al_{0.12}Si_{0.88}O_2$ film. b) High-resolution STM image showing different contrast inside the islands A. The positions of the Si atoms in the top layer are shown by black circles and O atoms by open circles. Tunneling parameters: bias* 0.15 V*, current* 0.07 nA*. The figure is taken from [FDF1].*

### 4.2.4 Re-Evaluation of Possible Structures

The computationally derived structural models for the aluminosilicate films do not agree with Löwenstein's rule. To get further understanding of this system, an additional model system is now introduced that is inspired by Löwenstein's rule and accordingly, "chemical intuition" as well as by the experimental observations concerning bridging hydroxyl groups that has been mentioned above. In the experiments, a film of $Al_{0.36}Si_{0.64}O_2$ compositions has been investigated. This corresponds to a $Al_3Si_5O_{16}\cdot 2O/Ru$ unit cell if we make the usual assumptions about surface oxygen. A structural model that confirms with the chemist's expectations is shown in Figure 4.14 where it is contrasted with the most stable structure for this composition that has been found by the systematic approach that was described before.

Calculations of the total slab energy[1] show that it is energetically disfavored by

[1]The computational setup for the calculations in this subsection was slightly changed from the previous calculations. It was found that a $4 \times 2 \times 1$ Monkhorst-Pack grid [55] for the integrations of the first Brillouin zone was sufficient.

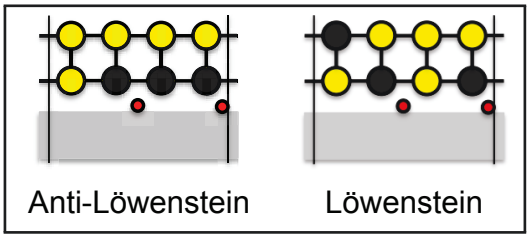


***Figure 4.14:*** *Two structural models for a $Al_3Si_5O_{16}{\cdot}2O/Ru$ unit cell. One right one is allowed by Löwenstein's rule.*

***Table 4.4:*** *Relative energies $\Delta E$ in* kJ mol$^{-1}$ *per unit cell and scaled [83] PBE+D frequencies (in* cm$^{-1}$*) for the two most IR-active (highest intensity) vibrational modes of Ru-supported aluminosilicate films $H_nAl_3Si_5O_{16}{\cdot}2O/Ru$ with $n \in \{0,1\}$. An overlayer of surface oxygen (25%) was included in the calculations. The results are compared to the experimentally observed [41] IRAS frequencies.*

| | $\Delta E$ | | Vib. 1 | | Vib. 2 | |
|---|---|---|---|---|---|---|
| $n$(H) | 0 | 1 | 0 | 1 | 0 | 1 |
| anti-Löwenstein structure v1 | 0 | 51.3 | 1277 | 1273 | 680 | 673 |
| anti-Löwenstein structure v2 | | 69.5 | | 1277 | | 666 |
| Löwenstein structure | 87.1 | 0 | - | 1284 | - | 676 |
| *exp. observed $Al_{0.36}Si_{0.64}O_2$* | | | *1281* | | *692* | |

87 kJ mol$^{-1}$ per unit cell. This could be a discouraging finding. If the locations of the Al atoms in the films (domains) truly do not follow Löwenstein's rule, the experimentally prepared aluminosilicate film cannot be established as a two-dimensional zeolite so clearly. A further investigation of the DFT results shows that the total charge that is transferred from the Ru substrate to the aluminosilicate film is only about 1.3 to 1.6 $e$ while the unit cell contains 3 Al atoms. Is this charge compensation enough for a realistic situation? Or is there a computational artifact? Does the selected DFT method not describe the electronic system accurately enough? The accurate description of a system that contains both a metal (highly delocalized electrons) and silicate system with comparably covalent bonds and localized electrons is challenging for any functional. To test this, additional calculations have been performed where a hydrogen atom was added. This is favorable compared to directly adding an electron, since charged systems are problematic when being treated with periodic boundary conditions. The results are a surprise. The energetic ordering of the two models of Figure 4.14 is now inverted! Now, the model system that agrees with chemical intuition is the most stable structure. A calculation of harmonic

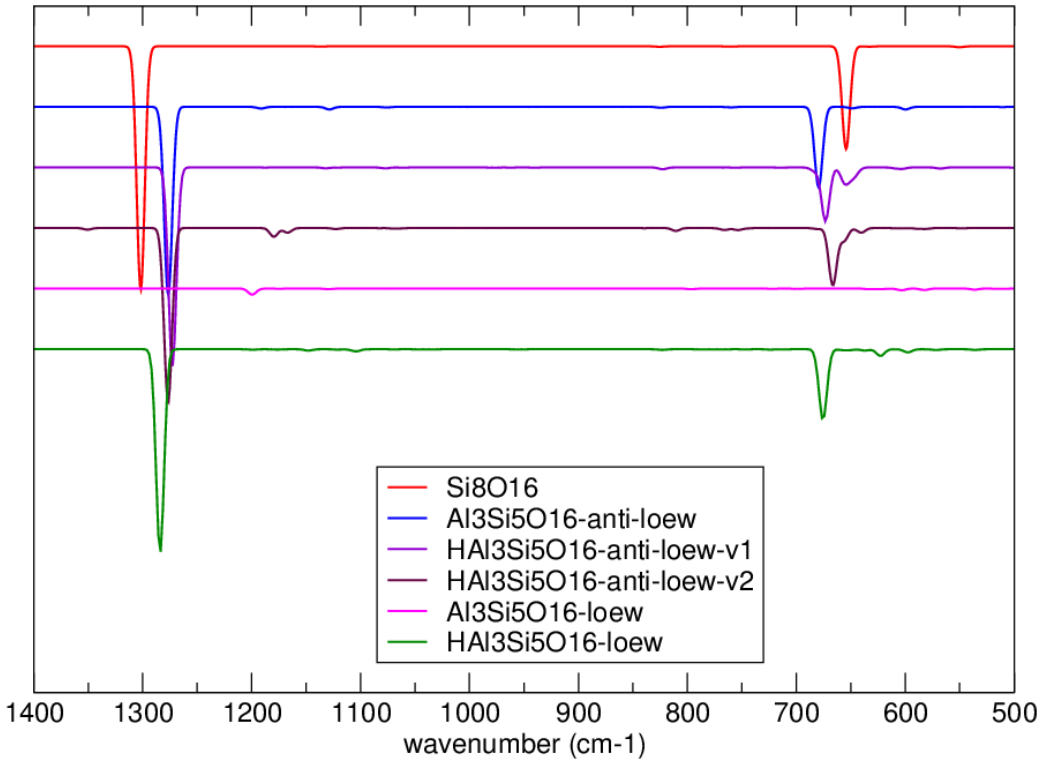


***Figure 4.15:*** *IRA spectra simulated for the most stable the pristine silica film and different models for the aluminosilicate film with the Al:Si ratio of 3:5. Thes models include both the "Löwenstein-like structure" and the "anti-Löwenstein-like" one that was obtained by the systematic structure exploration that was explained in subsection 4.2.2. Spectra are simulated both for the pure aluminosilicate films $Al_3Si_5O_{16}$·2O/Ru and for structures where one hydrogen atom was added to obtain a bridging Si-O(H)-Al group. The spectra are scaled by a factor of 1.0341 [83].*

vibrational frequencies is necessary to further confirm this model. The results are summarized in table 4.4. Most surprisingly, the calculations predict no vibrational modes of significant IR intensity, if no hydrogen atom is added. After the addition of the hydrogen atom, the vibrations appear exactly at the region where one would expect them and they are in fact even closer to the experimentally observed ones than the vib. frequencies that have been calculated for the previous $Al_3Si_5O_{16}$·2O/Ru structure (see Figure 4.11 at 3Al/5Si and 25% $O_{surf}$). Figure 4.15 shows computed IRA spectra for the pristine silica layer, both different model systems of $Al_3Si_5O_{16}$·2O/Ru composition with and without the added hydrogen atom.

### 4.2.5 Conclusions

DFT calculations give insight into possible structures of ultrathin aluminosilicate films, prepared on a Ru(0001) surface. The computational findings are compared to the characterization of experimentally prepared films. Contrary to chemical intuition and some experimental findings, the results obtained by DFT suggest that structures that violate Löwenstein's rule are energetically favorable. DFT and experiment agree that Al preferentially occupies positions in the bottom layer. Computed vibrational modes agree reasonably well with experimental IRAS data for both structures that follow Löwenstein's rule and for some that do not. These theoretical results weakly support the interpretation of the experimental findings on the aluminosilicate films, regarding them as model systems for zeolites.

## 4.3 Acidity of the H-2dH Zeolite: Influence of Al Content and Metal Support

Two-dimensional zeolite films are an interesting model system to investigate the limiting case of a zeolite with infinite pore size. A simple model for DFT calculations using periodic boundary conditions consists of a free-standing zeolite film with one Aluminum atom per unit cell, as well as one bridging hydroxyl group Si-OH-Al. Here, DFT calculations of the adsorption energies and the OH frequency shift upon CO adsorption are approximations to a more realistic modeling of the experimentally prepared H-2dH zeolite, including both metal support and a higher Aluminum content in the film. Increasing the Al:Si ratio reduced the acidity, while adding a Ru(0001) support to a free-standing bilayer increased the acidity. Adding both effects leads to a cancellation of errors. Simplifying the modeling of the experimental system by including only one Al atom in the unit cell and neglecting the metal support in the calculations can therefore still give a rather good agreement when comparing the DFT results to the experimental observations. This is important, since it is computationally much less demanding to investigate the simplified model.

### 4.3.1 Computational Details

All calculations were based on density functional theory with periodic boundary conditions and carried out using the Vienna ab initio simulation package (VASP) [80, 81], along with the projector augmented wave (PAW) method [57, 82]. We apply the PBE functional [60, 76] augmented with a semi-empirical $^1/_{r^6}$ dispersion term (PBE+D) [27, 66]. A 400 eV cutoff for the plane wave basis set and an $4 \times 2 \times 1$ Monkhorst-Pack grid [55] for the integrations of the first Brillouin zone were used. The surface slabs were modelled using the cell parameters of the silica double layer on Ru(0001), including two adsorbed oxygen atoms per unit cell that are adsorbed on the Ru surface [83, 84]. As was done in previous investigations, the cell was then doubled along its shortest axis, resulting in

a 1079.2 × 934.6 × 2700.0 pm cell, containing five Ru layers, with the three top layers allowed to relax and two bottom layers fixed to their bulk positions. This cell that now includes 16 T-atoms has two possible adsorption sites Si-OH-Al, only one of which was occupied for the calculations in order to reduce lateral interaction. The positions of the nuclei were relaxed until the forces were smaller than 0.005 eV Å$^{-1}$. For the calculation of the vibrational frequencies for the O-H and C-O stretching modes, the $\omega/r$ correlation and anharmonicity correction proposed by Nachtigall [79] was used.

### 4.3.2 Results and Discussion

The two-dimensional zeolite H-2dH is constructed experimentally as an Al-substituted silica bilayer that is supported on a Ru(0001) surface which is already covered with some surface oxygen. It exhibits bridging hydroxyl-groups Si-OH-Al. Previously, it has been investigated computationally using a simplified model where the Ru support was completely neglected and only one Si atom per unit cell (which contains 8 T-atoms) was substituted by Al, resulting in an $^{Al}/_{Al+Si}$ ratio of 0.175. Note, experimentally, only systems with this ratio being higher than 0.25 exhibit bridging hydroxyl groups [41, 42]. This work investigates the effects of a more realistic modeling of the H-2dH system and the Brønsted acidity by comparing the calculated adsorption behavior of carbon monoxide and ammonia for different models.

Three different model systems have been investigated and are compared in the following. They are schematically explained in Fig. 4.16. The simplest model is the one that has been used previously [41, 42]. The metal support is neglected and, after doubling along one axis, the composition of the unit cell is $\{HAlSi_7O_{16}\}_2$. Including the metal support without changing the composition of the aluminosilicate film resulted in the second model. For the third model, half of the T-sites in the bottom layer of the film are occupied with Al but no bridging hydroxyl groups Si- O(H)-Al are formed in the bottom layer. One fourth of the T-sites in the top layer is occupied by Al as well and here, bridging hydroxyl groups are included. The Al/(Al+Si) ratio of 0.375 is closer to what is used experimen-

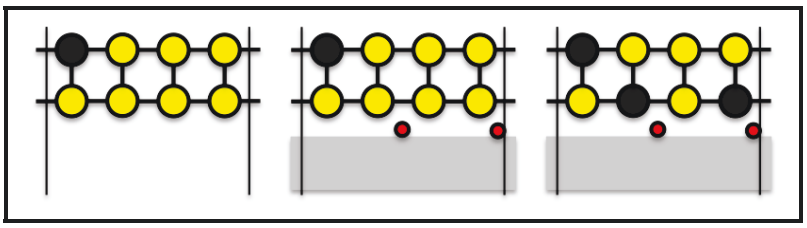

***Figure 4.16:*** *The three different models that have been used to model the H-2dH zeolite film. Only the positions of the Si, Al and surface oxygen atoms are shown explicitly.*

***Table 4.5:*** *PBE+D adsorption energies (in* $\mathrm{kJ\,mol^{-1}}$*) of CO and* $NH_3$ *on three different models for the H-2dH film. For CO adsorption, the shifts in the vibrational wavenumbers (in* $\mathrm{cm^{-1}}$*) of the O-H and C-O stretching modes are reported and compared with the experimentally observed values.*

| System | $NH_3$ | CO | | |
|---|---|---|---|---|
| | $\Delta_{\mathrm{ads.}}E$ | $\Delta_{\mathrm{ads.}}E$ | $\Delta_{\mathrm{ads.}}\nu_{\mathrm{O\text{-}H}}$ | $\Delta_{\mathrm{ads.}}\nu_{\mathrm{C\text{-}O}}$ |
| $HAlSi_7O_{16}$ | -155.8 | -38.9 | -386.6 | 41.2 |
| $HAlSi_7O_{16}\cdot 2\,O/Ru$ | -168.8 | -40.6 | -387.1 | 45.5 |
| $HAl_3Si_5O_{16}\cdot 2\,O/Ru$ | -161.2 | -39.1 | -363.4 | 39.5 |
| exp. observed [42] | | | -379 | 40 |

tally [41]. This model is expected to be the closest to the "real", experimental system. Table 4.5 compares the adsorption energies of both $NH_3$ and CO for the three model systems. In addition, the shifts in the vibrational frequencies of the O-H stretching mode and the C-O stretching mode upon adsorption of a single CO molecule are reported.

Table 4.5 shows the same trend for all calculated properties: Going from the first $HAlSi_7O_{16}$ to the second ($HAl_3Si_5O_{16}\cdot$) model system, the adsorption energies increase in absolute value for both ammonia and carbon monoxide. The red-shifting of the vibrational frequency of the O-H stretching mode is more pronounced and the blue-shift of the C-O stretching mode has also increased. The third model system ($Al_3Si_5O_{16}\cdot 2O/Ru$), which includes both the metal support and higher aluminum content, reveals the opposite effect. The absolute values of the adsorption energies are lower and the shift in the vibrational frequencies is also decreased compared to the second model system. In fact, this third model exhibits a lower acidity (as measured by the shift in O-H bond stretching frequency, see p. 12) than the first. The effects of including the metal support and modeling the experimental film with a more realistic, higher Al content act in opposite directions. This is a fortuitous phenomenon since it explains that a cancellation of errors

is the reason for the previously (preliminary) identified first model system reproducing the experimental data sufficiently well.

### 4.3.3 Conclusions

The interaction of CO molecules with bridging hydroxyls of two-dimensional aluminosilicate films was studied using periodic DFT. Three different model systems were compared, namely a free-standing model system with one Al atom per unit cell and one acidic hydroxyl group, the same film, but now supported on a Ru(0001) surface with pre-adsorbed oxygen, and finally, the Ru-supported film with the Al/Si ratio raised to 3/5 while still including only one bridging hydroxyl group. In the last case, the film has an overall negative charge, with some electrons transferred from the metal. This system comes closest to what probably exists under experimental conditions. It was investigated how much the inclusions of these aspects in the structural model effect the calculated adsorption energies and OH frequency shifts on CO adsorption, which is an indicator of acidity. Increasing the Al/Si ratio reduced the adsorption energies and the OH frequency shifts, while adding a Ru-substrate to the model had the opposite effect. Adding both effects leads to at least some cancellation of errors. Using the simplified model system that disregards the role of the metal support and has an unrealistically low Al/Si ratio can therefore still give a rather good agreement with the experiment.

## 4.4 Adsorption of Probe Molecules on Zeolites and a Two-Dimensional Zeolite Model System

The presence of acidic hydroxyl groups Si-OH-Al within the pores of zeolites plays a crucial role in their catalytic activity. One of the ways to characterize bridging hydroxyls is by adsorption of probe molecules. An aluminosilicate bilayer containing such hydroxyl groups is used as a model of the internal surface of zeolites representing infinitely large pores. This model consists of a planar sheet of hexagonal prisms and is therefore called H-2dH in its protonated form. DFT calculations give insight into the behavior of a free-standing model of this zeolitic film. The results are compared to adsorption experiments carried out on the experimentally prepared hydroxylated aluminosilicate film supported on a Ru(0001) surface. The comparison (both theory and experiment) with the properties of three-dimensional zeolites shows that this two-dimensional zeolite model system exhibits bridging hydroxyls with properties similar to those of the most catalytically active zeolites. It can be used further to achieve a deeper understanding of structure-reactivity relations in zeolites. [1]

### 4.4.1 Computational Details

All calculations were based on density functional theory with periodic boundary conditions and carried out using the Vienna ab initio simulation package (VASP) [80, 81], along with the projector augmented wave (PAW) method [57, 82]. We apply the PBE functional [60, 76] augmented with a semi-empirical $^1/_{r^6}$ dispersion term (PBE+D) [27, 66]. The calculations were carried out at the Γ-point, using a 600 eV cutoff for the plane wave basis set. If not explicitly stated otherwise, the following cell parameters were used: For the calculations on the bilayer, the $HAlSi_7O_{16}$ unit cell ($539.61 \times 934.64 \times 2700.0$ pm, $\alpha = \beta = \gamma = 90°$) that was taken from the silica double layer on Ru(0001) [83, 84] was doubled along its shortest axis, resulting in a $1079.2 \times 934.64 \times 2700.0$ pm cell. One and two molecules were adsorbed per double cell. For chabazite, the cell parameters were op-

[1] The results presented here are based on excerpts from the joint publication [FDF2].

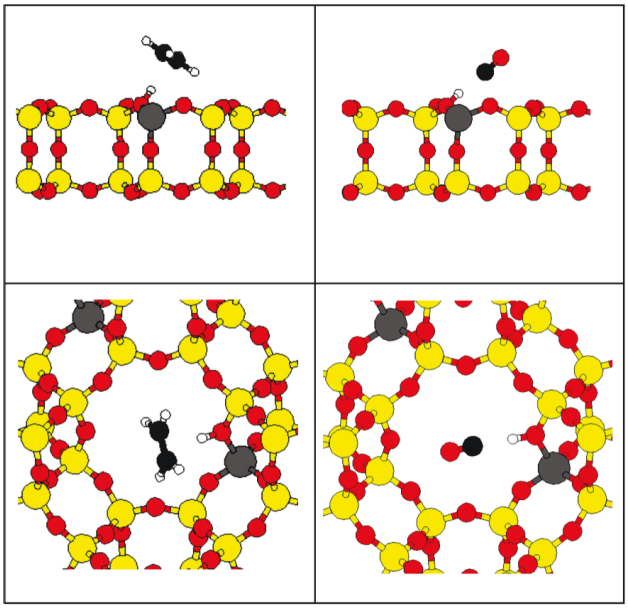

***Figure 4.17:*** *Adsorption structures of $C_2H_4$ (left) and CO (right) in H-2dH (top) and H-CHA (bottom). The figure is taken from [FDF2].*

timized for a $(HAlSi_{11}O_{24})_2$ double cell (942.63 × 937.16 × 1870.80 pm, $\alpha = 93.530°, \beta = 94.120°, \gamma = 94.491°$). Molecules in the gas phase were calculated using a box with the same cell parameters as in the adsorbed state. The positions of the nuclei were relaxed until the forces were smaller than 0.005 eV Å$^{-1}$. For the calculation of the harmonic force constants, a central finite difference method with 1.5 pm displacements in each Cartesian direction was used to obtain the frequencies. The intensities were obtained from the derivatives of the dipole moment component perpendicular to the surface. For the calculation of the vibrational frequencies for the OH and CO stretching modes, the $^{\omega}/_{r}$ correlation and anharmonicity correction proposed by Nachtigall [79] was used. The vibrational wavenumbers reported along the text correspond to the case of one molecule adsorbed per double cell.

### 4.4.2 DFT Adsorption Energies

Figure 4.17 and Figure 4.18 show the optimized adsorption structures for the adsorbed molecules. Table 4.6 shows the adsorption energies, which are according to

$$\Delta E_{\text{ads}} = E(\text{M/H-Z}) - \{E(\text{H-Z}) + E(\text{M})\}, \tag{4.8}$$

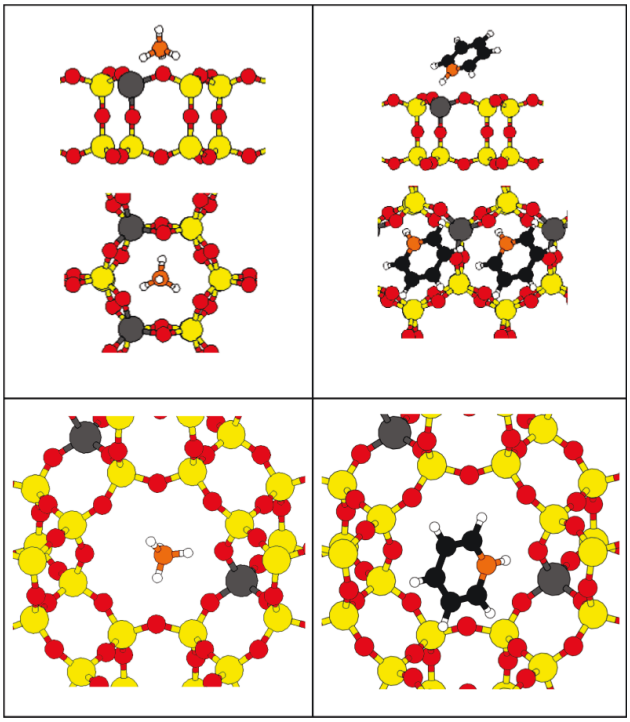

***Figure 4.18:*** *Adsorption structures of $C_2H_4$ (left) and CO (right) in H- 2dH (top) and H-CHA (bottom). The figure is taken from [FDF2].*

where $E(\text{H-Z})$ is the energy of the zeolite, $E(\text{M})$ the energy of the isolated molecule and $E(\text{M/H-Z})$ the energy of the system where the molecule is adsorbed on the zeolite. Experimental results are hardly available. For the adsorption of $C_2H_4$, Hansen et al. [26] quote a value of $-40.5\,\text{kJ mol}^{-1}$ which they derived from experimental heat of adsorption on a (H,Na)-zeolite Y[90] and vibrational corrections as well as thermal corrections form DFT+D calculations. They performed hybrid MP2:PBE+D + $\Delta$CCSD(T) calculations for $C_2H_4/\text{H}-\text{MFI}$ and obtained an adsorption energy of $-48.3\,\text{kJ mol}^{-1}$ [26]. It is illustrative to compare the calculated adsorption energies for different systems, since these relative energies are more reliable than the absolute PBE+D adsorption energies. For CO and $C_2H_4$, the calculated adsorption energies are $-2.6$ and $-4.9\,\text{kJ mol}^{-1}$, respectively. They are smaller on the flat surfaces of the film than in the cavities of chabazite (see Table 4.6). This illustrates the effect of missing pore fit which has been observed before (see Lucas et al. [45] and references therein), when comparing adsorption in small (better fit) and large pores (less good fit). The increase from the flat surface to the cavity is even more pronounced when looking at the dispersion contribution only: $-4.1$ and $-11.3\,\text{kJ mol}^{-1}$

for CO and $C_2H_4$. That the effect is larger for the dispersion contribution than for the total adsorption energy implies that there must be another component, which is stronger for the 2dH film than for chabazite. This interaction is governed by acidity and we find it to be stronger for the 2dH film than for chabazite.

### 4.4.3 Frequency Shifts, Comparison to Experiment

**Weak Bases: Carbon Monoxide and Ethene** Table 4.7 compares experimental and calculated OH frequency shifts on adsorption of CO and $C_2H_4$ on Brønsted sites of the 2dH film with zeolites H-CHA and H-ZSM-5. The ratio of the experimental shifts of $C_2H_4$ compared to CO adsorption is similar for H-MFI (1.38) and H-2dH (1.28). Comparing the 2dH films with the CHA and MFI zeolites, the experimental shifts are larger for the 2dH films, indicating a higher acidity. The same is seen for the calculated vibrational frequencies. It is important that this trend is reproduced, although for $C_2H_4$ adsorption, the calculated shift numbers are too large. This is a well-known weakness of the exchange-correlation functional applied [20]. The OH bonds are too weak and too long, and on formation of a hydrogen bond they become too much elongated resulting in a too large red-shift. For CO adsorbed on bridging hydroxyls, it is possible to determine the CO and OH stretching frequencies directly from the corresponding DFT bond distances. This method proposed by Nachtigall [79] yields much improved vibrational frequencies as the required parameters have been found by comparison with high-level, i.e., CCSD(T), calculations. For the ethene complexes, where the frequency shifts are much larger, neither is it guaranteed that this correlation would work nor are the required parameters available. Here, unscaled harmonic frequencies are used. Scale factors, which would effectively account for too small harmonic force constants and neglected anharmonicities, are close to 1.0 for the PBE functional anyway (a scale factor of 0.9948 yields a root-mean-square deviation of $38\,\mathrm{cm}^{-1}$, see Merrick et al. [91]). While Table 4.7 reports OH frequency shifts, Figures 4.19 and 4.20 report experiments on OD groups. For CO on bridging OD, the results of the Nachtigall scheme for the OH frequencies have been multiplied with the ratio

***Table 4.6:*** *Calculated PBE+D adsorption energies (in* kJ mol$^{-1}$*, dispersion contribution in parentheses) of CO, $C_2H_4$, $NH_3$ and $NC_5H_5$ on the zeolite H-CHA and on the H-2dH film.*

| system | M:cell[a] | CO | $C_2H_4$ | $NH_3$ | $NC_5H_5$ |
|---|---|---|---|---|---|
| H-CHA | 1:2 | -40.4 (-19.3) | -53.3 (-36.8) | -158.6(-27.4) | -182.2 (-66.4) |
| H-2dH | 1:2 | -37.8 (-15.2) | -48.4 (-25.5) | -160.2 (-28.8) | -145.1 (-47.1) |
| $\Delta\Delta E_{\text{ads}}$ | | +2.6 (+4.1) | +4.9 (+11.3) | +1.6 (+1.4) | +37.1 (+19.3) |
| H-2dH | 2:2 | -37.8 (-15.1) | -49.1 (-27.4) | -155.1 (-29.0) | -132.6 (-54.8) |
| $\Delta E_{\text{lateral}}$[b] | | 0.0 | -0.7 | +5.0 | +12.5 |

[a] Loading, number of molecules per cell

[b] Lateral interaction energy $\Delta E_{lateral} = \Delta E_{ads}(1:2) - \Delta E_{ads}(2:2)$; positive numbers indicate repulsion.

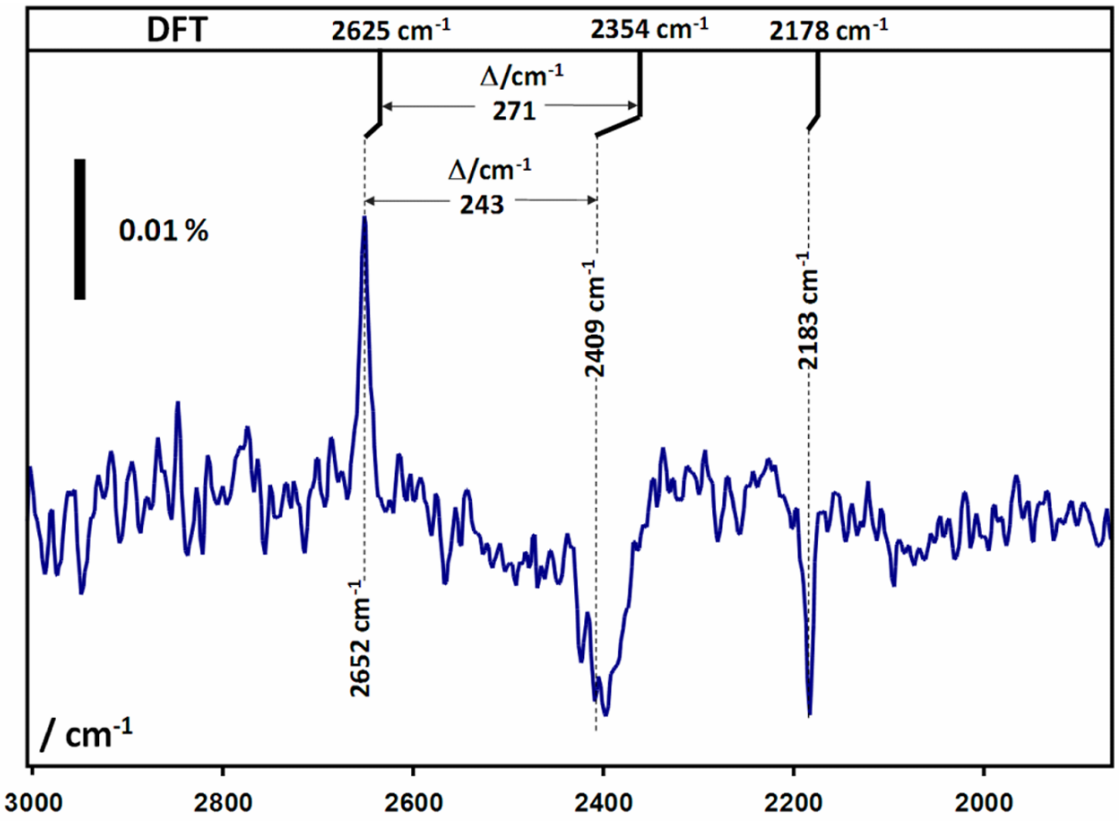


***Figure 4.19:*** *Comparison of the computationally derived vibrational modes with the experimental transmittance spectrum of CO adsorbed on bridging OD groups divided by the spectrum taken before CO adsorption. Spectrum taken under CO pressure ($2 \times 10^{-5}$ mbar). At the top of the spectrum the DFT results are shown (double cell, Nachtigall scheme [79], see Computational Details p. 62). The figure is taken from the publication [FDF2].*

of the reduced masses

$$\nu_{OD} = \nu_{OH} * \sqrt{\frac{9}{17}} \tag{4.9}$$

yielding a red-shift of 271 $cm^{-1}$, from 2625 to 2354 $cm^{-1}$ for the O-D stretching vibration (see top of Figure 4.19). A red-shift of 394 $cm^{-1}$ (see top of Figure 4.20) was calculated for the O-D mode when adsorbing $C_2H_4$ (from 2681 to 2287 $cm^{-1}$). This is again larger than the 325 $cm^{-1}$ shift observed experimentally. Good agreement was found for the symmetric out-of-plane C-H wagging mode, yielding a frequency (988 $cm^{-1}$) close to the experimental value (992 $cm^{-1}$).

**Strong Bases: Pyridine and Ammonia** When strong bases such as pyridine (Py) or ammonia ($NH_3$) interact with the bridging hydroxyls of zeolites, it is a well-established fact that they abstract the proton to form $PyH^+$ and $NH_4^+$ ions, respectively. The inter-

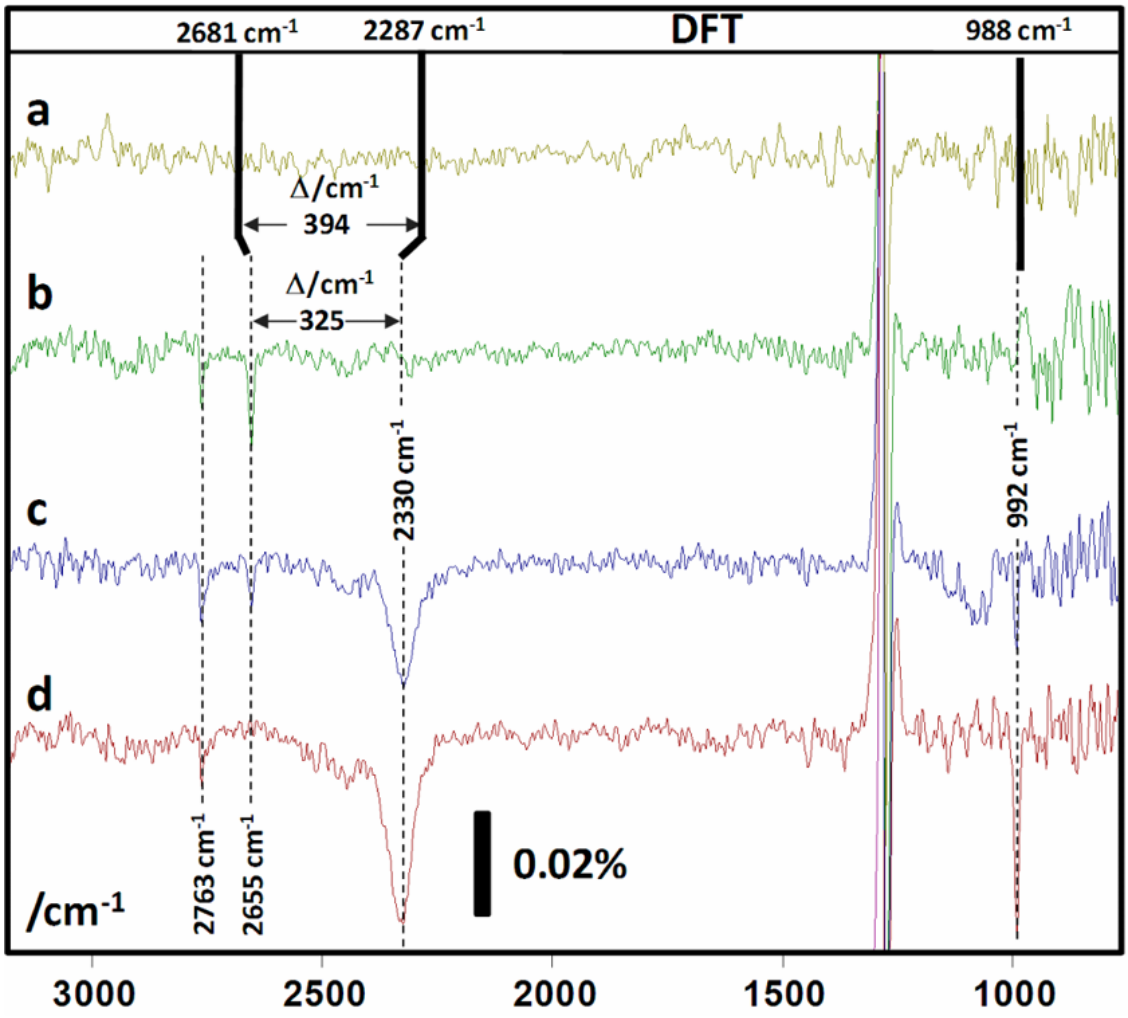


***Figure 4.20:*** *Comparison of the calculated vibrational modes with experimental IRAS spectra. From top to bottom, (a) ethene dosed on a film with no bridging hydroxyls, (b) a film with bridging OD groups before dosing ethene, and (c) and (d) after increasing doses of $C_2H_4$. At the top of the spectra the unscaled DFT frequencies are shown (double cell, unscaled harmonic frequencies, see Computational Details p. 62). The figure is taken from [FDF2].*

***Table 4.7:*** *Calculated changes of O-H bond distances, $\Delta d_{OH}$ (in* pm*), as well as vibrational wavenumbers, $\Delta\nu_{OH}$ (in* $cm^{-1}$*), for CO and $C_2H_4$ adsorbed on the H-2dH film compared to zeolites H-CHA and H-MFI*

| observed | $\Delta\nu_{OH}(CO)$ | $\Delta\nu_{CO}$ | | $\Delta\nu_{OH}(C_2H_4)$ |
|---|---|---|---|---|
| H-MFI | -343 $\pm$ 8[ab], -313 $\pm$ 3[bc] | | | -389[db], -433 $\pm$ 8[bc] |
| H-CHA | -316[e] | +34[e] | | |
| H-2dH | -379 | +40 | | -487 |
| calculated | $\Delta d_{OH}(CO)$ | $\Delta\nu_{OH}(CO)^f$ | $\Delta d_{OH}(C_2H_4)$ | $\Delta\nu_{OH}(C_2H_4)^g$ |
| H-MFI | | | | $-535^h$ |
| H-CHA | +2.66 | $-350$ | +2.58 | $-537$ |
| H-2dH | +2.83 | $-373$ | +2.63 | $-548$ |

[a] Zecchina et al. [92]
[b] Note that very broad bands are obtained which make it difficult to specify a precise number for the shift.
[c] Makarova et al. [93] Taken from Figures 1 and 2 of that paper.
[d] Spoto et al. [47]
[e] Bordiga et al. [94] report a shift of +39 $cm^{-1}$, but uses for CO the value of 2138 $cm^{-1}$ (liquid like). Using 2143 $cm^{-1}$ (gas-phase CO) as reference, the shift is +34 $cm^{-1}$
[f] Anharmonic frequencies obtained from bond distances using the Nachtigall scheme [79].
[g] Unscaled harmonic frequencies
[h] PBE calculations of Hansen et al. [26]

action of these probe molecules with bridging hydroxyls will be studied here for H-2dH and D-2dH.

Figure 4.18 shows that in the DFT calculated structure, the pyridine molecule is protonated upon adsorption on the surface. This has to be expected, since its proton affinity (912 kJ mol$^{-1}$) [95] is higher than that of ammonia (854 kJ mol$^{-1}$), and it has been found previously by DFT that this is a non-activated process [96]. To see whether pyridine also gets protonated in the experiment, one has to examine the observed IRAS spectrum (Figure 4.21) very carefully. On the upside, a careful examination of this spectrum also gives some insight into the molecular orientation, which then can also be compared to the computational results. Figure 4.23 depicts important vibrational modes, along with

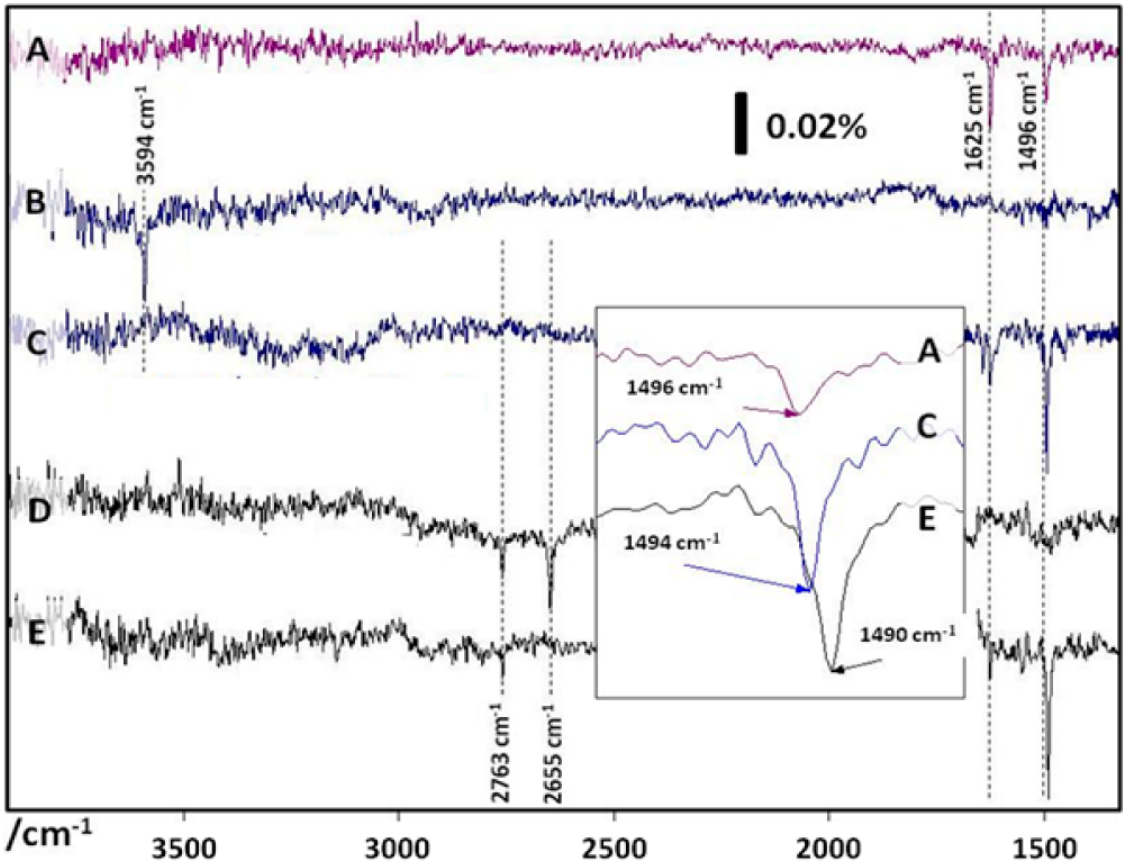


***Figure 4.21:*** *Experimental IRAS results for pyridine adsorption. (A) Pyridine adsorbed on a nonhydroxylated surface. (B) Surface with bridging OH groups before and (C) after Py adsorption. (D) Surface with bridging OD groups before and (E) after pyridine adsorption. The inset shows mode 19a for the three different cases having Py on the surface. The figure is taken from [FDF2].*

the corresponding experimental frequencies, for a free Py molecule, as well as ranges of frequencies that have been reported for $PyH^+$ by adsorption on bridging hydroxyls [96].

The most significant difference between Py and $PyH^+$ occurs in mode 19b, which undergoes a dramatic blue-shift of $\sim 90\,cm^{-1}$. In Figure 4.21, spectrum A corresponds to Py adsorbed at 300 K on a surface with no bridging hydroxyls. Two adsorption bands are evident at 1625 and 1496 $cm^{-1}$, which can be assigned to 8(a or b) and 19a of an adsorbed, non-protonated Py. Since only vibrational modes that have a component perpendicular to the surface plane can be observed by IRAS (see p. 29), and considering the description of the modes shown in Figure 4.23, it is inferred that Py is adsorbed in an orientation such that the molecule plane has a significant component perpendicular to the surface plane, presumably with the N atom toward the surface. Spectrum B shows a surface that has been hydroxylated and shows a typical vibrational mode at 3594 $cm^{-1}$, corresponding to a bridging hydroxyl group. When Py is adsorbed on this surface (spectrum C), the OH stretching peak disappears, and peaks corresponding to 8(a or b) and 19a modes appear in the spectrum at 1625 and 1494 $cm^{-1}$. The disappearance of the OH vibration can be explained by the expected proton abstraction Again, mode 19b, which usually allows a clear distinction between the protonated and non-protonated forms, is not clearly observed in the spectrum due to the IRAS selection rules. The differences between the non-protonated (A) and protonated (C) cases are subtle. They include a change in the intensities of the 19a and 8(a or b) modes, where 19a is more intense for the protonated case while 8(a or b) is significantly more intense for the non-protonated one. Another difference is a 2 $cm^{-1}$ red-shift in the 19a mode for the pyridinium ion with respect to the non-protonated case. The same experiment was repeated for a bridging OD (spectrum D). Two peaks are observed in the OD stretching region at 2763 and 655 $cm^{-1}$, which correspond to a silanol group and a bridging OD group, respectively. (In spectrum B, the silanol group is not observed since the spectrum that was used as a background already had silanol groups present). When pyridine is adsorbed on the surface with bridging OD groups (spectrum E), the peak at 2655 $cm^{-1}$ disappears, indicating the deuteron abstraction by Py, while the silanol group remains. Again in this case, modes 19a and 8(a or b) are observed, but now mode 19a is shifted further down to 1490 $cm^{-1}$. The fact that mode 19b is not observed leads to difficulties to clearly determine whether the molecule is protonated or not. How-

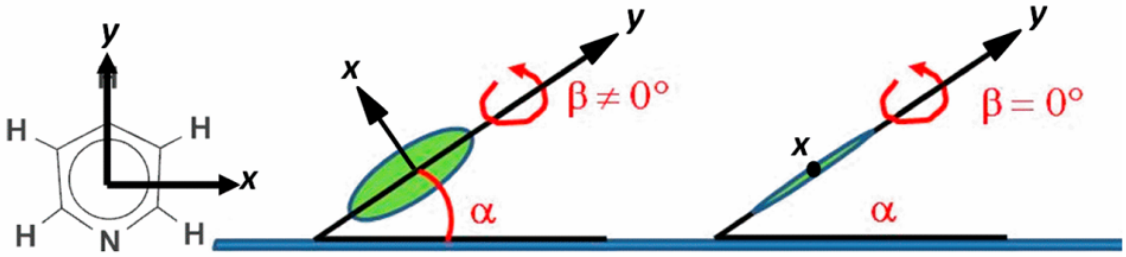


***Figure 4.22:*** *The green oval represents the pyridine molecule. The angles α and β define its orientation with respect to the surface plane. The figure is taken from [FDF2].*

ever, this fact provides information about the orientation of the molecule. When defining the orientation of the molecule with respect to the surface plane two angles have to be considered. We are going to call them $\alpha$ and $\beta$, and these are depicted in Figure 4.22. $\alpha$ is the tilt of the molecule plane with respect to the surface plane, while $\beta$ is the rotation of the molecule around an axis defined along the N atom and the C atom in position 4 in the ring. Let us call this direction y, while x is the direction perpendicular to it within the plane of the molecule, as depicted in Figure 4.22. The main components of the 19b mode are in the x direction. The direction of the x axis depends on the angle $\beta$, and it becomes parallel to the surface with $\beta = 0$. Since only modes perpendicular to the surface can be seen by IRAS, this means that for the mode 19b not to be observed $\beta$ must be $\sim 0$. In addition, for mode 19a to be observed, $\alpha$ must be $> 0$. The calculated value for $\alpha$ in Figure 4.22 is 34°, and the one for $\beta$ is 12°. This showcases a good agreement of the structure predicted by the calculations with the interpretation of the IRAS experiment, concerning the molecular orientation. In the calculations, mode 19a has a frequency of 1470 $cm^{-1}$ for the bridging OH, while it is 1462 $cm^{-1}$ for the bridging OD. This shift to lower wavenumbers for mode 19a when comparing the protonated to the deuterated case is in agreement with what is found experimentally. This helps in identifying this vibrational mode, which in turn is a good indicator for the protonation status of pyridine, as was explained above.

**Ammonia** Figure 4.18 shows that a protonated structure can be formed, with the ammonium ion located on top of the center of the six-membered ring and three of the H atoms pointing toward the surface forming H-bonds to three of the O atoms of the ring, two of which are part of the $[AlO_4]$ tetrahedron. There are two vibrational modes of $NH_4^+$ with

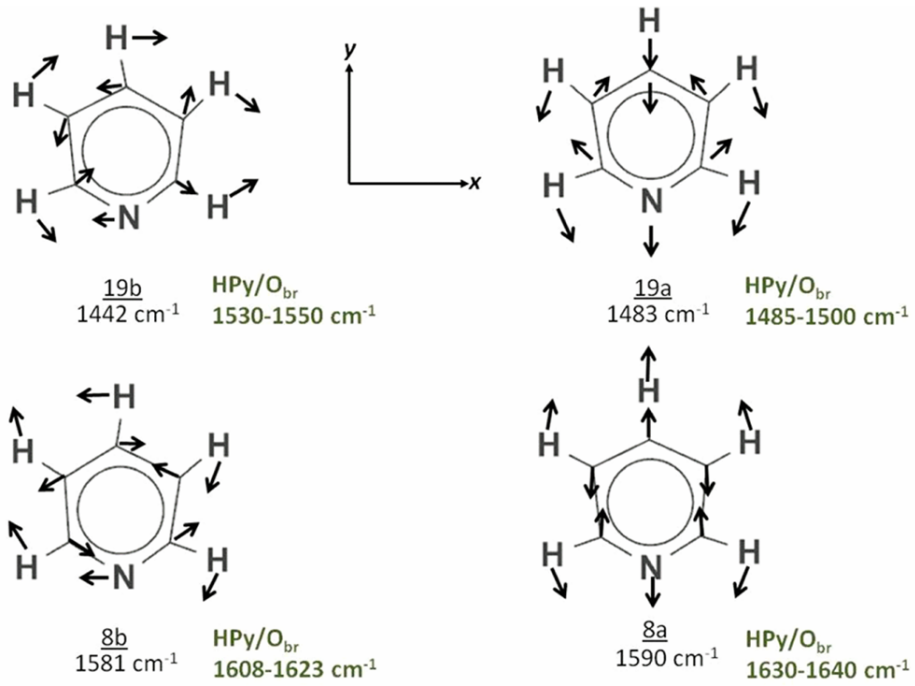


***Figure 4.23:*** *Pyridine modes between* 1400 *and* 1700 $\mathrm{cm}^{-1}$. *The figure is taken from ref. [96].*

strong components perpendicular to the surface plane in this configuration. These are a N-H stretch for the H pointing outward from the surface (3472 $\mathrm{cm}^{-1}$) and an umbrella mode also perpendicular to the surface plane at 1520 $\mathrm{cm}^{-1}$. This allows the assignment of the two modes observed experimentally (Figure 4.24), in agreement with the hypothesis of the proton abstraction, which is expected based on what is known from bulk zeolites. The DFT OH wavenumber for the unloaded zeolite is found at 3608 $\mathrm{cm}^{-1}$, whereas the Nachtigall scheme was used for the latter value (O-H vibration in the zeolite); the former two (N-H stretching modes) are unscaled harmonic frequencies, all calculated for a double cell.

### 4.4.4 Acidity of Bridging Hydroxyls, Comparison to other Zeolites.

The measurement of solid acidity is not trivial. Computationally, it is challenging since the calculation of deprotonation energies is problematic within periodic boundary conditions. If there is an overall charge in the unit cell after deprotonation, it interacts with its periodic images. The system is not stable, the energy diverges. There exist ways to deal with this problem by introducing corrections, like adding a background charge, but

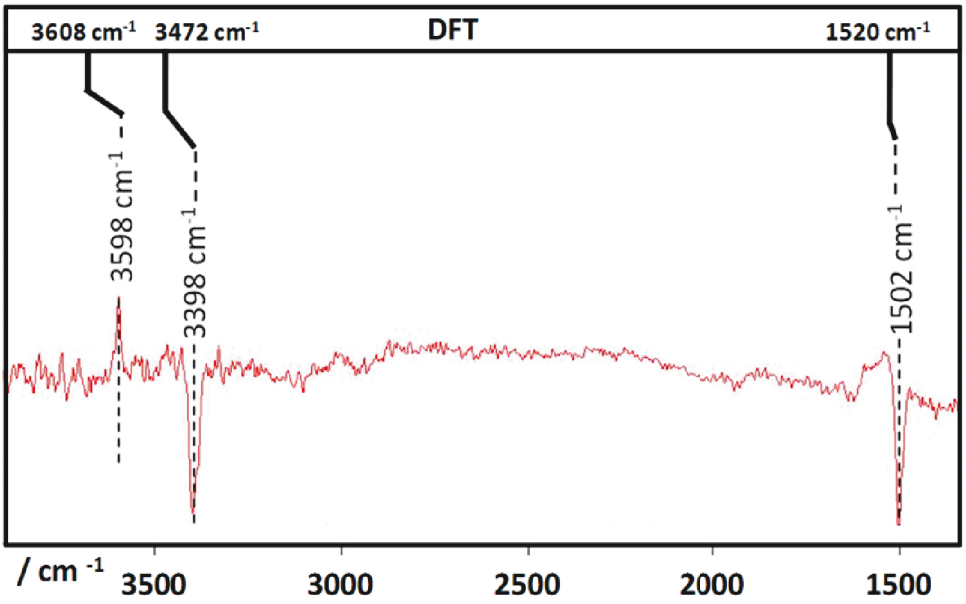


***Figure 4.24:*** *Comparison of the calculated vibrational modes with the experimental IRA spectrum of ammonia adsorbed on a bridging hydroxyl using as a background the spectrum taken before adsorption. At the top of the spectra, DFT frequencies are shown. The unscaled values are shown for the umbrella and NH stretching mode, whereas the* $3608\,\mathrm{cm}^{-1}$ *for the OH stretching mode is the result of the Nachtigall scheme. The calculations were done using a double cell (see Computational Details). The figure is taken from [FDF2].*

it is nevertheless difficult to calculate the deprotonation energy quantitatively. Here, the interaction of the acidic hydroxyl group with probe molecules is used to judge the acidity. To compare the relative acidities of different zeolitic systems, the OH frequency shifts on adsorption of CO and $C_2H_4$ can be compared for different zeolites. Interestingly, there is a clear correlation between the shifts induced by CO and $C_2H_4$. This is in line with the idea that the frequency shift is an indicator for the acidity of the system. Figure 4.25 plots the induced OH vibration shift for a variety of different systems with well-defined structure. The general trend that the CO and $C_2H_4$ induced shifts are strongly correlated, is obvious in the figure. In addition, the observation that was already made based on Table 4.6, is now even more pronounced. The bridging hydroxyls in H-2dH are the most acidic when compared to other zeolites. When trying to find structure-activity relationships, the Al:Si ratio might be an important quantity. The effects of different Al contents as well as the inclusion of the metal support in the DFT calculations are discussed in section 4.3 of this thesis.

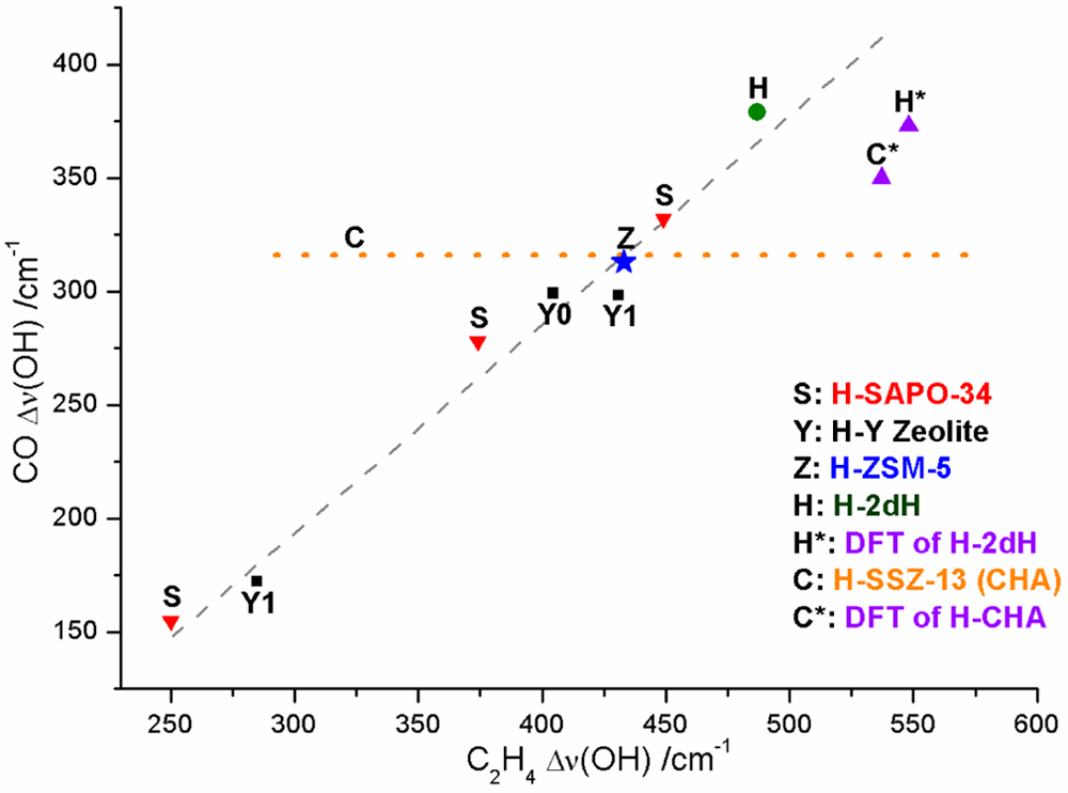


***Figure 4.25:*** *Plot of CO and $C_2H_4$ induced shifts in the OH vibration for different systems, including the film reported in this work (green circle).The orange dotted line corresponds to H-SSZ-13, a zeolite with CHA framework [94]. The red triangles correspond to H-SAPO-34, a silicoaluminophosphate with CHA structure [97]. The black squares correspond to the same H-Y zeolite (FAU framework). Y0 is a non-dealuminated H-Y zeolite. Y1 was dealuminated by isomorphous substitution by treatment with $(NH_4)_2SiF_6$. [98]. The blue star corresponds to H-ZSM-5 (MFI framework type) [93]. The literature analysis and the figure are taken from the joint publication [FDF2].*

### 4.4.5 Conclusions

The interaction of bases of different strength with bridging hydroxyls was studied on a zeolite model system (H-2dH) with a well-defined structure. The adsorption was studied using DFT calculations and compared to experiments that were done under the controlled conditions provided by a UHV environment. While ammonia and pyridine abstract the proton from the bridging hydroxyl to form ammonium and pyridinium ions, respectively, weak bases CO and $C_2H_4$ bind coordinatively to the proton inducing a shift in the OH vibration. Defining this shift as proportional to the acidity of the site, it indicates that the aluminosilicate film is more acidic than conventional zeolites with cavities. However, the adsorption energies are larger in cavities because of larger dispersion contributions for curved surfaces. An acidity in the range of the most acidic (and catalytically active) zeolites validates the use of this well-defined aluminosilicate film as a model system for mechanistic studies of the large number of chemical reactions that are performed on zeolites. This paves the way for improvements in the currently used industrial catalysts once the mechanistic details are well understood. Additionally, the internal vibrational modes of the probe molecules allowed us to infer their orientation with respect to the bridging hydroxyl taking advantage of the IRAS selection rules.

# 5 Summary

This chapter provides a brief summary of all results. It is a collection of the conclusions of sections 4.1 to 4.4 in the results part of this thesis.

**Ultrathin Ti-Silicate Film on a Ru(0001) Surface** Combining experimental techniques with DFT structure and stability predictions resulted in structural model for a well-ordered, ultra-thin Ti-silicate film on a Ru(0001) surface. The film can best be described as a monolayer of corner-sharing [$SiO_4$] tetrahedra on top of a mono- layer formed by [$TiO_6$] octahedra. The layers are connected by shared oxygen atoms at the corners of the [$SiO_4$] tetrahedra and [$TiO_6$] octahedra in the top and bottom layers, respectively. The [$TiO_6$] octahedra are connected to the Ru substrate via oxygen atoms shared by two Ti atoms and one Ru atom. The agreement of the calculated vibrational modes with the experimental infrared reflection absorption (IRA) spectra provides compelling evidence for the proposed structural model and the segregation into pure silica and a 1:1 (Si:Ti) phase. For low Ti contents, segregation is predicted and observed. Next to pristine silica bilayer domains, domains of the proposed Ti-silicate structure are formed. Those results clearly differ from what was found for Al- substitution into pure silica film but are similar to what was recently found for a Fe-containing silicate film.[1]

**Ultrathin Al-Silicate Film on a Ru(0001) Surface** DFT calculations give insight into possible structures of ultrathin aluminosilicate films, prepared on a Ru(0001) surface. The computational findings are compared to the characterization of experimentally prepared

[1] This text is an excerpt from the paper published on the topic [FDF3].

films. Contrary to chemical intuition and some experimental findings, the results obtained by DFT suggest that structures that violate Löwenstein's rule are energetically favorable. DFT and experiment agree that Al preferentially occupies positions in the bottom layer. Computed vibrational modes agree reasonably well with experimental IRAS data for both structures that follow Löwenstein's rule and for some that do not. These computational results weakly support the interpretation of the experimental findings on the aluminosilicate films, regarding them as model systems for zeolites.

**Acidity of the H-2dH Zeolite: Influence of Al Content and Metal Support** The interaction of CO molecules with bridging hydroxyls of two-dimensional aluminosilicate films was studied using periodic DFT. Three different model systems were compared, namely a free-standing model system with one Al atom per unit cell and one acidic hydroxyl group, the same film, but now supported on a Ru(0001) surface with pre-adsorbed oxygen, and finally, the Ru-supported film with the Al/Si ratio raised to 3/5 while still including only one bridging hydroxyl group. In the last case, the film has an overall negative charge, with some electrons transferred from the metal. This system comes closest to what probably exists under experimental conditions. It was investigated how much the inclusions of these aspects in the structural model effect the calculated adsorption energies and OH frequency shifts on CO adsorption, which is an indicator of acidity. Increasing the Al/Si ratio reduced the adsorption energies and the OH frequency shifts, while adding a Ru-substrate to the model had the opposite effect. Adding both effects leads to at least some cancellation of errors. Using the simplified model system that disregards the role of the metal support and has an unrealistically low Al/Si ratio can therefore still give a rather good agreement with the experiment.

**Adsorption of Probe Molecules on Zeolites and a Two-Dimensional Zeolite Model System** The interaction of bases of different strength with bridging hydroxyls was studied on a zeolite model system (H-2dH) with a well-defined structure. The adsorption was studied using DFT calculations and compared to experiments that were done under

the controlled conditions provided by a UHV environment. While ammonia and pyridine abstract the proton from the bridging hydroxyl to form ammonium and pyridinium ions, respectively, weak bases CO and $C_2H_4$ bind coordinatively to the proton inducing a shift in the OH vibration. Defining this shift as proportional to the acidity of the site, it indicates that the aluminosilicate film is more acidic than conventional zeolites with cavities. However, the adsorption energies are larger in cavities because of larger dispersion contributions for curved surfaces. An acidity in the range of the most acidic (and catalytically active) zeolites validates the use of this well-defined aluminosilicate film as a model system for mechanistic studies of the large number of chemical reactions that are performed on zeolites. This paves the way for improvements in the currently used industrial catalysts once the mechanistic details are well understood. Additionally, the internal vibrational modes of the probe molecules allowed us to infer their orientation with respect to the bridging hydroxyl taking advantage of the IRAS selection rules.[1]

[1]This text is an only slightly changed excerpt from the paper published on the topic [FDF2].

# Bibliography

[1] W. Vermeiren and J. P. Gilson, "Impact of Zeolites on the Petroleum and Petrochemical Industry," *Top. Catal.*, vol. 52, no. 9, pp. 1131–1161, 2009.

[2] A. Corma, M. T. Navarro, and J. P. Pariente, "Synthesis of an ultralarge pore Titanium Silicate Isomorphous to MCM-41 and its Application as a Catalyst for Selective Oxidation of Hydrocarbons," *Chem. Commun.*, no. 2, pp. 147–148, 1994.

[3] J. A. van Bokhoven and C. Lamberti, "Structure of aluminum, iron, and other heteroatoms in zeolites by x-ray absorption spectroscopy," *Coord. Chem. Rev.*, vol. 277–278, pp. 275 – 290, 2014. Following Chemical Structures using Synchrotron Radiation.

[4] 17th International Zeolite Conference 2013, "Scientific Program."

[5] H. Pastore, S. Coluccia, and L. Marchese, "Porous aluminophosphates: From molecular sieves to designed acid catalysts," *Annu. Rev. Mater. Res.*, vol. 35, pp. 351–395, 2005.

[6] J. Liu, L. Chen, H. Cui, J. Zhang, L. Zhang, and C.-Y. Su, "Applications of metal-organic frameworks in heterogeneous supramolecular catalysis," *Chem. Soc. Rev.*, vol. 43, no. 16, pp. 6011–6061, 2014.

[7] H. Furukawa, U. Mueller, and O. M. Yaghi, ""Heterogeneity within Order" in Metal-Organic Frameworks," *Angew. Chem. Int. Ed.*, vol. 54, no. 11, SI, pp. 3417–3430, 2015.

[8] C. Lamberti, A. Zecchina, E. Groppo, and S. Bordiga, "Probing the surfaces of heterogeneous catalysts by in situ IR spectroscopy," *Chem. Soc. Rev.*, vol. 39, pp. 4951–5001, 2010.

[9] J. A. Lercher, C. Gründling, and G. Eder-Mirth, "Infrared studies of the surface acidity of oxides and zeolites using adsorbed probe molecules," *Catal. Today*, vol. 27, no. 3–4, pp. 353 – 376, 1996. Vibrational Spectroscopy of Adsorbed Molecules and Surface Species on Metal Oxides.

[10] J. B. Nicholas and J. F. Haw, "The prediction of persistent carbenium ions in zeolites," *J. Am. Chem. Soc.*, vol. 120, no. 45, pp. 11804–11805, 1998.

[11] V. Termath, F. Haase, J. Sauer, J. Hutter, and M. Parrinello, "Understanding the Nature of Water Bound to Solid Acid Surfaces. Ab Initio Simulation on HSAPO-34," *J. Am. Chem. Soc.*, vol. 120, no. 33, pp. 8512–8516, 1998.

[12] J. Sauer, "Proton transfer in zeolites," in *Hydrogen-Transfer Reactions* (J. T. Hynes, J. P. Klinman, H.-H. Limbach, and R. L. Schowen, eds.), vol. 2, pp. 685–707, Weinheim, Germany: Wiley-VCH Verlag GmbH & Co. KGaA, 2007.

[13] W. Löwenstein, "The distribution of aluminium in the tetrahedra of silicates and aluminates," *Am. Mineral*, vol. 39, pp. 92–96, 1954.

[14] C. S. Cundy and P. A. Cox, "The hydrothermal synthesis of zeolites: Precursors, intermediates and reaction mechanism," *Microporous Mesoporous Mat.*, vol. 82, no. 1–2, pp. 1 – 78, 2005.

[15] C. R. A. Catlow, S. T. Bromley, S. Hamad, M. Mora-Fonz, A. A. Sokol, and S. M. Woodley, "Modelling nano-clusters and nucleation," *Phys. Chem. Chem. Phys..*, vol. 12, pp. 786–811, 2010.

[16] S. Malola, S. Svelle, F. L. Bleken, and O. Swang, "Detailed reaction paths for zeolite dealumination and desilication from density functional calculations," *Angew. Chem. Int. Ed.*, vol. 51, no. 3, pp. 652–655, 2012.

[17] J. Sauer, "Acidic catalysis by zeolites and the active site concept," in *On Catalysis* (W. Reschetilowski and W. Hönle, eds.), vol. 2 of *Edition Ostwald*, pp. 136—-161, Berlin Germany: VWB - Verlag für Wissenschaft und Bildung, 2010.

[18] B. Smit and T. L. M. Maesen, "Molecular simulations of zeolites: Adsorption, diffusion, and shape selectivity," *Chem. Rev.*, vol. 108, no. 10, pp. 4125–4184, 2008. PMID: 18817356.

[19] J. Sauer, "Molecular models in ab initio studies of solids and surfaces: from ionic crystals and semiconductors to catalysts," *Chem. Rev.*, vol. 89, no. 1, pp. 199–255, 1989.

[20] J. Sauer, P. Ugliengo, E. Garrone, and V. R. Saunders, "Theoretical study of van der waals complexes at surface sites in comparison with the experiment," *Chem. Rev.*, vol. 94, no. 7, pp. 2095–2160, 1994.

[21] Y. Zhao and D. G. Truhlar, "Benchmark data for interactions in zeolite model complexes and their use for assessment and validation of electronic structure methods," *J. Phys. Chem. C*, vol. 112, no. 17, pp. 6860–6868, 2008.

[22] J. Sauer and M. Sierka, "Combining quantum mechanics and interatomic potential functions in ab initio studies of extended systems," *J. Comp. Chem.*, vol. 21, no. 16, pp. 1470–1493, 2000.

[23] C. Tuma and J. Sauer, "A hybrid mp2/planewave-dft scheme for large chemical systems: proton jumps in zeolites," *Chem. Phys. Lett.*, vol. 387, no. 4–6, pp. 388 – 394, 2004.

[24] C. Tuma and J. Sauer, "Treating dispersion effects in extended systems by hybrid mp2:dft calculations-protonation of isobutene in zeolite ferrierite," *Phys. Chem. Chem. Phys.*, vol. 8, pp. 3955–3965, 2006.

[25] S. Svelle, C. Tuma, X. Rozanska, T. Kerber, and J. Sauer, "Quantum chemical model-

ing of zeolite-catalyzed methylation reactions: Toward chemical accuracy for barriers," *J. Am. Chem. Soc.*, vol. 131, no. 2, pp. 816–825, 2009. PMID: 19099476.

[26] N. Hansen, T. Kerber, J. Sauer, A. T. Bell, and F. J. Keil, "Quantum Chemical Modeling of Benzene Ethylation over H-ZSM-5 Approaching Chemical Accuracy: A Hybrid MP2:DFT Study," *J. Am. Chem. Soc.*, vol. 132, no. 33, pp. 11525–11538, 2010. PMID: 20677757.

[27] T. Kerber, M. Sierka, and J. Sauer, "Application of semiempirical long-range dispersion corrections to periodic systems in density functional theory," *J. Comp. Chem.*, vol. 29, no. 13, pp. 2088–2097, 2008.

[28] J. Moellmann and S. Grimme, "DFT-D3 Study of Some Molecular Crystals," *J. Phys. Chem. C*, vol. 118, no. 14, pp. 7615–7621, 2014.

[29] M. Rybicki and J. Sauer, "Acidity of two-dimensional zeolites," *Phys. Chem. Chem. Phys.*, vol. 17, pp. 27873–27882, 2015.

[30] M. Leslie and N. J. Gillan, "The energy and elastic dipole tensor of defects in ionic crystals calculated by the supercell method," *J. Phys. Condens. Mat,*, vol. 18, no. 5, p. 973, 1985.

[31] A. D. Boese and J. Sauer, "Accurate adsorption energies of small molecules on oxide surfaces: CO-MgO(001)," *Phys. Chem. Chem. Phys.*, vol. 15, pp. 16481–16493, 2013.

[32] G. Piccini, M. Alessio, J. Sauer, Y. Zhi, Y. Liu, R. Kolvenbach, A. Jentys, and J. A. Lercher, "Accurate Adsorption Thermodynamics of Small Alkanes in Zeolites. Ab initio Theory and Experiment for H-Chabazite," *J. Phys. Chem. C*, vol. 119, no. 11, pp. 6128–6137, 2015.

[33] J. Sauer and H.-J. Freund, "Models in catalysis," *Catal. Lett.*, vol. 145, no. 1, pp. 109–125, 2015.

[34] C. Büchner, L. Lichtenstein, X. Yu, J. A. Boscoboinik, B. Yang, W. E. Kaden, M. Heyde, S. K. Shaikhutdinov, R. Włodarczyk, M. Sierka, J. Sauer, and H.-J. Freund, "Ultrathin

silica films: The atomic structure of two-dimensional crystals and glasses," *Chem. Eur. J.*, vol. 20, no. 30, pp. 9176–9183, 2014.

[35] https://www.unicat.tu-berlin.de [accessed 14-August-2015].

[36] https://www.chemie.hu-berlin.de/de/forschung/sfb1109 [accessed 14-August-2015].

[37] B. Yang, W. E. Kaden, X. Yu, J. A. Boscoboinik, Y. Martynova, L. Lichtenstein, M. Heyde, M. Sterrer, R. Wlodarczyk, M. Sierka, J. Sauer, S. Shaikhutdinov, and H.-J. Freund, "Thin silica films on Ru(0001): monolayer, bilayer and three-dimensional networks of [SiO4] tetrahedra," *Phys. Chem. Chem. Phys.*, vol. 14, pp. 11344–11351, 2012.

[38] S. Shaikhutdinov and H.-J. Freund, "Ultrathin silica films on metals: The long and winding road to understanding the atomic structure," *Adv. Mater.*, vol. 25, no. 1, pp. 49–67, 2013.

[39] S. Shaikhutdinov and H.-J. Freund, "Metal-supported aluminosilicate ultrathin films as a versatile tool for studying the surface chemistry of zeolites," *ChemPhysChem*, vol. 14, no. 1, pp. 71–77, 2013.

[40] W. J. Roth, P. Nachtigall, R. E. Morris, and J. Čejka, "Two-dimensional zeolites: Current status and perspectives," *Chem. Rev.*, vol. 114, no. 9, pp. 4807–4837, 2014. PMID: 24555638.

[41] J. A. Boscoboinik, X. Yu, B. Yang, F. D. Fischer, R. Wlodarczyk, M. Sierka, S. Shaikhutdinov, J. Sauer, and H.-J. Freund, "Modeling Zeolites with Metal-Supported Two-Dimensional Aluminosilicate Films," *Angew. Chem. Int. Ed.*, vol. 51, no. 24, pp. 6005–6008, 2012.

[42] J. A. Boscoboinik, X. Yu, E. Emmez, B. Yang, S. Shaikhutdinov, F. D. Fischer, J. Sauer, and H.-J. Freund, "Interaction of Probe Molecules with Bridging Hydroxyls of Two-

Dimensional Zeolites: A Surface Science Approach," *J. Phys. Chem. C*, vol. 117, no. 26, pp. 13547–13556, 2013.

[43] R. Wlodarczyk, J. Sauer, X. Yu, J. A. Boscoboinik, B. Yang, S. Shaikhutdinov, and H.-J. Freund, "Atomic structure of an ultrathin fe-silicate film grown on a metal: A monolayer of clay?," *J. Am. Chem. Soc.*, vol. 135, no. 51, pp. 19222–19228, 2013.

[44] D. Stacchiola, S. Kaya, J. Weissenrieder, H. Kuhlenbeck, S. Shaikhutdinov, H.-J. Freund, M. Sierka, T. K. Todorova, and J. Sauer, "Synthesis and structure of ultrathin aluminosilicate films," *Angew. Chem. Int. Ed.*, vol. 45, no. 45, pp. 7636–7639, 2006.

[45] A. Lucas, I. Derycke, P. Lambin, J.-P. Vigneron, L. Leherte, M. Elanany, J.-M. André, A. Larin, and D. Vercauteren, "Confinement in molecular sieves: The pioneering physical concepts," *J. Mol. Catal. A-Chem.*, vol. 305, no. 1–2, pp. 16 – 23, 2009. In memory of Eric Derouane.

[46] J.-C. Lavalley, S. Jolly-Feaugas, A. Janin, and J. Saussey, "In situ Fourier transform infrared studies of active sites and reaction mechanisms in heterogeneous catalysis: hydrocarbon conversion on H-zeolites," *Microchim. Acta, Suppl.*, vol. 14, pp. 51–56, 1997.

[47] G. Spoto, S. Bordiga, G. Ricchiardi, D. Scarano, A. Zecchina, and E. Borello, "IR study of ethene and propene oligomerization on H-ZSM-5: hydrogen-bonded precursor formation, initiation and propagation mechanisms and structure of the entrapped oligomers," *J. Chem. Soc., Faraday Trans.*, vol. 90, pp. 2827–2835, 1994.

[48] C. Martínez and A. Corma, "Inorganic molecular sieves: Preparation, modification and industrial application in catalytic processes," *Coord. Chem. Rev.*, vol. 255, no. 13–14, pp. 1558 – 1580, 2011. Industrial Chemistry.

[49] J. A. Boscoboinik, X. Yu, B. Yang, S. Shaikhutdinov, and H.-J. Freund, "Building blocks of zeolites on an aluminosilicate ultra-thin film," *Microporous Mesoporous Mat.*, vol. 165, pp. 158 – 162, 2013.

[50] C. J. Cramer, *Essentials of Computational Chemistry*. Weinheim, Germany: Wiley-VCH Verlag GmbH, second ed., 2004.

[51] W. Koch and M. C. Holthausen, *A Chemist's Guide to Density Functional Theory*. Weinheim, Germany: Wiley-VCH Verlag GmbH, second ed., 2001.

[52] R. Hoffmann, "How chemistry and physics meet in the solid state," *Angew. Chem. Int. Ed.*, vol. 26, no. 9, pp. 846–878, 1987.

[53] in *Quantum-Mechanical Ab-initio Calculation of the Properties of Crystalline Materials* (C. Pisani, ed.), vol. 67 of *Lecture Notes in Chemistry*, Berlin Heidelberg, Germany: Springer-Verlag, 1996.

[54] E. Pehlke, "The plane-wave pseudopotential method." University Lecture Script. http://th.fhi-berlin.mpg.de/th/Meetings/FHImd2001/pehlke1.pdf [accessed 17-August-2015].

[55] H. J. Monkhorst and J. D. Pack, "Special Points for Brillouin-Zone Integrations," *Phys. Rev. B*, vol. 13, no. 12, pp. 5188–5192, 1976.

[56] A. D. Corso, "Reciprocal Space Integration and Special-Point Techniques," in *Quantum-Mechanical Ab-initio Calculation of the Properties of Crystalline Materials* (C. Pisani, ed.), vol. 67 of *Lecture Notes in Chemistry*, pp. 77–89, Berlin Heidelberg, Germany: Springer-Verlag, 1996.

[57] P. Blochl, "Projector Aaugmented-Wave Method," *Phys. Rev. B*, vol. 50, no. 24, pp. 17953–17979, 1994.

[58] F. Jensen, *Introduction to Computational Chemistry*. Weinheim, Germany: Wiley-VCH Verlag GmbH, second ed., 2007.

[59] J. P. Perdew, A. Ruzsinszky, J. Tao, V. N. Staroverov, G. E. Scuseria, and G. I. Csonka, "Prescription for the design and selection of density functional approximations: More constraint satisfaction with fewer fits," *J. Chem. Phys.*, vol. 123, no. 6, 2005.

[60] J. Perdew, K. Burke, and M. Ernzerhof, "Generalized gradient approximation made simple (vol 77, pg 3865, 1996)," *Phys. Rev. Lett.*, vol. 78, no. 7, p. 1396, 1997.

[61] O. Gunnarsson and B. I. Lundqvist, "Exchange and correlation in atoms, molecules, and solids by the spin-density-functional formalism," *Phys. Rev. B*, vol. 13, pp. 4274–4298, 1976.

[62] D. C. Langreth and J. P. Perdew, "Exchange-correlation energy of a metallic surface: Wave-vector analysis," *Phys. Rev. B*, vol. 15, pp. 2884–2901, 1977.

[63] D. Bohm and D. Pines, "A collective description of electron interactions: Iii. coulomb interactions in a degenerate electron gas," *Phys. Rev.*, vol. 92, pp. 609–625, 1953.

[64] M. Gell-Mann and K. A. Brueckner, "Correlation energy of an electron gas at high density," *Phys. Rev.*, vol. 106, pp. 364–368, 1957.

[65] D. Rappoport, N. R. M. Crawford, F. Furche, and K. Burke, "Which functional should I choose?," in *Computational Inorganic and Bioinorganic Chemistry* (E. I. Solomon, R. B. King, and R. A. Scott, eds.), Chichester, England: Wiley, 2009.

[66] S. Grimme, "Semiempirical GGA-type density functional constructed with a long-range dispersion correction," *J. Comp. Chem.*, vol. 27, no. 15, pp. 1787–1799, 2006.

[67] H. Krieg and S. Grimme, "Thermochemical benchmarking of hydrocarbon bond separation reaction energies: Jacob's ladder is not reversed!," *Mol. Phys.*, vol. 108, no. 19-20, pp. 2655–2666, 2010.

[68] L. Goerigk and S. Grimme, "A thorough benchmark of density functional methods for general main group thermochemistry, kinetics, and noncovalent interactions," *Phys. Chem. Chem. Phys.*, vol. 13, pp. 6670–6688, 2011.

[69] J. V. der Mynsbrugge, K. Hemelsoet, M. Vandichel, M. Waroquier, and V. V. Speybroeck, "Efficient approach for the computational study of alcohol and nitrile adsorption in h-zsm-5," *J. Phys. Chem. C*, vol. 116, no. 9, pp. 5499–5508, 2012.

[70] D. Wales, *Energy Landscapes. Applications to Clusters, Biomolecules and Glasses.* Cambridge: Cambridge University Press, 2003.

[71] R. S. Włodarczyk, *Surface Structure Predictions and Development of Global Exploration Tools*. PhD thesis, Humboldt-Universität zu Berlin, 2015.

[72] M. P. Teter, M. C. Payne, and D. C. Allan, "Solution of schrödinger's equation for large systems," *Phys. Rev. B*, vol. 40, pp. 12255–12263, 1989.

[73] P. Polavarapu, *Vibrational Spectra: Principles and Applications with Emphasis on Optical Activity*. Studies in Physical and Theoretical Chemistry, Elsevier Science, 1998.

[74] M. Sterrer, "Modern methods in heterogeneous catalysis, vibrational spectroscopy, class 2007/2008." Lecture Script. http://www.fhi-berlin.mpg.de/acnew/department/pages/teaching/pages/teaching__wintersemester__2007_2008/sterrer_vibspec_091107.pdf [accessed 21-August-2015].

[75] G. Rauhut and P. Pulay, "Transferable scaling factors for density functional derived vibrational force fields," *J. Phys. Chem.*, vol. 99, no. 10, pp. 3093–3100, 1995.

[76] J. Perdew, K. Burke, and M. Ernzerhof, "Generalized gradient approximation made simple," *Phys. Rev. Lett.*, vol. 77, no. 18, pp. 3865–3868, 1996.

[77] B. Santra, *Density-Functional Theory Exchange-Correlation Functionals for Hydrogen Bonds in Water*. PhD thesis, Technische Universität Berlin, 2010.

[78] O. Bludský, M. Silhan, P. Nachtigall, T. Bucko, L. Benco, and J. Hafner, "Theoretical investigation of co interaction with copper sites in zeolites: Periodic dft and hybrid quantum mechanical/interatomic potential function study," *J. Phys. Chem. B*, vol. 109, no. 19, pp. 9631–9638, 2005.

[79] P. Nachtigall, O. Bludsky, L. Grajciar, D. Nachtigallova, M. R. Delgado, and C. O. Arean, "Computational and FTIR spectroscopic studies on carbon monoxide and dinitrogen adsorption on a high-silica H-FER zeolite," *Phys. Chem. Chem. Phys.*, vol. 11, no. 5, pp. 791–802, 2009.

[80] G. Kresse and J. Furthmuller, "Efficiency of ab-initio total energy calculations for metals and semiconductors using a plane-wave basis set," *Comput. Mater. Sci.*, vol. 6, no. 1, pp. 15–50, 1996.

[81] G. Kresse and J. Furthmuller, "Efficient iterative schemes for ab initio total-energy calculations using a plane-wave basis set," *Phys. Rev. B*, vol. 54, no. 16, pp. 11169–11186, 1996.

[82] G. Kresse and D. Joubert, "From ultrasoft pseudopotentials to the projector augmented-wave method," *Phys. Rev. B*, vol. 59, no. 3, pp. 1758–1775, 1999.

[83] D. Loeffler, J. J. Uhlrich, M. Baron, B. Yang, X. Yu, L. Lichtenstein, L. Heinke, C. Buechner, M. Heyde, S. Shaikhutdinov, H. J. Freund, R. Wlodarczyk, M. Sierka, and J. Sauer, "Growth and Structure of Crystalline Silica Sheet on Ru(0001)," *Phys. Rev. Lett.*, vol. 105, no. 14, 2010.

[84] R. Wlodarczyk, M. Sierka, J. Sauer, D. Loeffler, J. J. Uhlrich, X. Yu, B. Yang, I. M. N. Groot, S. Shaikhutdinov, and H. J. Freund, "Tuning the electronic structure of ultra-thin crystalline silica films on Ru(0001)," *Phys. Rev. B*, vol. 85, no. 8, 2012.

[85] A. J. M. de Man and J. Sauer, "Coordination, structure, and vibrational spectra of titanium in silicates and zeolites in comparison with related molecules. an ab initio study," *J. Phys. Chem.*, vol. 100, no. 12, pp. 5025–5034, 1996.

[86] J. Grüner, "The crystal structures of talc and pyrophyllite.," *Z. Kristallogr.*, vol. 88, no. 5/6, pp. 412–419, 1934.

[87] G. Ferraris, A. Bloise, and M. Cadoni, "Layered titanosilicates - A review and some results on the hydrothermal synthesis of bafertisite," *Microporous Mesoporous Mat.*, vol. 107, no. 1-2, pp. 108–112, 2008. Workshop on Innovative Applications of Layered Materials: from Catalysis to Nanotechnology, Alessandria, Italy, SEP 01-02, 2006.

[88] A. Männig, Z. Zhao, D. Rosenthal, K. Christmann, H. Hoster, H. Rauscher, and R. J.

Behm, "Structure and growth of ultrathin titanium oxide films on ru(0001)," *Surf. Sci.*, vol. 576, no. 1–3, pp. 29 – 44, 2005.

[89] E. Dempsey, "Acid Strength and Aluminum Site Reactivity of Y Zeolites," *J. Catal.*, vol. 33, no. 3, pp. 497–499, 1974.

[90] N. W. Cant and W. Hall, "Studies of the hydrogen held by solids: XXI. The interaction between ethylene and hydroxyl groups of a Y-zeolite at elevated temperatures ," *J. Catal.*, vol. 25, no. 1, pp. 161 – 172, 1972.

[91] J. P. Merrick, D. Moran, and L. Radom, "An evaluation of harmonic vibrational frequency scale factors," *J. Phys. Chem. A*, vol. 111, no. 45, pp. 11683–11700, 2007. PMID: 17948971.

[92] A. Zecchina, S. Bordiga, G. Spoto, D. Scarano, G. Petrini, G. Leofanti, M. Padovan, and C. O. Arean, "Low-temperature Fourier-transform infrared investigation of the interaction of CO with nanosized ZSM5 and silicalite," *J. Chem. Soc., Faraday Trans.*, vol. 88, pp. 2959–2969, 1992.

[93] M. A. Makarova, A. F. Ojo, K. Karim, M. Hunger, and J. Dwyer, "FTIR study of weak hydrogen bonding of Broensted hydroxyls in zeolites and aluminophosphates," *J. Phys. Chem.*, vol. 98, no. 14, pp. 3619–3623, 1994.

[94] S. Bordiga, L. Regli, D. Cocina, C. Lamberti, M. Bjørgen, and K. P. Lillerud, "Assessing the acidity of high silica chabazite H-SSZ-13 by FTIR using CO as molecular probe: Comparison with H-SAPO-34," *J. Phys. Chem. B*, vol. 109, no. 7, pp. 2779–2784, 2005. PMID: 16851287.

[95] G. Busca, "The surface acidity of solid oxides and its characterization by IR spectroscopic methods. An attempt at systematization," *Phys. Chem. Chem. Phys.*, vol. 1, pp. 723–736, 1999.

[96] M. Castellà-Ventura, Y. Akacem, and E. Kassab, "Vibrational analysis of pyridine

adsorption on the brønsted acid sites of zeolites based on density functional cluster calculations," *J. Phys. Chem. C*, vol. 112, no. 48, pp. 19045–19054, 2008.

[97] G. A. V. Martins, G. Berlier, S. Coluccia, H. O. Pastore, G. B. Superti, G. Gatti, and L. Marchese, "Revisiting the Nature of the Acidity in Chabazite-Related Silicoaluminophosphates: Combined FTIR and $^{29}$Si MAS NMR Study," *J. Phys. Chem. C*, vol. 111, no. 1, pp. 330–339, 2007.

[98] M. Maache, *Etude par spectroscopie infrarouge de l'effet de la structure et de la désalumination de divers zéolithes sur leur acidité de Bronsted.* PhD thesis, Université de Caen, 1992.

# Appendix

## List of Structures and absolute Energies

### Ultrathin Ti-Silicate Film on a Ru(0001) surface

Table 1 lists all structures that are discussed in section 4.1 together with their absolute energies as calculated with VASP. The computational details are discussed in subsection 4.1.1. All relevant files are stored in the archives of the group of Prof. Sauer. The path to the directories is `/archive/publications/p342`.

***Table 1:*** *Absolute energies in* eV *for all structures that are discussed in section 4.1. The ordering of the structures is different from table 4.1. There, the structures are ordered by energy. Here, the structures are labeled by the order in which they were created and investigated and this is also how they are ordered in the archives. The energies reported here are the PBE energies, before re-optimization by PBE+D*

| Structure | Energy |
|---|---|
| $Si_8O_{16} \cdot 2O/Ru$ | -556.631225 |
| $TiSi_7O_{16} \cdot 2O/Ru$, v1 | -559.041730 |
| $TiSi_7O_{16} \cdot 2O/Ru$, v2 | -559.033101 |
| $TiSi_7O_{16} \cdot 2O/Ru$, v3 | -559.033537 |
| $TiSi_7O_{16} \cdot 2O/Ru$, v4 | -559.040305 |
| $TiSi_7O_{16} \cdot 2O/Ru$, v5 | -559.033349 |
| $TiSi_7O_{16} \cdot 2O/Ru$, v6 | -559.046371 |
| $TiSi_7O_{16} \cdot 2O/Ru$, v7 | -559.033036 |
| $TiSi_7O_{16} \cdot 2O/Ru$, v8 | -559.046547 |
| $Ti_2Si_6O_{16} \cdot 2O/Ru$, v1 | -561.570597 |
| $Ti_2Si_6O_{16} \cdot 2O/Ru$, v2 | -561.384389 |
| $Ti_2Si_6O_{16} \cdot 2O/Ru$, v3 | -561.495585 |
| $Ti_2Si_6O_{16} \cdot 2O/Ru$, v4 | -561.389197 |
| $Ti_2Si_6O_{16} \cdot 2O/Ru$, v5 | -561.570917 |
| $Ti_2Si_6O_{16} \cdot 2O/Ru$, v6 | -561.518238 |
| $Ti_2Si_6O_{16} \cdot 2O/Ru$, v7 | -561.329727 |
| $Ti_3Si_5O_{16} \cdot 2O/Ru$, v1 | -563.925216 |
| $Ti_3Si_5O_{16} \cdot 2O/Ru$, v2 | -563.918483 |
| $Ti_3Si_5O_{16} \cdot 2O/Ru$, v3 | -563.869591 |
| $Ti_3Si_5O_{16} \cdot 2O/Ru$, v4 | -563.925244 |
| $Ti_3Si_5O_{16} \cdot 2O/Ru$, v5 | -563.922039 |
| $Ti_3Si_5O_{16} \cdot 2O/Ru$, v6 | -563.849917 |
| $Ti_4Si_4O_{16} \cdot 2O/Ru$, v1 | -566.271423 |
| $Ti_4Si_4O_{16} \cdot 2O/Ru$, v2 | -566.333178 |
| $Ti_4Si_4O_{16} \cdot 2O/Ru$, v3 | -566.274770 |
| $Ti_4Si_4O_{16} \cdot 2O/Ru$, v4 | -566.015927 |
| $Ti_4Si_4O_{16} \cdot 2O/Ru$, v5 | -566.303501 |
| $Ti_4Si_4O_{16} \cdot 2O/Ru$, v6 | -566.293255 |
| $Ti_4Si_4O_{16} \cdot 2O/Ru$, v7 | -566.121458 |
| $Ti_4Si_4O_{16} \cdot 2O/Ru$, v8 | -566.255570 |
| $Ti_4Si_4O_{16} \cdot 2O/Ru$, v9 | -566.342550 |
| $Ti_4Si_4O_{16} \cdot 2O/Ru$, v10 | -566.392727 |
| $Ti_4Si_4O_{16} \cdot 2O/Ru$, v11 | -566.287364 |
| $Ti_4Si_4O_{16} \cdot 2O/Ru$, v12 | -566.325117 |
| $Ti_4Si_4O_{16} \cdot 2O/Ru$, v13 | -566.254337 |
| $Ti_4Si_4O_{16} \cdot 2O/Ru$, v14 | -566.348832 |
| $Ti_4Si_4O_{16} \cdot 2O/Ru$, v15 | -566.309705 |
| $Ti_4Si_4O_{16} \cdot 2O/Ru$, v16 | -568.644708 |

## Ultrathin Al-Silicate Film on a Ru(0001) surface

Tables 2 to 5 list all structures that are discussed in section 4.2 together with their absolute energies as calculated with VASP. Also included are the absolute energies for some additional structures that were found. They were different local minima on the PES that were energetically less favorable than those reported in section 4.2. The computational details are discussed in subsection 4.2.1. Tables 2 to 5 show results for calculations that were performed by R. Włodarczyk, while the calculations for the structures shown in table 5 were performed by the author of this thesis. All relevant files are stored in the archives of the group of Prof. Sauer. The path to the directories is `/archive/frfi/al-sio2-bilayer-on-Ru`.

***Table 2:*** *Absolute energies in* eV *for structures without surface oxygen that are discussed in section 4.2.*

| Structure | Energy |
|---|---|
| $Si_8O_{16}$/Ru | -566.237035 |
| $Al_1Si_7O_{16}$/Ru, v18 | -566.647519 |
| $Al_1Si_7O_{16}$/Ru, v20 | -565.501249 |
| $Al_2Si_6O_{16}$/Ru, v2 | -565.086514 |
| $Al_2Si_6O_{16}$/Ru, v3 | -564.610874 |
| $Al_2Si_6O_{16}$/Ru, v4 | -566.411913 |
| $Al_2Si_6O_{16}$/Ru, v6 | -566.574549 |
| $Al_2Si_6O_{16}$/Ru, v7 | -565.271503 |
| $Al_3Si_5O_{16}$/Ru, v1 | -565.224644 |
| $Al_3Si_5O_{16}$/Ru, v2 | -564.171189 |
| $Al_3Si_5O_{16}$/Ru, v3 | -563.664739 |
| $Al_3Si_5O_{16}$/Ru, v4 | -565.205222 |
| $Al_3Si_5O_{16}$/Ru, v5 | -564.176478 |
| $Al_3Si_5O_{16}$/Ru, v6 | -563.664747 |
| $Al_4Si_4O_{16}$/Ru, v1 | -561.767796 |
| $Al_4Si_4O_{16}$/Ru, v2 | -561.762668 |
| $Al_4Si_4O_{16}$/Ru, v3 | -563.516278 |
| $Al_4Si_4O_{16}$/Ru, v4 | -562.318282 |
| $Al_4Si_4O_{16}$/Ru, v5 | -561.802701 |

***Table 3:*** *Absolute energies in* eV *for structures with* 25% *surface oxygen that are discussed in section 4.2.*

| Structure | Energy |
|---|---|
| $Si_8O_{16} \cdot 2\,O/Ru$ | -581.888187 |
| $AlSi_7O_{16} \cdot 2\,O/Ru$, v1 | -580.796012 |
| $AlSi_7O_{16} \cdot 2\,O/Ru$, v2 | -580.787943 |
| $AlSi_7O_{16} \cdot 2\,O/Ru$, v3 | -579.552174 |
| $AlSi_7O_{16} \cdot 2\,O/Ru$, v4 | -579.555368 |
| $AlSi_7O_{16} \cdot 2\,O/Ru$, v5 | -579.683990 |
| $AlSi_7O_{16} \cdot 2\,O/Ru$, v6 | -580.739003 |
| $Al_2Si_6O_{16} \cdot 2\,O/Ru$, v1 | -579.234655 |
| $Al_2Si_6O_{16} \cdot 2\,O/Ru$, v2 | -577.821801 |
| $Al_2Si_6O_{16} \cdot 2\,O/Ru$, v3 | -578.286576 |
| $Al_2Si_6O_{16} \cdot 2\,O/Ru$, v4 | -579.567097 |
| $Al_2Si_6O_{16} \cdot 2\,O/Ru$, v5 | -578.391240 |
| $Al_2Si_6O_{16} \cdot 2\,O/Ru$, v6 | -579.526863 |
| $Al_2Si_6O_{16} \cdot 2\,O/Ru$, v7 | -578.401696 |
| $Al_3Si_5O_{16} \cdot 2\,O/Ru$, v1 | -577.694348 |
| $Al_3Si_5O_{16} \cdot 2\,O/Ru$, v2 | -576.270427 |
| $Al_3Si_5O_{16} \cdot 2\,O/Ru$, v3 | -576.792216 |
| $Al_3Si_5O_{16} \cdot 2\,O/Ru$, v4 | -576.270452 |
| $Al_3Si_5O_{16} \cdot 2\,O/Ru$, v5 | -577.694341 |
| $Al_3Si_5O_{16} \cdot 2\,O/Ru$, v6 | -576.791663 |
| $Al_4Si_4O_{16} \cdot 2\,O/Ru$, v1 | -574.066393 |
| $Al_4Si_4O_{16} \cdot 2\,O/Ru$, v2 | -574.085422 |
| $Al_4Si_4O_{16} \cdot 2\,O/Ru$, v3 | -574.097745 |
| $Al_4Si_4O_{16} \cdot 2\,O/Ru$, v4 | -575.500203 |
| $Al_4Si_4O_{16} \cdot 2\,O/Ru$, v5 | -574.588363 |

***Table 4:*** *Absolute energies in* eV *for structures with* 50% *surface oxygen that are discussed in section 4.2.*

| Structure | Energy |
|---|---|
| $Si_8O_{16} \cdot 4\,O/Ru$ | -596.228296 |
| $AlSi_7O_{16} \cdot 4\,O/Ru$, v1 | -593.146748 |
| $AlSi_7O_{16} \cdot 4\,O/Ru$, v2 | -592.978007 |
| $AlSi_7O_{16} \cdot 4\,O/Ru$, v3 | -593.307690 |
| $AlSi_7O_{16} \cdot 4\,O/Ru$, v4 | -592.992384 |
| $AlSi_7O_{16} \cdot 4\,O/Ru$, v5 | -593.312914 |
| $Al_2Si_6O_{16} \cdot 4\,O/Ru$, v1 | -589.587193 |
| $Al_2Si_6O_{16} \cdot 4\,O/Ru$, v2 | -591.739455 |
| $Al_2Si_6O_{16} \cdot 4\,O/Ru$, v3 | -590.724883 |
| $Al_2Si_6O_{16} \cdot 4\,O/Ru$, v4 | -589.838435 |
| $Al_2Si_6O_{16} \cdot 4\,O/Ru$, v5 | -589.298148 |
| $Al_2Si_6O_{16} \cdot 4\,O/Ru$, v6 | -589.569094 |
| $Al_2Si_6O_{16} \cdot 4\,O/Ru$, v7 | -590.205645 |

***Table 5:*** *Absolute energies in* eV *for additional structures with* 25% *surface oxygen that are discussed in section 4.2. Some of these structures contain an additional hydrogen atom.*

| Structure | Energy |
|---|---|
| anti-Löwenstein structure $Al_3Si_5O_{16} \cdot 2\,O/Ru$ | -577,694348 |
| anti-Löwenstein structure $HAl_3Si_5O_{16} \cdot 2\,O/Ru$, v1 | -581.273849 |
| anti-Löwenstein structure $HAl_3Si_5O_{16} \cdot 2\,O/Ru$, v2 | -581.085887 |
| Löwenstein structure $Al_3Si_5O_{16} \cdot 2\,O/Ru$, | -576.791663 |
| Löwenstein structure $HAl_3Si_5O_{16} \cdot 2\,O/Ru$, | -581.805990 |

## Acidity of the H-2dH zeolite: Influence of Al content and metal support

Table 6 lists all structures that are discussed in section 4.3 together with their absolute energies as calculated with VASP. The computational details are discussed in subsection 4.3.1. All relevant files are stored in the archives of the group of Prof. Sauer. The path to the directories is `/archive/frfi/h-2dh-acidity-effects`.

***Table 6:*** *Absolute energies in* eV *for all structures that are discussed in section 4.3.*

| Structure | Energy |
|---|---|
| $HAl_3Si_5O_{16}$ | -386.063497 |
| $HAlSi_7O_{16} \cdot 2O/Ru$ | -1167.636751 |
| $HAl_3Si_5O_{16} \cdot 2O/Ru$ | -1163.383051 |
| $NH_3$ | -19.517268 |
| CO | -14.783885 |
| CO adsorbed on $HAl_3Si_5O_{16}$ | -401.250770 |
| CO adsorbed on $HAlSi_7O_{16} \cdot 2O/Ru$ | -1182.841828 |
| CO adsorbed on $HAl_3Si_5O_{16} \cdot 2O/Ru$ | -1178.572011 |
| $NH_3$ adsorbed on $HAl_3Si_5O_{16}$ | -407.195955 |
| $NH_3$ adsorbed on $HAlSi_7O_{16} \cdot 2O/Ru$ | -1188.903056 |
| $NH_3$ adsorbed on $HAl_3Si_5O_{16} \cdot 2O/Ru$ | -1184.571072 |

## Adsorption of Probe Molecules on Zeolites and a two-dimensional zeolite model system

Table 7 lists all structures that are discussed in section 4.4 together with their absolute energies as calculated with VASP. The computational details are discussed in subsection 4.4.1. All relevant files are stored in the archives of the group of Prof. Sauer. The path to the directories is `/archive/publications/p318`.

***Table 7:*** *Absolute energies in* eV *for all structures that are discussed in section 4.4.*

| Structure | Energy |
|---|---|
| Carbon monoxide in CHA unit cell | -14.779740 |
| Carbon monoxide in 2dH unit cell | -14.779590 |
| Ethene in CHA unit cell | -32.009197 |
| Ethene in 2dH unit cell | -32.008560 |
| Ammonia in CHA unit cell | -19.551462 |
| Ammonia in 2dH unit cell | -19.551112 |
| Pyridine in CHA unit cell | -71.350216 |
| Pyridine in 2dH unit cell | -71.346296 |
| H-CHA, unloaded | -577.383134 |
| H-2dH, unloaded | -385.419463 |
| Carbon monoxide on H-2dH; loading: 1:2 | -400.590559 |
| Carbon monoxide on H-2dH; loading: 2:2 | -415.761875 |
| Carbon monoxide on H-CHA; loading: 1:2 | -592.581795 |
| Ethene on H-2dH; loading: 1:2 | -417.929711 |
| Ethene on H-2dH; loading: 2:2 | -50.454061 |
| Ethene on H-CHA; loading: 1:2 | -609.943110 |
| Ammonia on H-2dH; loading: 1:2 | -406.630272 |
| Ammonia on H-2dH; loading: 2:2 | -427.737220 |
| Ammonia on H-CHA; loading: 1:2 | -598.578097 |
| Pyridine on H-2dH; loading: 1:2 | -458.264502 |
| Pyridine on H-2dH; loading: 2:2 | -530.860847 |
| Pyridine on H-CHA; loading: 2:2 | -650.620700 |

# Selbstständigkeitserklärung

Hiermit erkläre ich, dass ich die vorliegende Dissertation selbstständig und nur unter Verwendung der angegebenen Literatur und Hilfsmittel angefertigt habe.

Frank D. Fischer

# Publications and Scientific Contributions

### Journal Publications

1. S. Kumbhar, **F. D. Fischer**, M. P. Waller, "Assessment of Weak Intermolecular Interactions Across QM/MM Noncovalent Boundaries," *Journal of Chemical Information and Modelling*, vol. 52, no. 1, pp. 93-98, 2012

2. J. A. Boscoboinik, X. Yu, B. Yang, **F. D. Fischer**, R. Włodarczyk, M. Sierka, S. Shaikhutdinov, J. Sauer, H.-J. Freund, "Modeling Zeolites via Metal Supported, Two-Dimensional Aluminosilicate films," *Angewandte Chemie International Edition*, vol. 51, no. 24, pp. 6005-6008, 2012

3. J. A. Boscoboinik, X. Yu, E. Emmez, B. Yang, S. Shaikhutdinov, **F. D. Fischer**, J. Sauer, H.-J. Freund, "The interaction of probe molecules with bridging hydroxyls of two-dimensional zeolites: a surface science approach," *Journal of Physical Chemistry C*, vol. 117, no. 26, pp. 13547-13556, 2013.

4. **F. D. Fischer**, J. Sauer, X. Yu, J. A. Boscoboinik, S. Shaikhutdinov, H.-J. Freund, "Ultrathin Ti-Silicate Film on a Ru(0001) surface," *Journal of Physical Chemistry C*, vol. 119, no. 27, pp. 15433-15448, 2015.

### Poster Contributions to Scientific Conferences

1. **F. D. Fischer**, R. Włodarczyk, J. Sauer, X. Yu, J. A. Boscoboinik, E. Emmez, B. Yang, S. Shaikhutdinov, H.-J. Freund, "Atomic structure of Fe- and Ti-substituted thin films of Silica on Ru(0001)", 17th International Zeolite Conference, Moscow, 2013.

2. **F. D. Fischer**, J. Sauer, "Probing Bridging Hydroxyls of two-dimensional Zeolites", 26. Deutsche Zeolith-Tagung, Paderborn, 2014.

3. **F. D. Fischer**, R. Włodarczyk, J. Sauer, X. Yu, J. A. Boscoboini, E. Emmez, B. Yang, S. Shaikhutdinov, H.-J. Freund, "Atomic structure of Fe- and Ti-substituted thin films of Silica on Ru(0001)", 6th International FEZA Conference, Leipzig, 2014.

# Acknowledgements

I thank Prof. Dr. Dr. h.c. Joachim Sauer for his most valuable guidance as my PhD supervisor, emphasizing high scientific standards, sharp analysis and clear presentations. In particular, I want to thank him for providing the opportunities to work in productive collaboration projects with experimentalists on interesting, rewarding topics. I also want to thank all the collaboration partners at the Fritz-Haber Institut, in particular Prof. Dr. Hans-Joachim Freund, Dr. Shamil Shaikhutdinov and Dr. Jorge Anibal Boscoboinik.

I gratefully acknowledge support by the German Chemical Industry Fund(FCI) and also thank the North German Computing Alliance Berlin (HLRN) for a computer grant.

Computational chemistry is not possible without smoothly running and well-maintained computers. I want to thank our systems administrator, Thomas Dargel for his help.

Thanks also go to all group members, especially to Dr. Radosław Włodarczyk and Dr. GiovanniMaria Piccini, for helpful advice and stimulating discussions.

In the finalization of this thesis, the support by my parents was most important and a very big "Thank You!" is reserved for them.